

NUREG/CR-0768
SAND79-0820
Vol. 10
R3

**Light Water Reactor Safety Research Program
Quarterly Report
October - December 1978**

Volume 10

Marshall Berman

Printed July 1979



Sandia Laboratories

2900 Q(7-73)

Prepared for
U. S. NUCLEAR REGULATORY COMMISSION

8007280 007

NOTICE

This report was prepared as an account of work sponsored by an agency of the United States Government. Neither the United States Government nor any agency thereof, or any of their employees, makes any warranty, expressed or implied, or assumes any legal liability or responsibility for any third party's use, or the results of such use, or any information, apparatus, product or process disclosed in this report, or represents that its use by such third party would not infringe privately owned rights.

The views expressed in this report are not necessarily those of the U. S. Nuclear Regulatory Commission.

Available from
National Technical Information Service
Springfield, VA 22161


NUREG/CR-0768
SAND79-0820
R3

LIGHT WATER REACTOR SAFETY RESEARCH PROGRAM
QUARTERLY REPORT
OCTOBER - DECEMBER 1978
Vol. 10

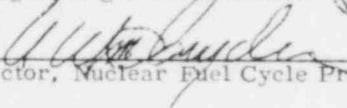
Person in Charge:
Marshall Berman, 441

Date published: July 1979

APPROVED:



Manager, Light Water Reactor Safety



Director, Nuclear Fuel Cycle Programs

Sandia Laboratories
Albuquerque, NM 87185
Operated by
Sandia Laboratories
for the
U. S. Department of Energy

Prepared for
Division of Reactor Safety Research
Office of Nuclear Regulatory Research
U. S. Nuclear Regulatory Commission
Washington, DC 20555
Under Interagency Agreement DOE 40-550-75
NRC FIN Nos. A-1019, -1030, -1205, and -1207

Contributing Authors:

T. J. Bartel	L. S. Dike
W. B. Benedick	M. A. Ellis
A. S. Benjamin	D. E. Mitchell
M. Berman	J. F. Muir
F. G. Blottner	L. S. Nelson
L. D. Buxton	D. A. Powers
R. K. Byers	G. P. Steck
R. K. Cole, Jr.	D. Tomasko
M. L. Corrandini	W. H. Vandevender

CONTENTS

	<u>Page</u>
1. Molten Core/Concrete Interactions Study	7
1.1 Summary	7
1.2 Molten Core/Concrete Interaction Experimental Program	9
1.3 Molten Core/Concrete Interaction Analytical Program	36
References	40
2. Steam Explosion Phenomena	41
2.1 Summary	41
2.2 Triggering Experiments	45
2.3 Efficiency Scaling Studies	56
2.4 Fully Instrumented Test Series	65
2.5 Theoretical Analysis of Steam Explosions	68
2.6 Assessment of Containment Failure Capability	74
References	77
3. Statistical Analysis	79
3.1 Summary	79
3.2 Statistical Blowdown Calculations	80
3.3 Reflood Calculations	98
3.4 FRAP	101
3.5 Statistical Development	102
References	102
4. UHI Model Development	103
4.1 Summary	103
4.2 Computational Experience	104
4.3 Heat Transfer	109
4.4 TRAC-UHI	110
Reference	115
5. Two-Phase Jet Loads	117
5.1 Summary	117
5.2 Experimental Data	117
5.3 Computer Program Results	128
5.4 Future Work	133
References	134

LIGHT WATER REACTOR SAFETY RESEARCH PROGRAM

1. Molten Core/Concrete Interactions Study

1.1 Summary

The Molten Core/Concrete Interactions Study was begun on July 15, 1975, to provide a qualitative, extensive exploration of the phenomena associated with contact between molten-core materials and concrete. The experimental elements of this study are divided into four categories:

1. Deposition of Corium-type melts onto concrete
2. Kinetics and stoichiometry of the thermal decomposition of concrete
3. Response of concrete to high heat fluxes at one surface
4. Simulation experiments which explore phenomena at the interface between a melt and a decomposing solid.

Experimental results are being incorporated in a computer model and a scaling analysis. They will establish scaling parameters for the system and identify key elements of the melt/concrete interaction. A complete project description of the study was issued in October 1975.¹

Experimental activities during the quarter produced a potpourri of results. Those presented herein include:

- A description of the two "standard tests" to be used as a basis for comparing the melt/concrete interaction computer models developed here (CORCON, GROWS) and in Germany (WECHSL, KAVERN). A fairly detailed description of the Sandia COIL test (Standard Test 1) to be performed later this year is provided.
- The compositions and thermochemical properties of the three "default" concretes recommended for inclusion in the CORCON melt/concrete interaction model. They are (1) a basaltic aggregate concrete, (2) a limestone aggregate concrete, and (3) a generic southeastern United States (GSEUS) concrete. The first two, which use common sand for fine aggregate, are representative of the concrete used in a large number of existing light water reactor (LWR) power plants. The first type is also quite similar to the concrete used in the Fast Flux Test Facility. The third type has been specified for use in the Clinch River Breeder Reactor, hence it is also referred to as "CRBR concrete." Characteristics given for each of the default concretes are composition, solidus and liquidus temperatures, temperatures and energies associated with the decomposition reactions and phase changes, weight losses accompanying the decomposition reactions, and a model for the effective heat capacity as a function of temperature. These heat-capacity models are compared against other models and experimental data available in the literature.

- The results of a posttest analysis of the crucible used in the BURN 0 test. One of the objectives of the test was to observe the interaction of molten Corium with samples of four refractory materials (calcia stabilized zirconia, hafnium carbide, tungsten boride, and yttrium oxide) embedded in the bottom of the concrete crucible. The posttest examination suggests that none of the refractory materials tested would be suitable for prolonged exposure to a Corium melt.
- Additional results obtained from further analysis of the data obtained from the BURN 1 test. An extensive frame-by-frame analysis of the x-ray motion picture film of the experiment was performed to determine (1) the swelling of the melt produced by gases evolved during the melt/concrete interaction, and (2) the actual contact between the melt and concrete at various points around the periphery of the pool. Pool level swell is found to be roughly independent of gas generation rates for superficial velocities greater than about 2.4 m/s. Below this value, level swell is approximately a linear function of gas generation rate (i.e., superficial velocity). Pool level swell (mean level) as high as 250% of the gas-free good depth was observed. Melt/concrete contact was greatest midway between localized gas emission sites (~70% of the time) and in the corner created by the bottom/sidewall junction (~80% to 90% of the time). Points on the cavity walls near the top of the pool are contacted only about 40% to 50% of the time. The lowest melt/concrete contact occurred at the localized gas generation sites (~20% to 30% of the time).

The analytical effort during the quarter continued to emphasize the development and programming of phenomenological models for the improved molten core/concrete interaction code, CORCON. The Equilibrium State Procedure (ESP) model developed by ACUREX/Aerotherm Corporation was completed and the program delivered to Sandia. In addition to the continuing effort on the concrete ablation and shape change model (also being developed by ACUREX), on several heat transfer models, and on a gas-volume-fraction/pool-level-swell model, work was started on a model describing the melt/gas chemical reactions encountered during molten core/concrete interactions.

Programming activities included the writing, coding, and checkout of a primitive CORCON main or driver program containing mostly dummy subroutines. In addition, several phenomenological model and data handling subroutines were completed, incorporated into CORCON, and checked out. These were: a data input subroutine (DATAIN), a routine for plotting computational results (DATAPLOT), a modified version of the ESP program for computing the thermochemical equilibrium state of gas mixtures (GEQUIL), a modified version of the VISRHO code for computing the density and viscosity of complex silicate melts (VISRHO), and a model for calculating the dynamic viscosity and thermal conductivity of equilibrium gas mixtures (GVISCON).

The investigation of the numerical aspects of INTER and CORCON, begun last quarter, revealed that the convergence of computations made with INTER could be improved with only a slight (~5%) increase in run time by replacing an algorithm for solving nonlinear equations with an alternative scheme available in the math library.

1.2 Molten Core/Concrete Interaction Experimental Program (D. A. Powers)

1.2.1 MCCI Code Comparison Experiments

Sandia Laboratories and Projekt Nukeare Sicherheit of Kernforschungszentrum Karlsruhe have agreed to perform two standard tests. Data from these tests will be used to evaluate predictions made by computer models of the melt/concrete interactions. To date the codes that will be used to make these predictions will be WECHSEL (developed at KfK by W. Murfin and M. Reimann), CORCON (developed at Sandia by J. F. Muir, et al.), and KAVERN (developed at the Kraftwerke Union by K. Hassman, et al.)

Developers of the GROWS code (Argonne National Laboratory and University of California, Los Angeles) will be invited to participate in this activity.

The comparison between experimental data and computer predictions will not be done in an attempt to verify the computer models. Rather it will be done to compare the codes. Undoubtedly the comparisons will point to areas where improvements in the codes should be made.

The two standard tests will be (1) Sandia's COIL test, in which about 200 kg of molten stainless steel will be deposited on the so-called CRBR (or GSEUS) limestone concrete, and (2) a KfK test called "Super-Thermit," in which about 1000 kg of thermit will react with a siliceous concrete.

Only geometric and other data necessary to make the model predictions will be supplied to the model developers. Some of these data for the COIL test are given in the next subsection. Actual experimental results will be made available only after the model predictions have been transmitted to the experimental groups.

Data that will be used in the comparison of the codes are

- Posttest profile of the crucible cavity
- Velocity of melt penetration
- Temperature distributions, both spatial and temporal, in the concrete
- Posttest weight of the metallic phase of the melt
- Time at which solidification of the melt begins.

The last item on this list is fairly difficult to collect. The models, however, have shown this to be a very sensitive quantity in prediction; differences of a factor of 10 can arise. Experimenters will have to keep quite detailed records on this process. The modellers will then have to select the data they want to use.

Specifications for the Standard COIL Test -- All basic procedures for the standard test problem will be similar to those described in SAND77-1423.² The description below reiterates many of the points in that document and expands on points where experimental procedure has improved since it was published.

Test Arrangement

Melt: Type 304 stainless steel weighing about 200 kg. Melt will be teemed at a temperature of 1700°C.

Crucible: Cylindrical block with a coaxial cylindrical cavity (identical to that described in Reference 2).

Top Hat: A top hat made of stainless and mild steel will be lowered over the crucible once the melt is in place. The top hat constrains effluent given off during the interaction so that these effluents may be measured. It contains two essential features: a cylindrical chimney assembly and an instrumentation section.

COIL Test Instrumentation

I. Test Procedure

- A. Time zero indicated by thermocouples within cavity that fail on impact of first portion of melt.
- B. Duration of pour indicated by motion picture and television coverage of test.
- C. Top hat closure indicated by motion picture coverage and by gas flow meters.

II. Diagnostics

A. Response of Concrete

- 1. Embedded thermocouples in concrete will provide temperature profiles and erosion rates.
- 2. Fracturing indicated by displacement gages mounted horizontally on exterior wall of crucible 25 and 43 cm below top of crucible.
- 3. Moisture migration in concrete monitored by electrical conductivity and pressure transducer probes located on centerline of crucible. Locations are 2.5, 5, and 10 cm below the original bottom of the crucible cavity.

CONCRETE

Type: Clinch River Limestone Concrete Composition (wt%):

Fe ₂ O ₃	1.2	SiO ₂	3.6
Cr ₂ O ₃	0.004	Al ₂ O ₃	1.6
MnO	0.01	CO ₂	35.7
TiO ₂	0.12	SO ₂	not detected
K ₂ O	0.68	Evaporable	2.3
		H ₂ O	

Na ₂ O	0.078	H ₂ O	2.3
CaO	45.4	Chemically constituted	1.8
MgO	5.67	H ₂ O	

Melting Range: 1430° to 1600°C

Aggregate Size: Per ACI specifications; maximum size is 2 cm. Fine aggregate made of crushed limestone.

B. Effluent

1. Upward heat flux indicated by two gages, mounted so that one is parallel and the other perpendicular to the surface of the melt. Active portion of each gage about 50 cm above surface of molten pool. The two gages should permit separation of upward heat transfer into terms for convective mass transfer and for radiation.
2. Gas phase temperature monitored by shielded thermocouples at the heat flux gages and at the gas sampling port.
3. Aerosol concentration monitored optically at the gas sampling port with a laser system. Both forward and right-angle scattering will be sensed.
4. Gas flow measured pitot-statically.
5. Gas composition monitored by grab samples. Real-time, continuous, composition data for H₂O, CO, CH₄, and CO₂ will also be provided.
6. Aerosol will be collected with a cascade, inertial impactor.

C. Melt Temperature

1. As is feasible, melt temperatures will be taken by immersion thermocouples. To do this the top hat will be raised.
2. When the top hat is raised a pyrometer will be used to measure temperatures. This will also afford an opportunity to detect crust formation.

D. Power Input

1. Water flow to cooling coil will be measured.
2. The ΔT of water will be measured.
3. After melt has cooled, a series of heating tests will be conducted to measure power coupling as a check of the active measurements during the test.

III. Posttest Measurements

- A. An x-ray of the crucible will be taken to determine the erosion profile.
- B. A chemical analysis of the slag and steel will be made to measure melt oxidation.

1.2.2 Concrete Compositions for the Computer Model CORCON

The computer program CORCON is to be used to predict the nature of melt/concrete interactions during a hypothetical reactor accident involving fuel melting. The model will allow as input variable concrete compositions. It is, desirable, however, that default concrete compositions be built into the model. The default compositions will make the model more easily used for generic, as opposed to site-specific, investigations.

One especially important use of CORCON will be for sensitivity analyses. Concrete composition will clearly be a variable in such sensitivity analyses. Because the impact of concrete composition on the nature of melt/concrete interactions should be well understood, it would be unwise to use a single default concrete composition.

Criteria for selecting default concrete compositions:

- Concretes should be representative of concrete found in a significant number of existing reactors or be representative of a type of concrete of particular interest to a substantial number of potential users of CORCON.
- Properties of concrete which are felt to have substantial influence on the nature of melt/concrete interactions should vary over a substantial range among the default case concretes.
- Selected concretes should have been subjected to experimental study of their interactions with high-temperature prototypic melts.

The Molten Core/Concrete Interactions Study and the Molten Core Technology program at Sandia have involved three types of concrete: (1) basaltic aggregate, (2) limestone aggregate-common sand, and (3) generic southeastern United States (GSEUS, or the so-called CRBR concrete). The first two of these concrete types are representative of concrete in a large number of LWRs. The first type is also quite similar to concrete found in the Fast Flux Test Facility. The third concrete type is of particular interest since this concrete would be used in the Clinch River Breeder Reactor should it be built.

Properties of concrete which are currently believed to have the most direct influence on melt/concrete interactions are

- The melting temperature range of solid concrete decomposition products
- Quantities of materials such as hydrates and carbonates in the concrete which may be thermally decomposed to yield volatile products
- The ratio of hydrates to carbonates in the concrete.

Basaltic aggregate and limestone aggregate-common sand concretes both begin to melt about 1100°C. The liquidus temperatures for these concretes are 1350° to 1400°C. Consequently, both of the first two types of concrete are completely molten at temperatures below the solidification temperature of metallic phases of a hypothetical core melt. The GSEUS concrete begins to melt at about 1450°C and is not fully molten until temperatures in excess of 1600°C are reached.

The melting temperature range of this concrete includes the solidification temperature expected for metallic phases of a hypothetical core melt.

Decomposition reactions of concrete typically occur in three temperature ranges which may be broadly categorized as

- Loss of evaporable water (70° - 250°C)
- Loss of chemically constituted water (350° - 550°C)
- Loss of carbon dioxide from calcite and dolomite in the concrete (580° - 1050°C).

Weight losses associated with each of these reactions for the three concrete types are listed in Table 1-I. It may be seen from these data that: (1) weight losses from the concrete due to the thermal decomposition reactions may be ordered as: basaltic aggregate < limestone aggregate-common sand < GSEUS; (2) weight losses from basaltic aggregate concrete are almost entirely due to dehydration reactions; (3) weight losses due to dehydration are similar for all three concrete types; (4) weight losses from limestone aggregate-common sand concrete are due to both dehydration and decarboxylation reactions which yield nearly equal volumes of volatile decomposition products; and (5) volatile decomposition products of GSEUS concrete are predominantly carbon dioxide.

TABLE 1-I
Losses Associated With Decomposition Reactions of
Tested Concretes

	Loss (wt% (l/g) [*])		
	Evaporable Water	Chemically Constituted Water	Carbon Dioxide
Basaltic aggregate concrete	3 (0.038)	2 (0.025)	1.5 (0.008)
Limestone aggregate- common sand	2.7 (0.034)	2 (0.025)	22 (0.112)
GSEUS-CRBR Concrete	2.3 (0.027)	2 (0.025)	35.7 (0.182)

* Gas volumes in litre/gram of concrete at standard temperatures and pressure.

It is apparent that the three concrete types used in Sandia experimental programs satisfy the criteria of default concretes for CORCON. Compositions for these concretes may be expressed in a variety of ways. The oxide basis for concrete compositions are shown in Table 1-II. Choices for the oxides of iron and manganese are quite arbitrary since these elements are polyvalent. At the elevated temperatures, manganese and iron are best treated as mono-oxides. Water contents

of the concretes have been differentiated into evaporable and chemically constituted water to be consistent with the needs of CORCON.

TABLE 1-II
Chemical Compositions of Default Concretes
(values in wt %)

	Basaltic Aggregate Concrete	Limestone Aggregate- Common Sand Concrete	GSEUS-CRBR Concrete
Fe ₂ O ₃	6.25	1.44	1.2
Cr ₂ O ₃	ND	0.014	0.004
MnO	ND	0.03	0.01
TiO ₂	1.05	0.18	0.12
K ₂ O	5.38	1.22	0.68
Na ₂ O	1.8	0.082	0.078
CaO	8.8	31.2	45.4
MgO	6.15	0.48	5.67
SiO ₂	54.73	35.7	3.6
Al ₂ O ₃	8.3	3.6	1.6
CO ₂	1.5	22	35.7
SO ₂	0.2	0.2	-
Evaporable H ₂ O	3	2.7	2.3
Bound H ₂ O	2	2	1.8

ND
Not determined

Alternative descriptions of concrete in terms of the mix used to make the concrete are shown in Table 1-III. Such descriptions are not especially accurate. Water used to make the concrete bears no simple relationship to the two types of water present in cured concrete. The mix description together with the chemical descriptions of concrete in Table 1-II and chemical descriptions of the concrete constituents in Table 1-IV should assist in the formulation of chemical descriptions of concrete where chemical data are not available. Caution is definitely urged when this procedure must be used.

TABLE 1-III

Engineering Composition of Default Concretes
(all values in pounds)

	<u>Limestone Aggregate- Common Sand Concrete</u>	<u>Basaltic Aggregate Concrete</u>	<u>GSEUS-CRBR Concrete</u>
Coarse aggregate	187	205	364
Fine aggregate	93	-	260
Sand	205	203	-
Fly ash	-	-	3.2
Cement	94	94	94
Water	42	45	53-59

TABLE 1-IV

Chemical Compositions of Concrete Constituents
(values in wt %)

<u>Oxide</u>	<u>Types 1&2 Cement</u>	<u>Limestone Aggregate (from GSEUS-CRBR concrete)</u>	<u>Basaltic Aggregate</u>	<u>Sand</u>	<u>Fly Ash</u>	<u>Limestone Aggregate (from limestone aggregate-common sand concrete)</u>
Fe ₂ O ₃	4.11	0.38	7.78	2.15	11.7	0.33
Cr ₂ O ₃	0.011	0.012	0.063	0.042	0.022	ND*
MnO	0.08	0.04	0.08	0.02	0.02	ND
TiO ₂	0.2	0.04	1.82	0.18	2.24	0.05
K ₂ O	0.54	0.36	7.2	2.7	3.5	0.3
Na ₂ O	0.27	0.16	1.85	1.74	0.34	0.15
CaO	63.5	47.2	6.54	1.52	1.3	45.56
MgO	1.53	0.6	9.7	0.34	1.14	0.8
SiO ₂	20.1	8	54.9	82.8	51.2	12.98
Al ₂ O ₃	4.2	1.2	9.51	7.24	24.5	1.25
CO ₂	ND	38	ND	ND	ND	40

* Not determined

Melting ranges for the default concretes are:

<u>Concrete</u>	<u>Temperature (°C)</u>	
	<u>Solidus</u>	<u>Liquidus</u>
Basaltic	1080	1380
Limestone-common sand	1150	1400
GSEUS-CRBR	1450	1600

Heats of melting are not adequately known, but should be about 100 cal/g.

Thermal effects involved in the decomposition of concrete have been incompletely studied. Until more reliable data are available, the values below are recommended (see Tables 1-III and -IV).

Heat capacity of concrete is a poorly defined quantity because of the time- and mass-dependence of the decomposition reactions. Heat capacity may be defined for the solid decomposition products of concrete. This heat capacity has again not been well investigated. In the absence of quality experimental data, the following equations are recommended:

a. Basaltic Concrete

$$C_p = 0.2245 + 0.0001332 T - \frac{4698.7}{T^2}$$

b. Limestone aggregate - Common Sand Concrete

$$C_p = 0.1697 + 0.0001031 T - \frac{3276.5}{T^2}$$

c. GSEUS-CRBR Concrete

$$C_p = 0.1085 + 0.0000497 T - 1433.23/TT$$

T = absolute temperature (K)

To correct for the volatile species add the following factors:

for $0 < T < 373$ K

a.
$$C_p(1) = \frac{W_e}{100} (0.6222 + 0.000428 T)$$

for $0 < T < 658$ K

b.
$$C_p(2) = \frac{W_{CH}}{100} (0.5244 + 0.401 \times 10^{-3} T)$$

for $0 < T < 273 \text{ K}$

$$c. \quad C_p(3) = \frac{W_{CO}}{100} (0.175 + 0.00012 T + 0.0189 \times 10^{-6} T^2)$$

where

W_e = wt% evaporable water

W_{CH} = wt% chemically constituted water

W_{CO} = wt% carbon dioxide

A formula for the "heat capacity" of concrete that takes into account both mass-loss and heats of decomposition may be written as

$$\begin{aligned} C_p (\text{cal/K} - \text{g concrete}) &= C_p(\text{res}) + C_p(1) \text{ g (393)} \\ &+ C_p(2) \text{ g (693)} + C_p(3) \text{ g (993)} + W(1) f (333, 543) \\ &+ W(2) f (663, 713) + W(3) f (843, 863) + W(4) f (999, 1123) \end{aligned}$$

where

$$g(T_0) = \text{erfc} [5(T - T_0)/T_0]$$

$$f(T_r, T_u) = \frac{1}{\sqrt{2\pi}\sigma} \exp\left(-\frac{1}{2} \left(\frac{T - \mu}{\sigma}\right)^2\right)$$

$$\mu = 1/2 (T_r + T_u)$$

$$\sigma = 1/2 (T_u - T_r)$$

T = absolute temperature (K)

$C_p(i)$ = residue heat capacity and correction terms defined above

$W(j)$ = decomposition energies (see Table 1-V)

$j = (1)$ heat of evaporable water loss

$j = (2)$ heat of chemical water loss

$j = (3)$ heat of SiO_2 $\alpha \rightarrow \beta$ phase change

$j = (4)$ heat of decarboxylation

Plots of this heat capacity function for the various default concretes are shown in Figures 1-1 and 1-2. Note that the shape of the curves in the vicinities of decomposition reactions is designed to account in an approximate way for the kinetic nature of the decomposition reaction. The adjustable parameters in the $g(T_0)_1$ and $f(T_r, T_u)$ functions may be varied to give even better agreement with the kinetic behavior of the decomposition reactions. A more sophisticated treatment of this aspect of heat capacity is definitely possible. Because of these heat effects, the above formula is applicable only when concrete is first heated. After concrete has been completely decomposed, the $C_p(\text{res})$ functions describe heat capacity again in units of cal/K-g virgin concrete.

TABLE 1-V
Heat of Decomposition or Phase Change
(values in cal/g concrete)

Concrete	Loss of Evaporable Water	Loss of Chemical Water	$\alpha \rightarrow \beta$ Phase Change in SiO_2	Decarboxylation
Basaltic	18.3	28	1.3	13.6
Limestone - common sand	16.5	28	0.3	200
GSEUS-CRBR	14	28	0	324

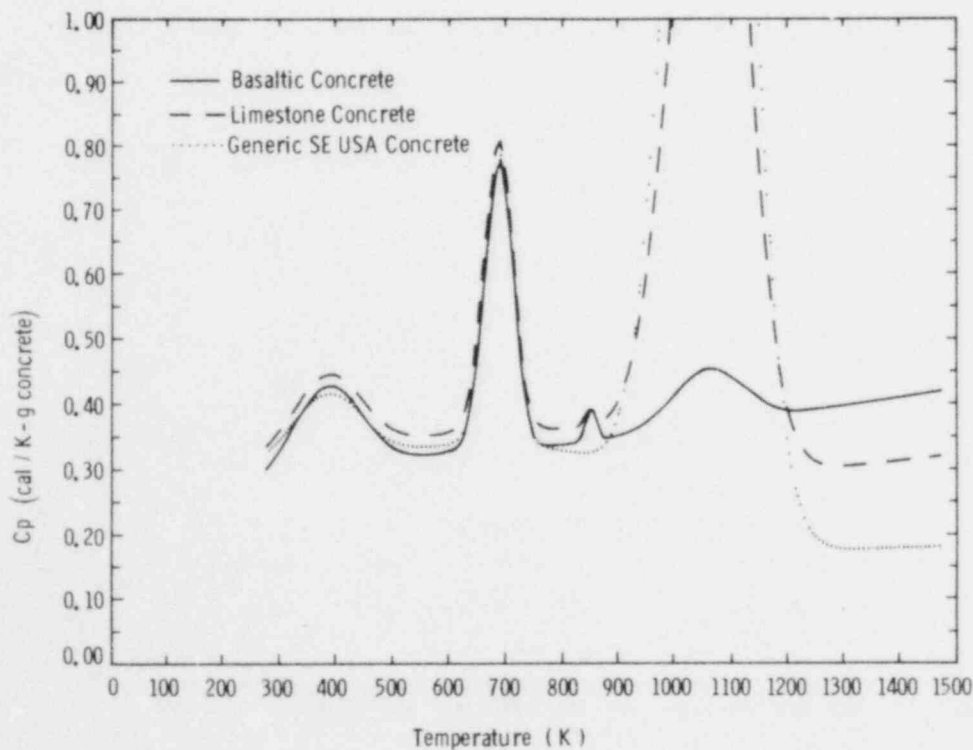


Figure 1-1. Heat Capacity vs Temperature With Heat Effects

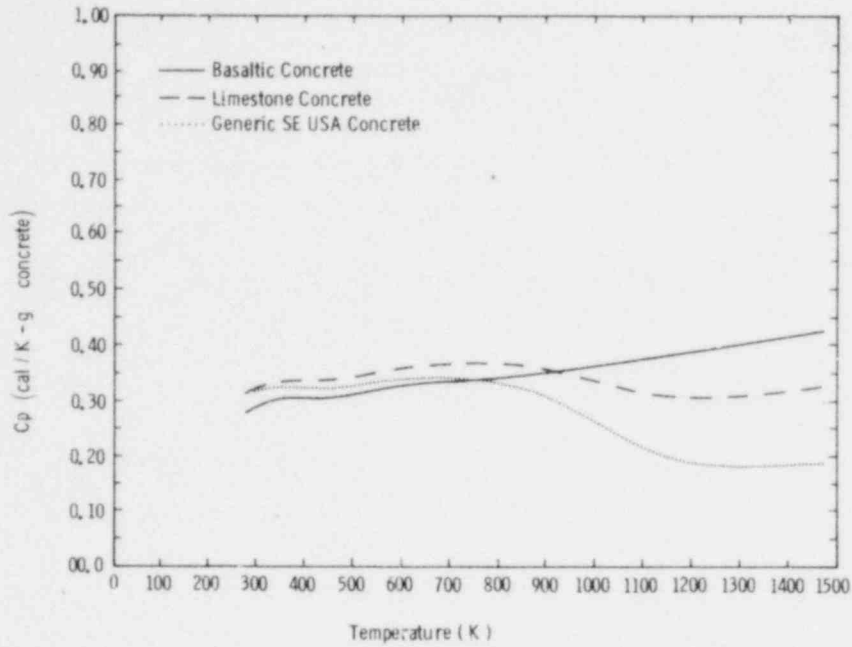


Figure 1-2. Heat Capacity vs Temperature Without Heat Effects but Including Mass-Loss Effects

Comparison of Heat Capacity Model to Other Models and Experimental Data -- Harmathy has described a model for estimating the thermophysical properties on concrete, including the heat capacity of concrete.³ He used his model to predict heat capacity of a siliceous concrete he labelled "#2". A comparison of Harmathy's estimates and those made with the model described here is shown in Figure 1-3.

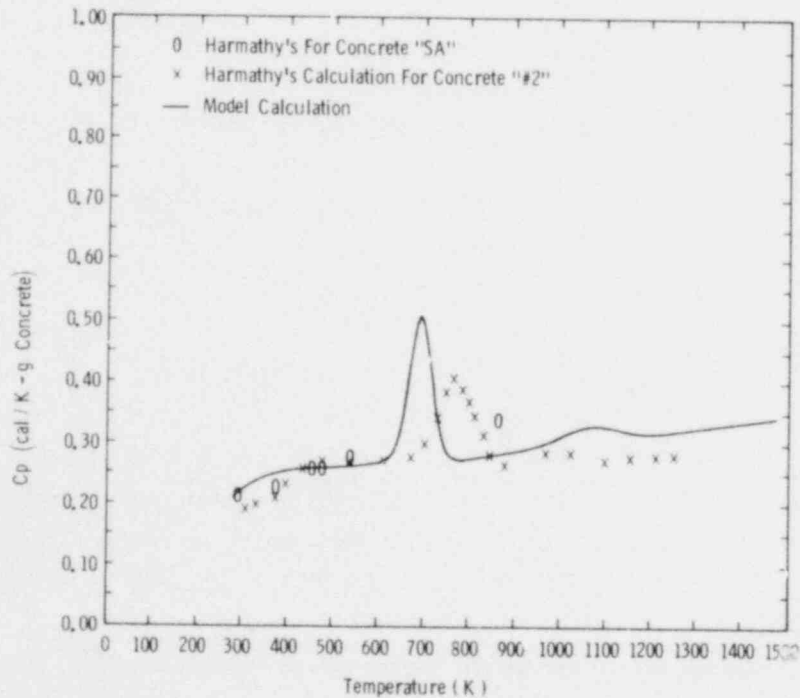


Figure 1-3. Comparison of Estimates in Reference 3 to the Results From Our Model

Harmathy's characterization of concrete "#2" was not suited for the requirements of the model described here. To make the necessary changes some reinterpretation of the experimental data was done. The most important changes:

- The cement binder was assumed to be a fully cured mixture of $(\text{CaO})_{1.62} \text{SiO}_2 \cdot 1.5 \text{H}_2\text{O}$ and $\text{Ca}(\text{OH})_2$.
- Weight loss in the thermogram of Harmathy's cement binder #2 was assumed to be due to loss of CO_2 at temperature 600°C .

The composition of cement "#2" was then found to be:

<u>Component</u>	<u>Weight %</u>
Na_2O	4.00
CaO	19.28
Al_2O_3	25.18
SiO_2	48.92
Free H_2O	0.79
Bound H_2O	1.06
CO_2	0.46

* All silica bound so that no $\alpha \rightarrow \beta$ transition occurred.

The residual heat capacity of the material was determined:

$$C_p(\text{res}) = 0.2003 + 0.9772 \times 10^{-4} T - \frac{4364}{T^2} .$$

The general trends of Harmathy's calculation and that produced from the present model are quite similar. Up to 600 K agreement between the two models is good. Any discrepancies are due to the fact that the present model allows easier removal (lower temperature removal) of free water than does the Harmathy model. Consequently, Harmathy predicts a more abrupt change in heat capacity in the vicinity of 370 K.

The present model predicts the influence of bound water loss on heat capacity to arise at lower temperatures than does Harmathy's model. This is a fine example of the difficulties in understanding heat capacity of chemically reacting substances. Because these reactions are kinetic in nature, the heat effects they produce arise at temperatures that are functions of the heating rate. In the model presented here, the heat effect terms are characterized by a parameter that determines the location and a parameter that determines the magnitude and breadth of the heat effect. Some arbitrary values of these parameters have been used in this model. Simply adjusting these parameters would bring the present model into good agreement with the Harmathy model in the region of bound water loss. A similar rationale could be used to adjust the rise in heat capacity due to decarboxylation at about 1050 K.

The physical justification of varying the parameters for the endothermic reactions is a question. These parameters do relate to the kinetic rate expressions for the concrete reactions developed by Powers.⁴

Elsewhere, Harmathy has presented heat capacity data for several varieties of concrete.⁵ His characterizations were, again, not suitable for the needs of the present model. To compare the experimented data to the calculated estimates it was assumed that the autoclaved siliceous concrete "SL" was similar to Harmathy's concrete "#2", that the siliceous concrete "S" was similar to the basaltic concrete described above, and that the calcareous concrete "C" was similar to the limestone-common sand concrete described above. Comparisons between the experimental and calculated heat capacity are made in Figures 1-3 through 1-5.

Peeh's has also presented heat capacity data for a siliceous concrete. His data, which agree well with Harmathy's data for the "S" concrete, are compared with the calculated result in Figure 1-4.

There is very strong disagreement between the model predictions and the experimental data for Harmathy's "C" concrete. No explanations for this disagreement can be offered at this time. Characterization of this concrete was not suitable for our model; therefore, data for the limestone-common sand default concrete were used. This might be one source of the discrepancies.

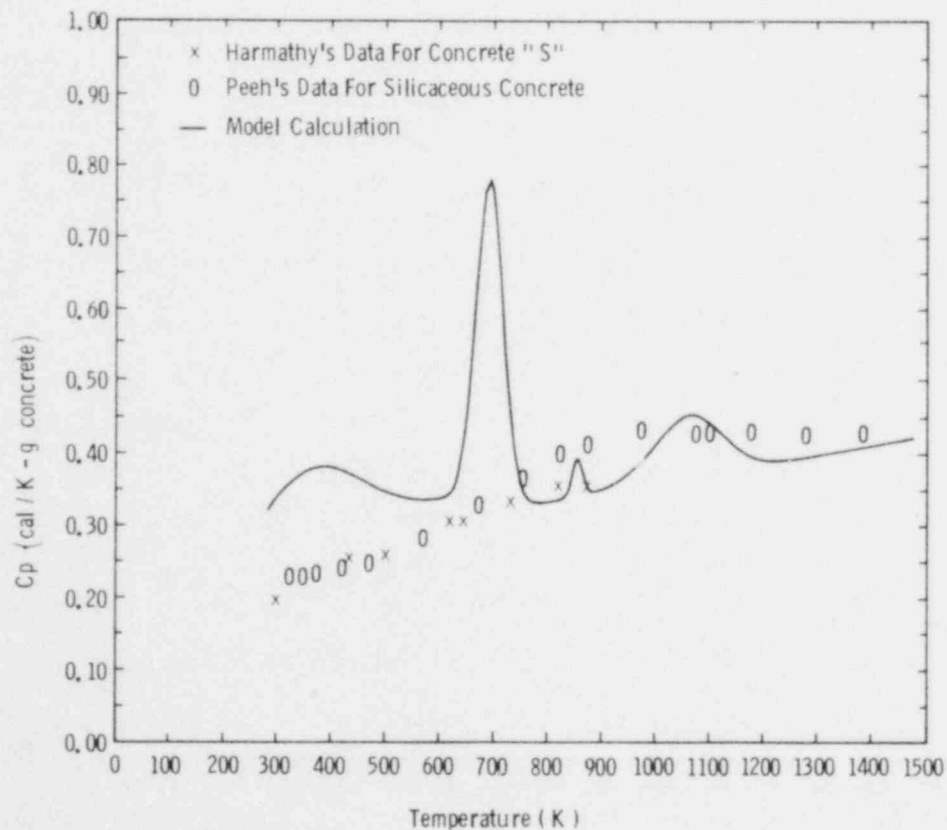


Figure 1-4. Siliceous Concrete -- Comparison of Data From Other Sources to Results From Our Model

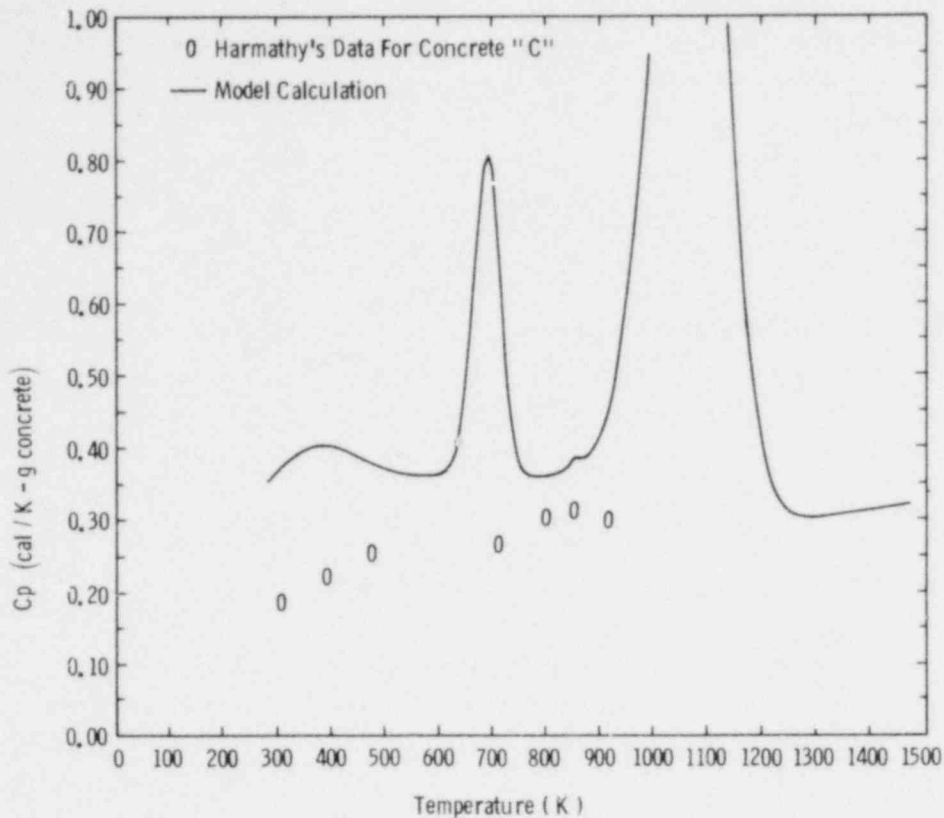


Figure 1-5. Calcareous Concrete -- Comparison of Reference 3 Data With Results From Our Model

1.2.3 Steel Oxidation During Melt/Concrete Interactions

Chemical composition of various steel samples taken during the COIL tests are listed in Table 1-VI.

TABLE 1-VI
COIL Test Steel Compositions

Sample Description	Composition (wt%)*			
	Cr	Fe	Ni	Mn
Stainless steel before melt formation	18.4	69.6	8.72	1.85
Stainless steel melt just before teem into concrete crucible	18.8	68	8.61	1.76
Steel after transient test, GSEUS-CRBR concrete	17.5	66	8.37	1.94
Stainless steel after a test with GSEUS-CRBR concrete sustained for 9.5 min.	15.3	70.8	9.26	0.35

* Compositions do not necessarily total 100% because of nonmetallic material included in the samples.

The percentage data shown in Table 1-VI are not suitable for determining the absolute extent of melt oxidation because the total metal weight at the conclusion of the test could not be measured. The data are suitable for determining the relative extents to which constituents of the melt are oxidized. In doing this, analytic errors and sampling errors are important because the relative determinations involve small differences in large numbers.

If it is assumed that nickel oxidation has a value of 1, then the extent of chromium oxidation is 1.35 and iron oxidation is 2.08 in the transient tests. Similar results from the sustained test of stainless steel/GSEUS concrete are:

Ni	1.00
Mn	1.49
Fe	4.19
Cr	5.14

These results do not recognize the varying concentrations of constituents in the melt. When the sustained tests are normalized for metal-atom concentration, they become:

Ni	1.00
Mn	6.57
Fe	0.50
Cr	2.16

These results are still not in good agreement with thermodynamic estimates and obviously both more sophisticated analysis and more extensive chemical composition data are needed.

1.2.4 Posttest Analysis of the Crucible Used in BURN 0 Test

The experimental details and objectives of BURN 0 test have been described elsewhere.⁶ One objective of this test was to observe the interaction of molten Corium with these refractory materials: calcia stabilized zirconia, hafnium carbide, tungsten boride, and yttrium oxide. Post-test inspection of the crucible, described here, was intended to confirm the observations made by x-rays described in Reference 6.

Dissection of the crucible showed that the solidified melt consisted of an upper layer of slag on metal droplets and a lower layer of stainless steel. A photograph of the top surface of the steel layer is shown in Figure 1-6. Notice that eruptions of slag occur in this layer at positions above the refractory test specimens in the concrete.

The steel had flowed into crevices created by the specimens in the concrete. The steel was removed with some difficulty. The surface below the steel is shown in Figure 1-7. Refractory specimens are marked in this figure.

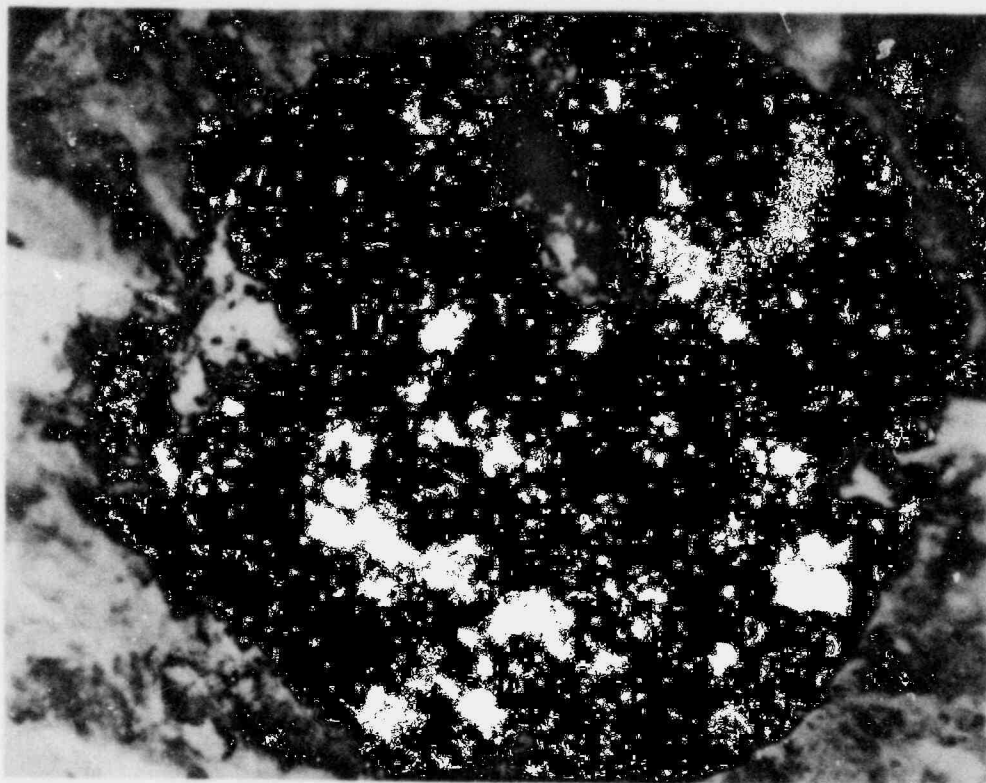


Figure 1-6. Top Surface of Solidified Steel in BURN 0 Test

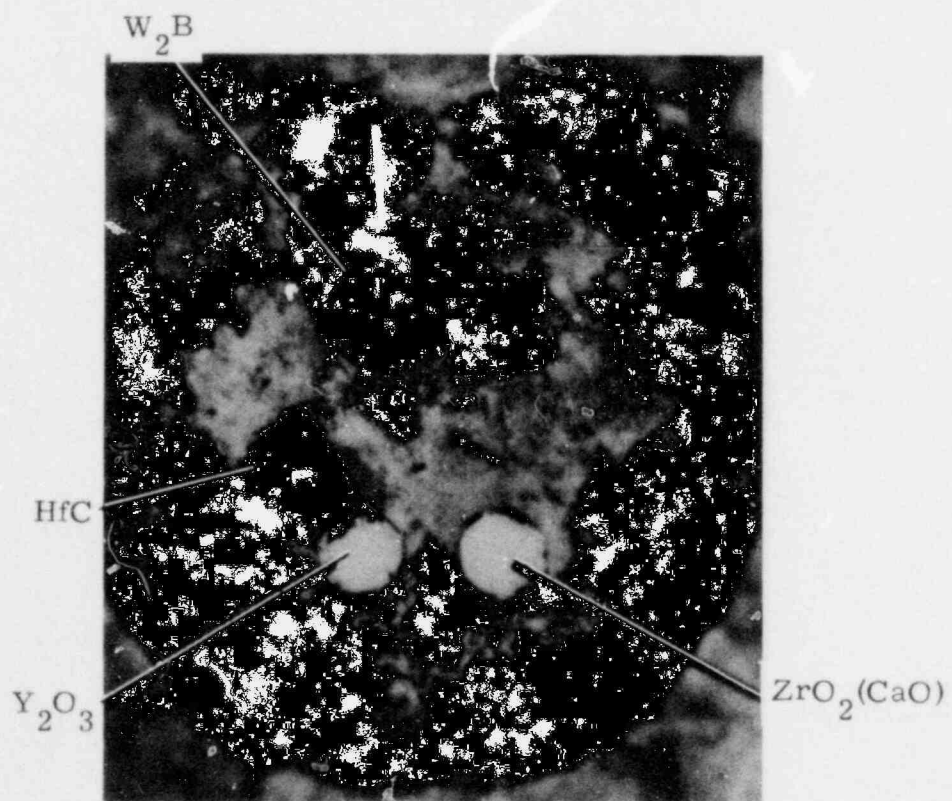


Figure 1-7. Concrete/Steel Interface, BURN 0 Test

The impact of the melt on the specimens may be summarized as follows:

- W₂B - badly eroded and powderized
- HfC - powderized on surface
- Y₂O₃ - fractured internally; powderized on surface
- ZrO₂ - (CaO stabilized) - fractured internally; powderized on surface.

A photograph of the undersurface of the steel is shown in Figure 1-8.

It appears that none of the materials considered in BURN 0 test would be suitable for prolonged exposure to the melt. Yttrium oxide was the best behaved of the samples, but it too suffered from thermal shock.

Posttest dissection of the crucible showed that the electrodes had alloyed with steel at their tips (Figure 1-9). Some melting of this alloy occurred. The electrodes were not shorted together by metal.

1.2.5 Further Analysis of Data From BURN 1 Test

Details of the BURN 1 test have been described elsewhere.⁷ One of the most important pieces of data that came from this test was the motion picture record of the x-ray image of the melt during the test. Frame-by-frame analysis of this record has been undertaken to determine (1) the time of contact between the melt and the concrete, and (2) how swelling of the melt produced by gas evolved during the melt/concrete interaction.

Sketches of the pool, which in the BURN 1 test was primarily a metallic pool, were made at 1-s intervals. The width of the pool was measured at 30 or more locations. The mean and maximum pool widths were computed from these measurements. The time dependence of the mean and maximum pool depths are shown in Figures 1-10 and 1-11, respectively. Pool depths are normalized by dividing by the calculated depth of a 100% dense steel melt weighing 832 g.

As may be seen in these figures the pool is substantially swelled by gases. For the small pool used in BURN 1, this swelling can be as much as 250% of the gas-free pool depth.

The relationship between pool swelling at the rate of gas evolution is of interest. Gas generation data from BURN 1 test are shown in Figure 1-12. The regression of mean pool level swell against the rate of gas generation is shown in Figure 1-13. It appears that at the highest generation rates level swell is roughly independent of gas generation rate. At gas generation rates below about 150 L/min (superficial velocities of 2.4 m/s), level swell is almost a linear function of gas generation rate (superficial velocity). At very low gas generation rates, data become very noisy. Low gas generation rates developed in BURN 1 when the melt was beginning to freeze. The viscous, two-phase melt was elevated and deformed as a body by single bubbles during this period.

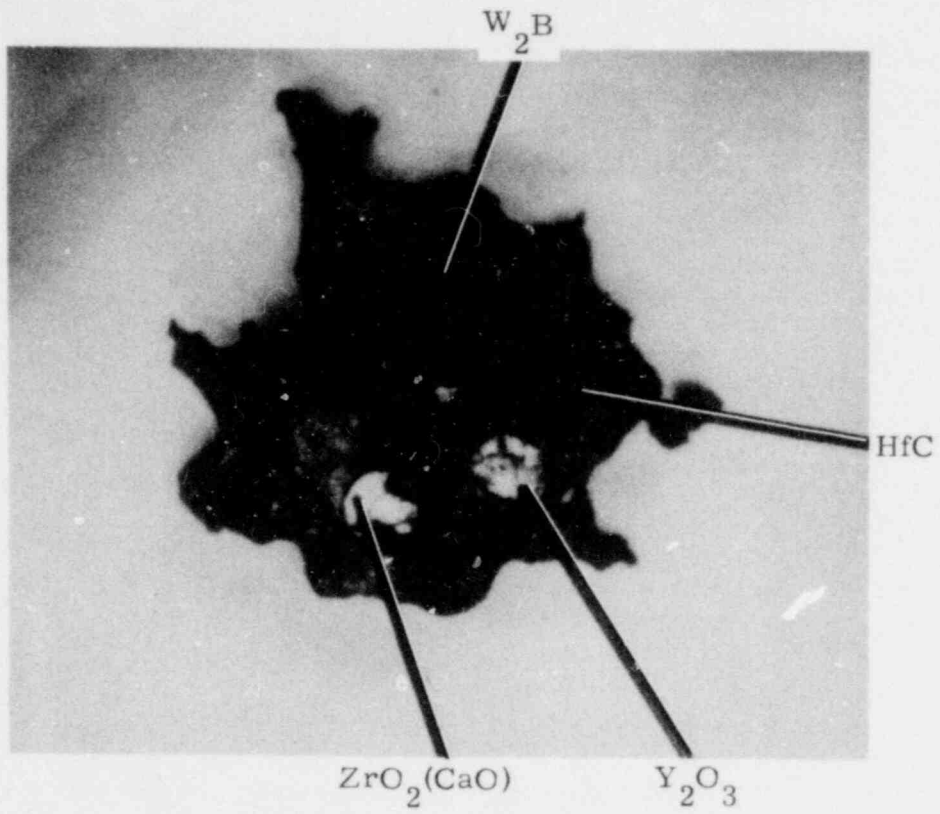


Figure 1-8. Undersurface of Steel Showing Included Refractory Material



Figure 1-9. Alloyed Electrodes Used in BURN 0 Test

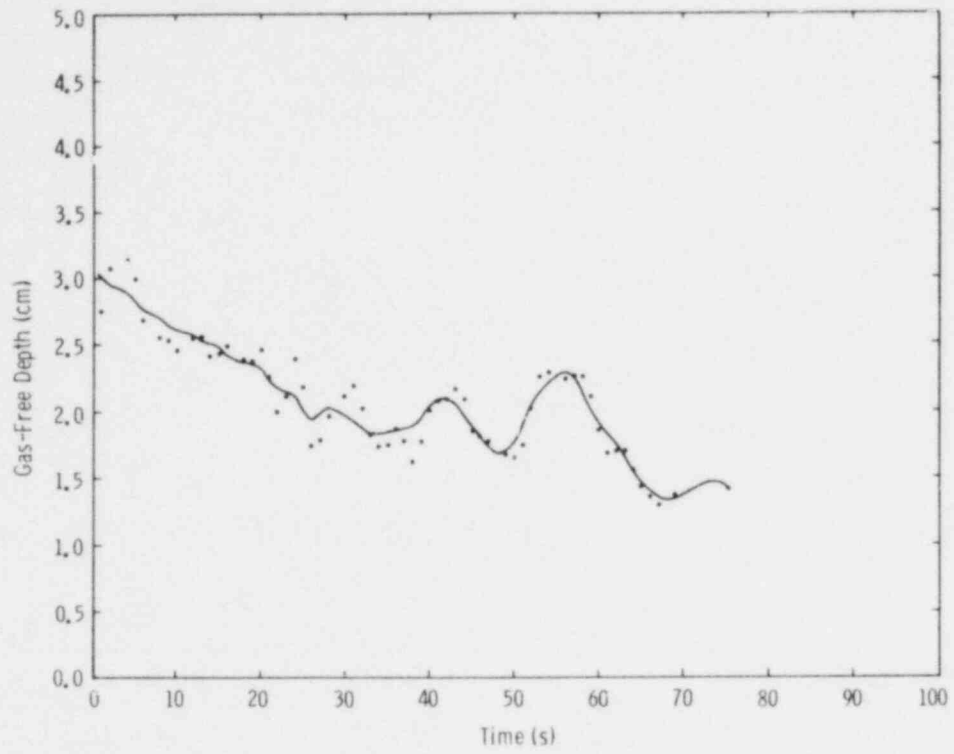


Figure 1-10. Level Swell (mean) in BURN 1 Test

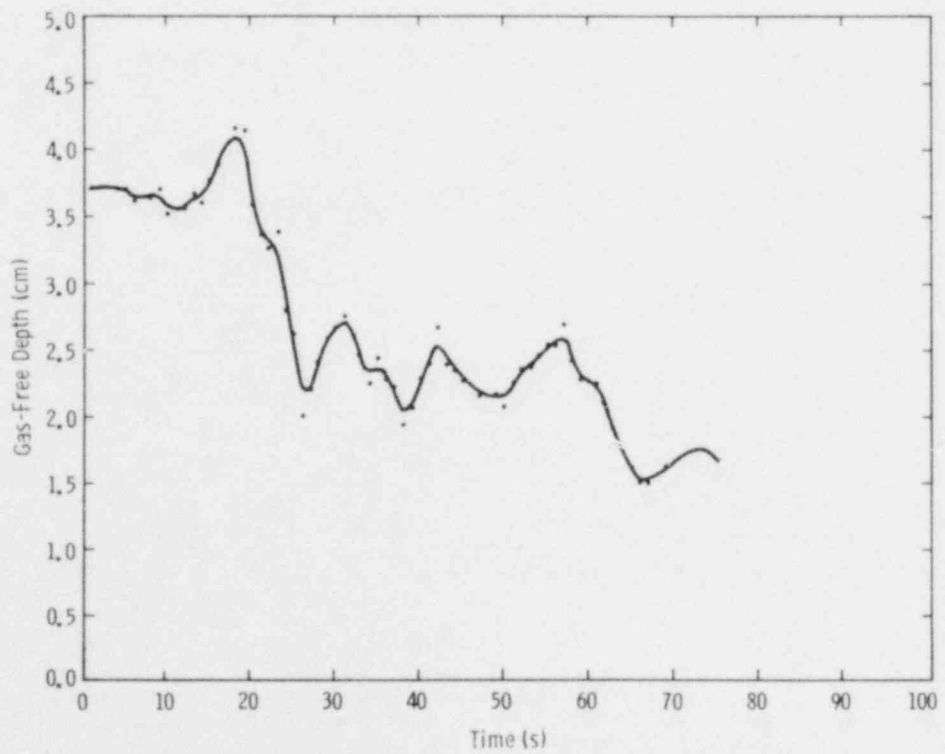


Figure 1-11. Level Swell (maximum) in BURN 1 Test

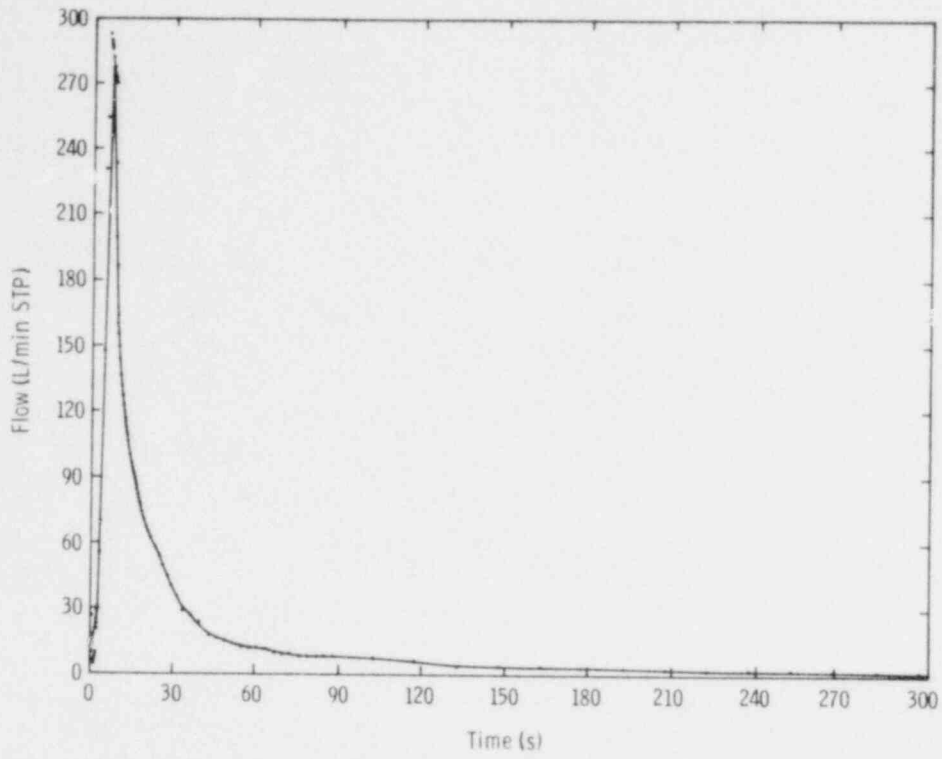


Figure 1-12. BURN 1 Gas Flow Data

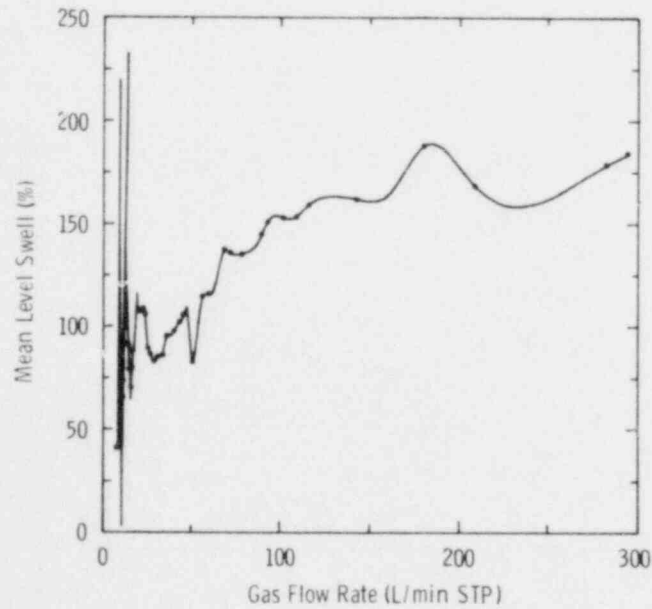


Figure 1-13. Plot of the Percentage of Mean Pool Swell Due to Entrained Gas vs the Rate of Gas Flow for the X-Ray Monitored Test

The quantitative aspects of the relationship between gas generation rate and pool swelling observed in BURN 1 may not be applicable to a much thicker melt. This is especially true for the magnitude of pool swelling. The general shape of the relationship, i.e., a region at high gas generation rates during which swell is independent of gas generation rate and a region where swell is strongly dependent on gas generation rate, would be expected for any melt. Confirmation of this point will be considered in the x-ray test series.

Melt contact with the concrete was noted for the nine locations defined in Figure 1-14 for each frame of the x-ray image (about 0.04-s intervals). Subjective decisions concerning contact were necessary, especially for points near the centerline of the crucible cavity since the melt is truly three-dimensional but the image is only two-dimensional. Resolution with the x-ray technique is limited to about ± 0.3 cm. Further, a light "halo" developed about the perimeter of the very dense melt where it was adjacent to the much less dense concrete. Contact between melt and concrete could not be more accurately defined than ± 0.3 cm or within the halo region. These limitations on the x-ray technique prevent positive identification of a gas-film separating the melt and concrete if that film is less than 0.3 cm thick.

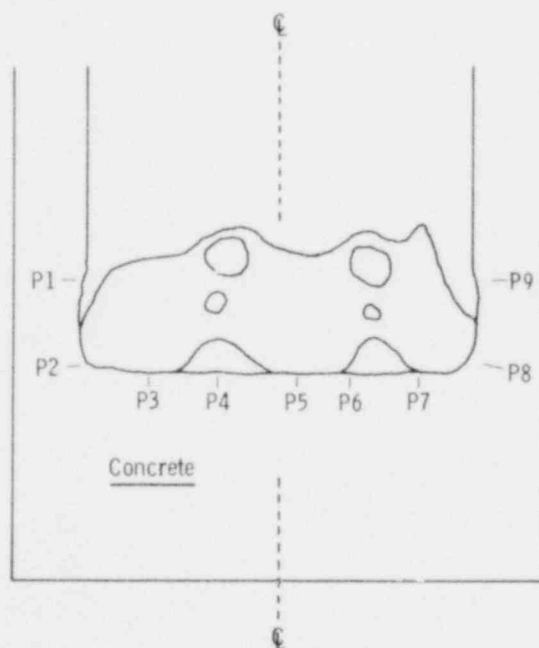


Figure 1-14. Schematic Diagram of Gas Evolution at a High-Temperature Melt/Concrete Interface

Observations of melt contact were averaged over 1-s intervals and mean contact times and standard deviations of these means were calculated. These results are presented in Table 1-VII and Figures 1-15 through 1-23. A piece-wise least squares, smoothing polynomial line has been drawn through the data in the figures. These smoothing polynomial lines are compared for points P5 through P9 in Figure 1-24.

TABLE 1-VIII

Mean Percent of Time Melt in Contact with Concrete at Various Locations and Time Intervals
(standard error of mean in parentheses)

Location*	Time Intervals (s)							
	<u>0-9</u>	<u>10-19</u>	<u>20-29</u>	<u>30-39</u>	<u>40-49</u>	<u>50-59</u>	<u>60-67</u>	<u>0-67</u>
P1	31(6)	56(5)	46(5)	48(3)	51(5)	33(4)	4(7)	40(20)
P2	59(9)	87(6)	92(1)	93(1)	89(2)	88(1)	91(4)	86(16)
P3	66(10)	89(6)	97(1)	96(2)	84(3)	68(6)	42(9)	79(20)
P4	19(5)	29(13)	33(6)	31(3)	12(2)	13(2)	3(3)	21(18)
P5	59(5)	74(4)	89(4)	95(2)	94(3)	83(7)	66(4)	80(16)
P6	64(15)	48(7)	29(4)	30(2)	17(3)	9(3)	7(1)	30(23)
P7	40(3)	48(6)	79(14)	91(2)	79(5)	73(2)	62(1)	68(22)
P8	84(3)	92(2)	94(1)	97(1)	95(1)	91(4)	90(2)	92(9)
P9	25(5)	40(4)	44(4)	48(1)	46(3)	41(3)	68(16)	45(22)

* Locations depicted in Figure 1-14.

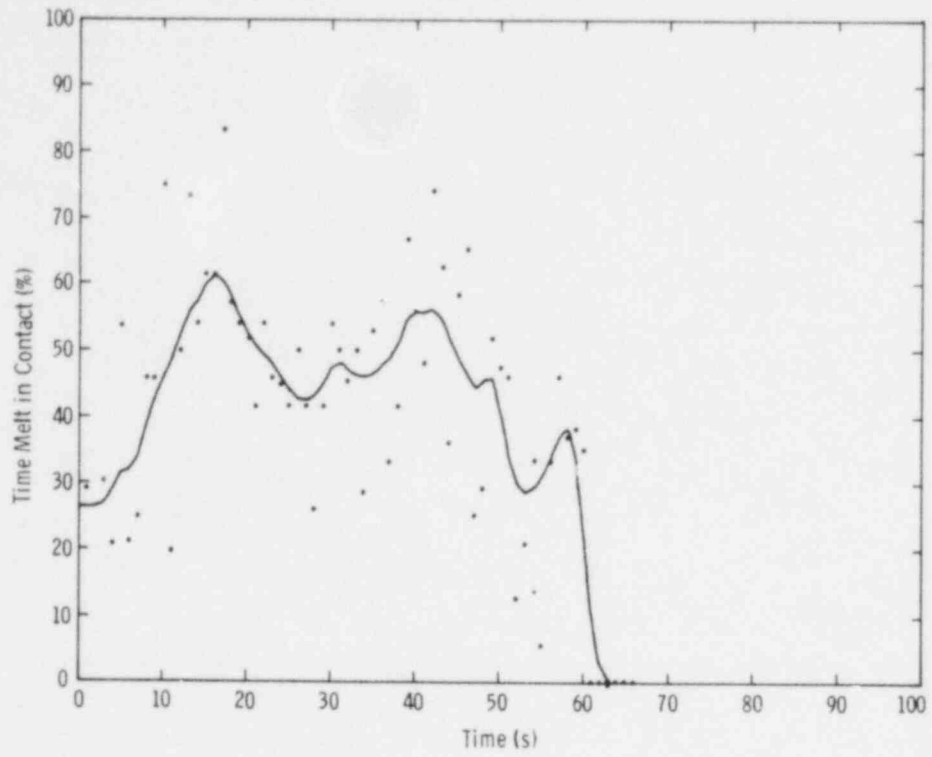


Figure 1-15. Contact Times for BURN 1 at P1

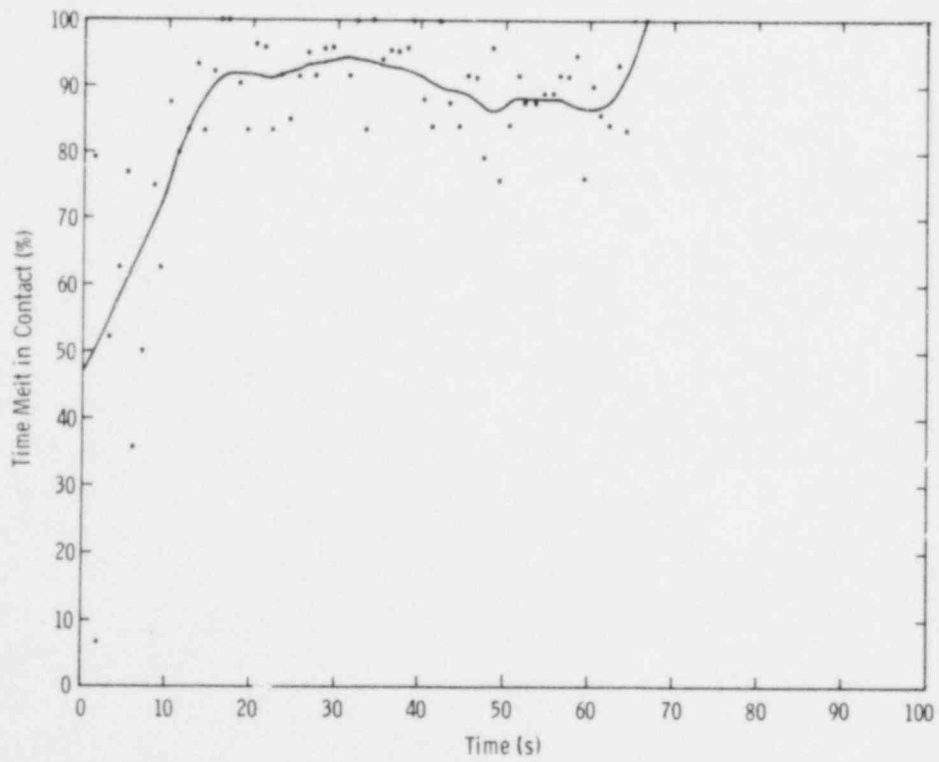


Figure 1-16. Contact Times for BURN 1 at P2

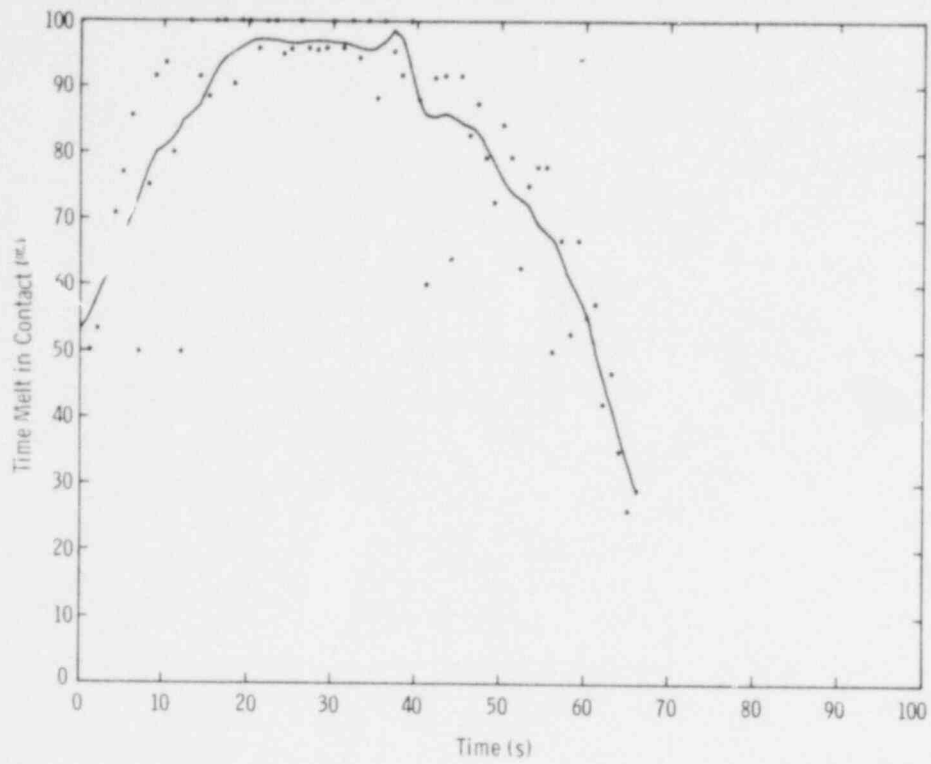


Figure 1-17. Contact Times for BURN 1 at P3

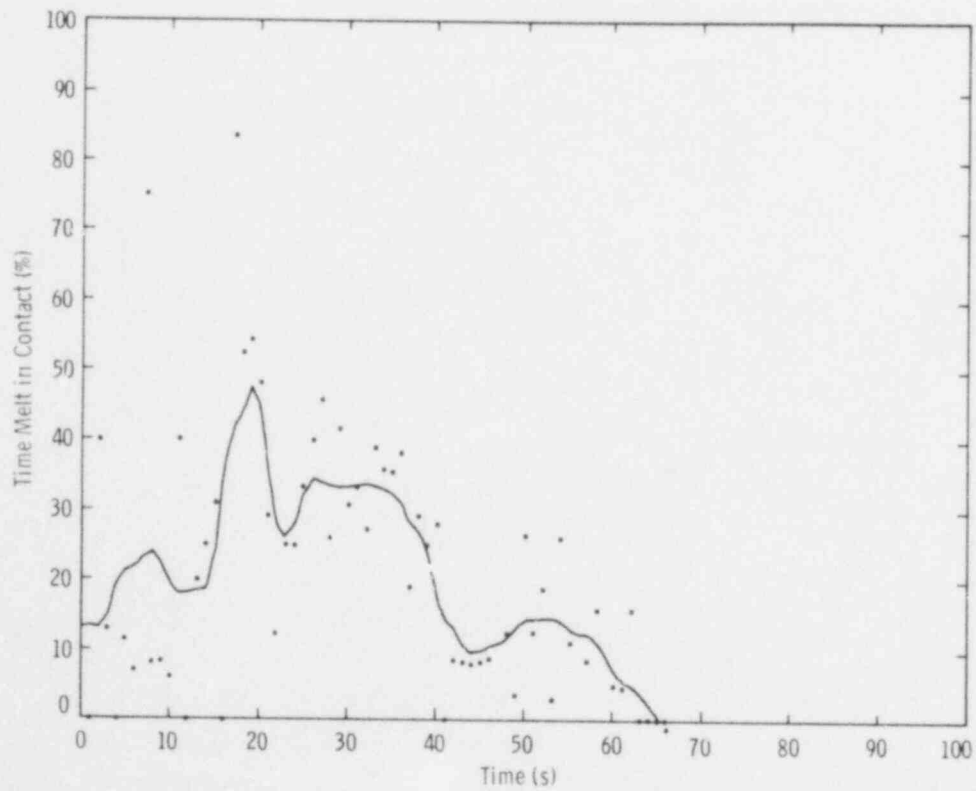


Figure 1-18. Contact Times for BURN 1 at P4

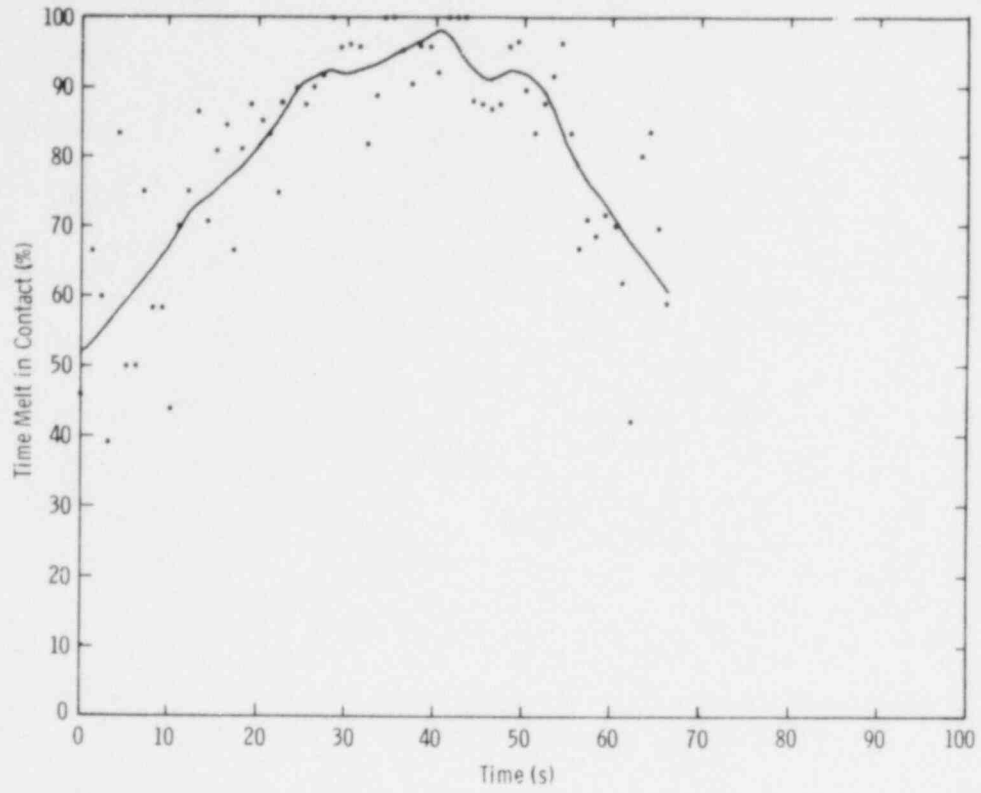


Figure 1-19. Contact Times for BURN 1 at P5

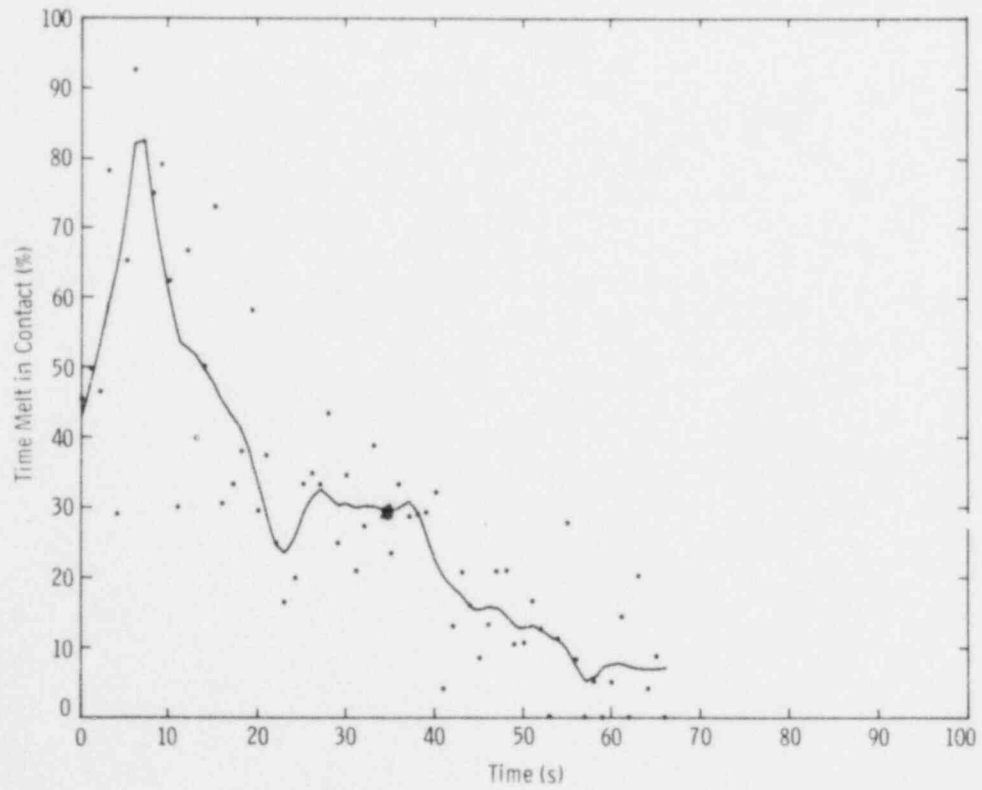


Figure 1-20. Contact Times for BURN 1 at P6

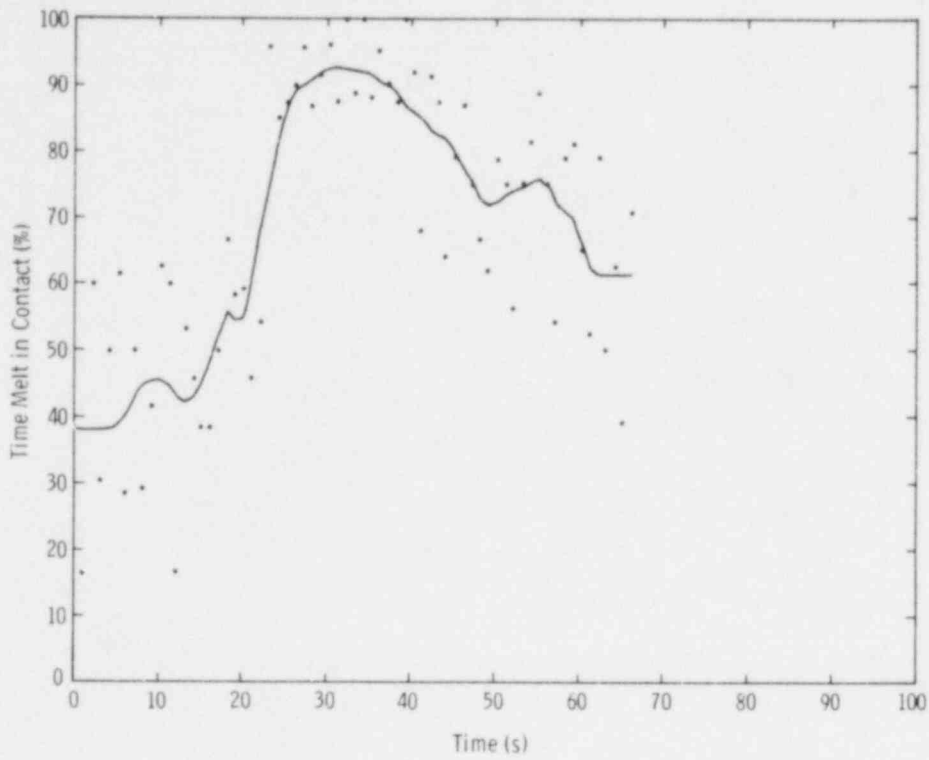


Figure 1-21. Contact Times for BURN 1 at P7

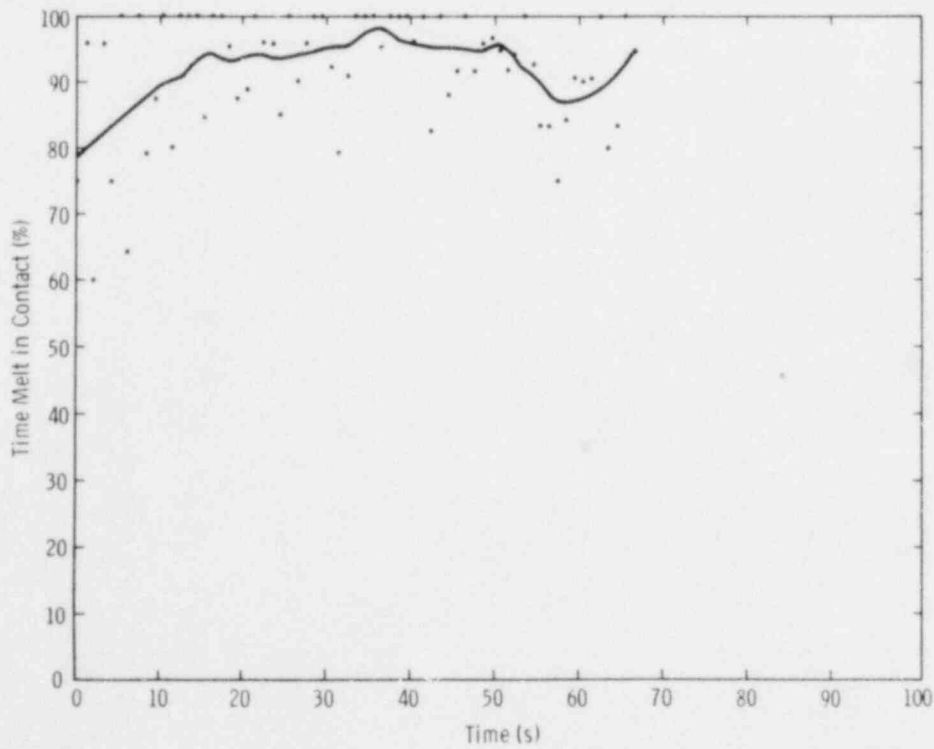


Figure 1-22. Contact Times for Burn 1 at P8

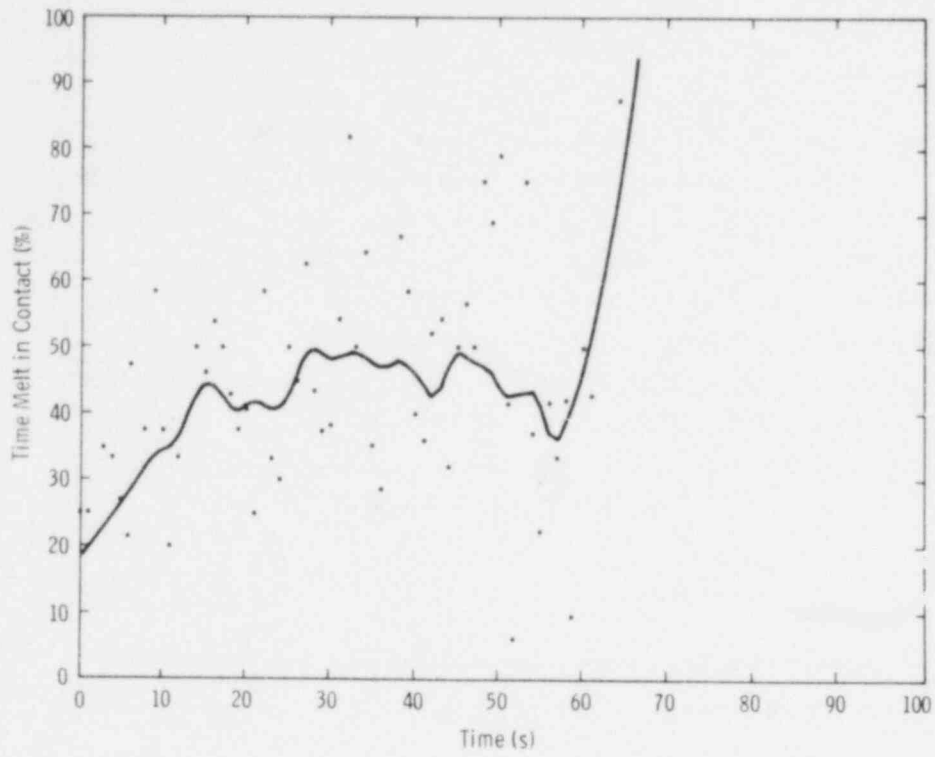


Figure 1-23. Contact Times for BURN 1 at P9

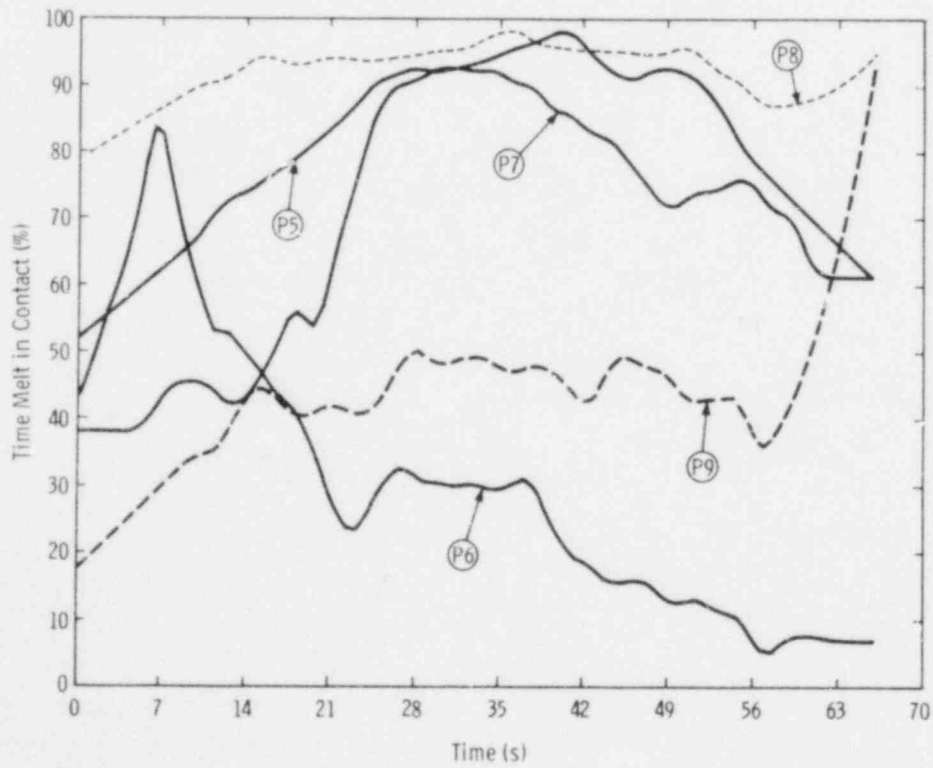


Figure 1-24. Contact Times for BURN 1 Test

The quantitative data again reflect the qualitative observations made above concerning pool behavior. The melt has approximate symmetry about the point P5. Points on the cavity walls near the top of the pool (P1 and P9) are contacted by the melt only 40% to 50% of the time. Melt froze in contact with point P9 and away from point P1 at the end of the test. Points near the corners created by intersection of the cavity walls with the cavity bottom (P2 and P8) are apparently contacted by the melt 80% to 90% of the time during the so-called "steady-state" portion of the interaction. This is also true for points P3 and P7 on the bottom of the cavity near the walls. Melt contacts these points less often toward the end of the test when the melt is viscous and gas bubbles at the interface cause more global disturbances in the melt.

Points P6 and P4 are at the sites of localized gas emissions described above. Melt is in contact with these points only 20% to 30% of the time. Interestingly, these points also correspond to the sites of maximum concrete erosion.

The point P5 nearest the centerline is in contact with the melt about 70% of the time. This point corresponds to the point of least concrete erosion at the base of the cavity.

Efforts to measure bubble sizes and residence times from the x-ray image were largely unsuccessful. During the period of violent melt agitation, distinct bubble did not develop. During the steady-state period, gas bubbles formed and broke free of the interface within single frames (~0.04 s). The melt depth was too small to monitor bubble travel through the melt. Transit times were less than 0.04 s during the first 30 s of the test. Transit times were about 0.08 s during the last 20 s. Bubble sizes were about 0.5 to 2 cm in diameter, somewhat larger than the sizes of crevices formed by gas bubbles entrapped in the solidified melt.

1.3 Molten Core/Concrete Interaction Analytical Program

CORCON development activities continued during the quarter with emphasis on phenomenological model development and programming and numerical concerns.

1.3.1 Phenomenological Model Development (A. S. Benjamin, F. G. Blottner, J. F. Muir, and D. A. Powers)

The Equilibrium State Procedure (ESP) program developed by ACUREX/Aerotherm Corporation was received in October. This model computes the equilibrium thermodynamic and chemical state for a mixture of reacting gases, given the elemental composition and two thermodynamic state variables. Results include the equilibrium mass and mole fractions of up to 30 species (6 elements) specified by the user, and the mixture properties of molecular weight, density, enthalpy, entropy, and frozen specific heat.

Work was initiated on development of a model describing the melt/gas chemical reactions encountered during molten core/concrete interactions. The reactions are modeled using a free

energy minimization technique that treats two subsystems: (1) oxidation of the metallic species in the melt by the concrete decomposition gases (H_2O , CO_2), and (2) reduction of the metallic oxide in the melt by CO and H_2 present in the melt atmosphere. Each subsystem is allowed to reach chemical and thermodynamic equilibrium.

Development efforts continued on models of the following phenomena:

- Concrete ablation and cavity shape change. This model is being developed by ACUREX Corporation and is scheduled for delivery early in the next quarter.
- Heat transfer from the top surface of the molten pool, including convection to the gas atmosphere above the melt and radiation to the atmospheric surroundings.
- Convective heat transfer from the gas atmosphere to its surroundings.
- Convective heat transfer from the periphery of the melt (i. e., the melt/interface-region boundary around the sides and bottom of the pool) to its interior.
- Gas bubble velocities, volume fraction, and pool level swell.

1.3.2 Programming and Numerical Concerns (L. S. Dike, M. A. Ellis, J. F. Muir, and W. H. Van Devender)

Early in the quarter, a primitive CORCON program (containing mostly dummy subroutines) was written, coded, and checked out. The various subroutines included are tabulated in Figure 1-25, which parallels the computation sequence defined previously.⁷ Several of these subroutines have been completed, incorporated into CORCON, and checked out:

DATAIN	Reads all control parameters and input data required for a computation.
DATPLOT	Provides two types of computer plot routines for presenting results. The first presents the variations of selected parameters vs time; the second plots the shape of the concrete cavity at prescribed times. The latter facilitates the production of computer movies of the cavity growth with time.
GEQUIL	Computes the thermochemical equilibrium state of an ideal gas mixture. The ESP program developed by ACUREX Corporation was brought up on the CDC 7600 and checked out by using the sample problem provided. It was subsequently modified to be compatible with CORCON, inserted as a subroutine, and checked out.

- VISRHO Computes the density and viscosity of complex silicate melts. It is a modified and greatly simplified version of the VISRHO code developed by D. A. Powers.⁸ It allows extrapolation to oxidic melts having SiO₂ concentrations and temperatures outside the ranges of 35 to 81 mole % and 1200° to 1800°C, respectively, which characterize the viscosity data base used in developing the original VISRHO.
- GVISCON Calculates the dynamic viscosity and thermal conductivity of equilibrium gas mixtures. This model was extracted from the REALG code developed by F. G. Blottner⁹ for computing the thermodynamic and transport properties of real gas mixtures. It was modified to meet the requirements of CORCON, inserted as a subroutine, and checked out.

In addition to the above programming efforts, work continued on a study of the numerical aspects of INTER and CORCON. The purpose of this study is to identify problem areas in INTER and to investigate and recommend improved numerical techniques for use in CORCON. An examination of INTER revealed that Newton's method is used four times, with various convergence criteria, for solving nonlinear equations. Replacing these sections of the code with the math library routine ZEROIN, which uses a modified secant method, and specifying at least three digits of accuracy resulted in a 5% increase in run time, for the same time step, over the unmodified code. Specifying at least nine digits of accuracy resulted in an 11% increase in run time. With either accuracy specification, the results (e.g., melt temperatures) were found to converge very nicely for the given time step.

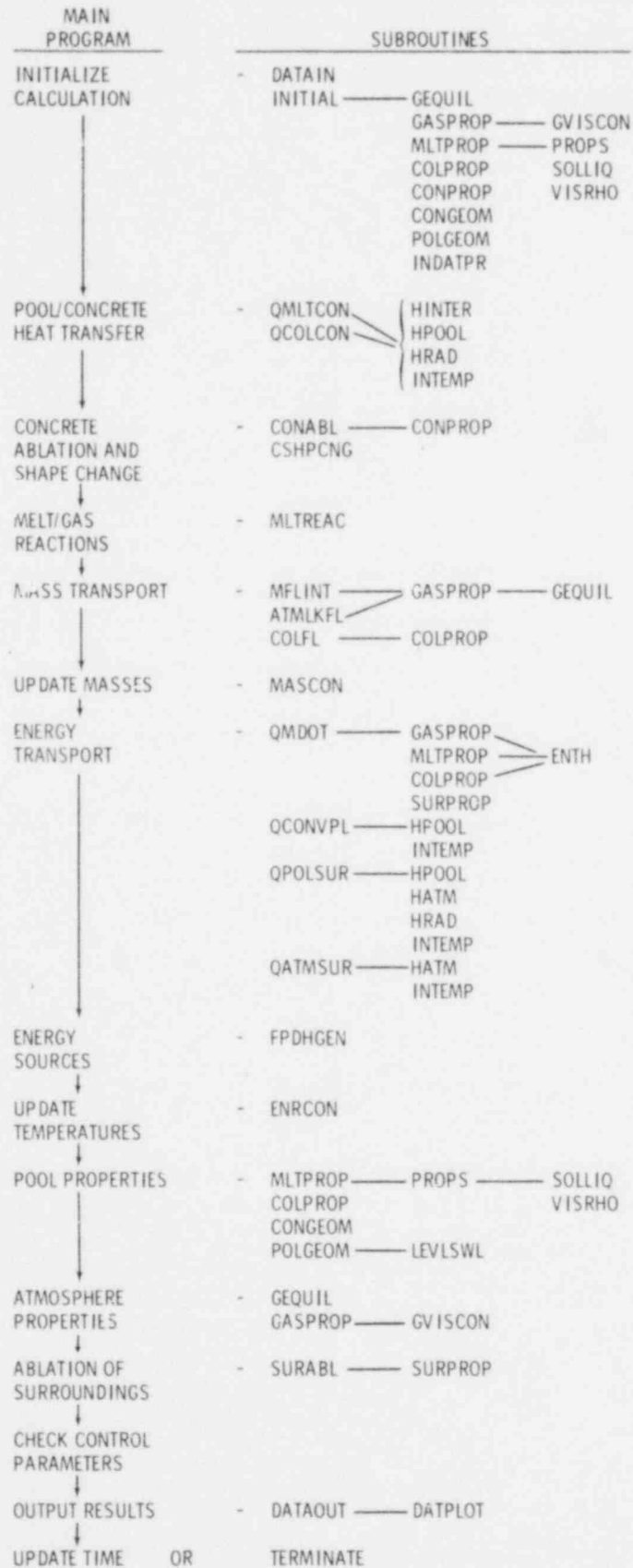


Figure 1-25. CORCON Program Structure

References for Section 1

1. D. A. Powers, Molten Core - Concrete Interactions Project Description, Schedule 189 No. A-1019, Sandia Laboratories, Albuquerque, NM, October 1975.
2. D. A. Powers, Sustained Molten Steel/Concrete Interactions Test, SAND77-1423, Sandia Laboratories, Albuquerque, NM, June 1978.
3. T. Z. Harmathy, "Thermal Properties of Concrete at Elevated Temperatures," Jour. of Materials, V. 5, No. 1, March 1970, pp. 47-74.
4. D. A. Powers, "Influence of Gas-Generation on Melt/Concrete Interaction," Proceedings of IAEA International Symposium on The-modynamics of Nuclear Materials, Julich, FRG, January 29 - February 2, 1979, Paper No. 58, to be published.
5. T. Z. Harmathy and L. W. Allen, "Thermal Properties of Selected Masonary Unit Concretes," ACI Journal, February 1973, pp. 132-142.
6. Light Water Reactor Safety Research Program Quarterly Report, July - September 1978, SAND79-0359, LWR Safety Department, Sandia Laboratories, Albuquerque, NM, April 1979.
7. Light Water Reactor Safety Research Program Quarterly Report, April - June 1978, SAND78-1901, Nuclear Fuel Cycle Safety Research Department, Sandia Laboratories, Albuquerque, NM, January 1979.
8. D. A. Powers and A. W. Frazier, VISRHO: A Computer Subroutine for Estimating the Viscosity and Density of Complex Silicate Melts, SAND76-0649, Sandia Laboratories, Albuquerque, NM, June 1977.
9. F. G. Blottner and D. E. Larson, Calculation of Real Gas Properties for MHD Channel Flows, SAND78-1361, Sandia Laboratories, Albuquerque, NM, September 1978.

2. Steam Explosion Phenomena (L. D. Buxton,
W. B. Benedick, M. L. Corradini,
D. E. Mitchell, L. S. Nelson)

2.1 Summary

The purpose of the steam explosion phenomena program is twofold: (1) to experimentally identify the magnitude and the characteristics of pressure pulses necessary to trigger and to propagate explosive interactions between water and molten LWR core materials, and (2) to develop criteria to assess the probability and consequences of steam explosions during a hypothetical meltdown accident in an LWR. The efforts in the program encompass five areas:

- Small-scale triggering experiments using simulant molten materials (Corium-A, Corium-E, iron oxide ~ 15 g) with water in a floodable arc melter. These experiments are directed toward understanding the applied triggering pressures needed to generate steam explosions under a variety of initial conditions.
- A large-scale, open geometry test series using thermally generated melts (iron-alumina ~ 25 kg) dropped into water. These experiments are primarily directed toward determining the explosive interaction potential of these high-temperature melts at large scales so that subsequent closed geometry tests may be better designed.
- The large-scale, closed geometry, fully instrumented test series using induction-generated melts (iron oxides, Corium-E ~ 25 kg) dropped into water. These experiments are directed toward observing at larger scale and with prototypic melts, the efficiency and propagation of the explosion as a function of fuel and coolant temperatures, mass ratios, and composition.
- Theoretical analysis of steam explosions. This theoretical work is directed toward helping interpret the observed experimental results in light of past theories and models of steam explosions (vapor explosions), and supplying additional modeling effort where past work has proven inadequate. The ultimate objective is to be able to relate the experiments performed and the results obtained to the possible behavior of a steam explosion during a meltdown accident by using a consistent modeling and scaling analysis.
- Assessment of containment failure resulting from steam explosions. This effort is directed toward evaluating how a steam explosion may lead to containment failure by missile generation or overpressure conditions, and to identify and evaluate the realistic mechanisms that could dissipate the explosion energy and reduce the probability of containment failure.

2.1.1 Triggering Experiments

Triggering experiments were performed with iron oxide, Corium-A, and thermite melts this quarter.

By measuring the gaseous oxygen evolved from iron oxide starting materials during arc melting, it was possible to determine the instantaneous melt composition during steam explosion triggering interactions. By comparing the melt compositions just before flooding with the debris retrieved after the steam explosion occurred, using wet chemical analyses, it was found that,

within experimental error, there was essentially no difference between the oxygen content of the two materials. It was also shown that heating times of the melts correlate poorly with their final composition at flooding time.

It has been concluded that little, if any, gaseous oxygen is evolved during the steam explosion triggering interaction in molten iron oxides ($\leq 2 \text{ cm}^3$ at STP conditions). Moreover, a critical composition region for explosions has been identified.

Triggering experiments were attempted with a four-component simulant of a highly metallic Corium-A. These melts were difficult to form and probably were multiphase during the interaction with the flooding water. Explosions could not be triggered.

Eight laboratory scale experiments were performed by flooding thermite melts (iron plus alumina) with water and, shortly afterward, applying a pressure transient. These experiments were intended to complement the steam explosion efficiency studies being performed in the field. It was not possible to initiate explosions with the thermite melts on this small scale, whether using bridge-wire or detonator stimulation.

2.1.2 Efficiency Studies Summary

Forty-eight field experiments involving 1 to 27 kg of metallothermic-reaction-generated mixtures of molten aluminum oxide and iron have been performed in this study. Steam explosions occurred in 37 of the 48 experiments. Most of the explosions occurred spontaneously at seemingly random delays from pour initiation. Both single and multiple explosions were seen. When multiple explosions occur, one is frequently more energetic than the others. The spontaneous triggering mechanism is unknown but is suspected to involve contact of the melt with the interaction vessel walls or similar solid surfaces at least for the slower pour rates. Coating the interaction vessel walls with lard was shown to reduce the incidence of spontaneous explosions under these conditions. However, recent data taken at high pour rates seem to indicate explosion initiation with no solid surface involvement. Steam explosions can also be artificially triggered using high-explosive detonators with no apparent enhancement in efficiency.

The largest explosion obtained was estimated to have converted about 1.34% of the thermal energy of the melt (assuming 3.1 kJ/g) into work. That particular experiment had a slightly different geometry than most in that a heavy metal plate was placed over the top of the tank. The second most efficient explosion converted almost 1% of the melt's thermal energy into work. The remainder of the explosions had estimated efficiencies of less than 0.6%.

Measurements taken during several explosions indicate pressurizations decaying over several milliseconds with peak pressures normally between 2 and 7 MPa. Narrow spikes to even higher pressures were occasionally seen. Rise times to peak pressures were usually less than 0.5 ms and frequently less than 0.1 ms, but the shape of the pulse is not what one would expect

from a continuous coherent interaction. Rather, it appears that the explosions might involve several smaller explosions which are only loosely coherent in time.

The debris generated in the field-scale efficiency experiments look quite similar to the debris produced in the laboratory-scale triggering experiments. Sieve analyses on partial samples of the debris recovered from some of the experiments indicated that the more efficient explosions produced finer particulate.

The most efficient explosions occurred with the greater water depths. This is probably a result of the additional inertial confinement provided by the larger quantities of water. It is probable that there was an enhanced inertial confinement for the experiment with the tank cover. Although the two most efficient explosions both involved only intermediate quantities of melt (~ 5 kg), a fairly efficient explosion (0.43%) was also recently obtained in an experiment for which all of the melt (13.6 kg) was assumed to be in the tank at the time of the explosion. This suggests that the explosion efficiency is not melt-quantity-dependent over the range studied.

Restricting the interaction volume by inserting smaller cylinders in the bottom of the interaction vessel caused no significant change in the explosion efficiency. Neither did the use of hot or boiling water nor the presence of a high vapor fraction created by air injection have any significant effect.

2.1.3 Fully Instrumented Test Series

Work on the fully instrumented test series (FITS) was begun during this quarter and progress was made on the initial setup and design of the experiment. A preliminary design of the interaction chamber was completed and is shown in Figure 2-1. Static overpressure and dynamic loads are being used to specify the chamber strength and size. A subcontract has been let for assistance in design, procurement, and installation of the apparatus. A 50-kW power supply, induction furnace, and controller and recorder have been obtained to be used in developmental activities and possibly some tests. A 100-g sample of Corium-E was prepared and melted in this facility and is now being analyzed. Finally a remote experimental site has been selected and is presently being modified by plant engineering for the FITS experiments.

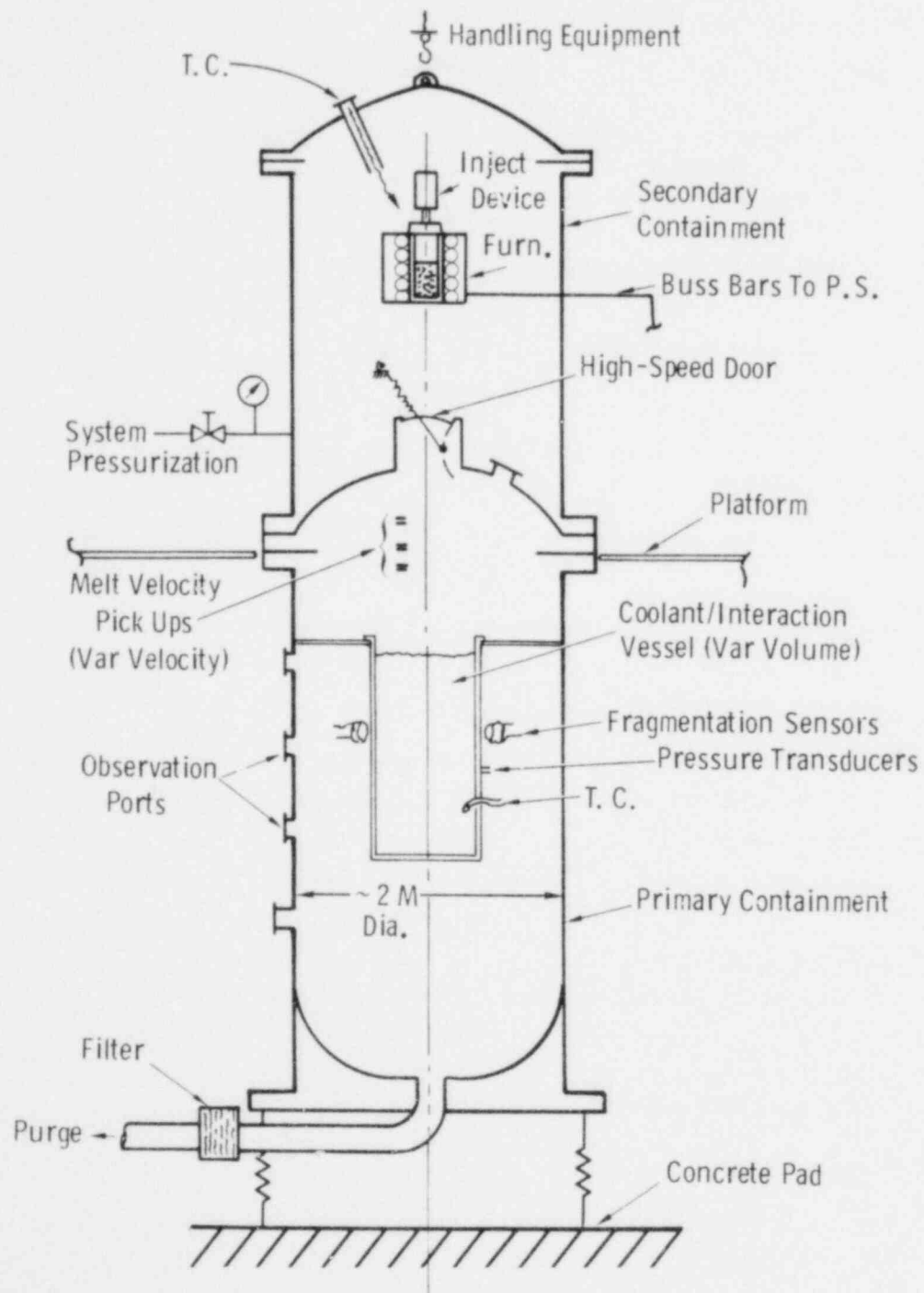


Figure 2-1. Schematic of Interaction Chamber

2.1.4 Theoretical Analysis

Phenomenological modeling of steam explosions this quarter addressed two areas: (1) analysis of small-scale triggering experiments by Nelson, and (2) identification of possible fragmentation and heat-transfer mechanisms that might govern the propagation of the explosion for larger scale experiments. A literature search was begun to determine the thermophysical properties of iron oxides as a function of oxygen content in an effort to identify the reason for the observed compositional cutoff of explosions. Recent results of Nelson, identifying the oxygen content of the melt before the interaction, were used to determine the potential for gas-release-induced fragmentation. The result does not conclusively prove the gas release hypothesis. The observed explosion cutoff at high ambient pressures or water temperatures may have a common explanation, viz, that the vapor film boiling regime separating the melt and the water does not collapse because the bridgewire pulses for these initial conditions are not energetic enough. Thus, the observed cutoffs might be eliminated if the trigger is increased in energy. The mechanisms for the propagation of the interaction are being modeled to determine the characteristic times and processes that might dominate the propagation phase.

2.1.5 Assessment of Containment Failure

In the area of assessment of containment failure, two results were obtained during this quarter. First, before reactor vessel head impact, heat transfer between the hot coolant vapor and the cold coolant above might be a dominant energy-dissipation mechanism. This phenomenon occurs as the coolant above the explosion is accelerated from the lower plenum toward the reactor vessel head. The potential exists to reduce the expansion work of the steam explosion by at least a factor of 2. Second, in analyzing the potential for missile penetration of the containment structure, it was estimated that very little of the missile energy (10% to 20%) is used in penetrating the containment structure for missiles with energies derived from a steam explosion with a conversion ratio of 1%.

2.2 Triggering Experiments (L. S. Nelson)

2.2.1 Determination of Instantaneous Composition of Iron-Oxygen Melts at Interaction Time

The oxygen evolution experiments started last quarter (experiments Nos. 10-104-1, 10-110-1, 10-111-1, 10-113-1, and 10-113-2 in the last quarterly report) were continued here. These experiments were performed with the electrochemical gaseous evolved-oxygen analyzer inserted in the argon exhaust flow from the arc melter. The objective of these experiments was to determine the instantaneous average compositions of the melts at the time of flooding. (See Figure 2-11 in previous quarterly report.¹) As shown in Table 2-I, 18 experiments were performed by using hematite (Fe_2O_3), magnetite (Fe_3O_4), or mixtures of magnetite with iron powder (to achieve less oxidic initial compositions). Also, the debris retrieved from each exploding interaction was analyzed by wet chemistry.

TABLE 2-I
Summary of Results of Triggering Experiments^a

Starting Material	Experiment No.	Sample Weight (g)	Water Temperature (K)	Melt Temperature (K)	Transient Generation	Delay Time (s)	High-Speed Photos (R)	Remarks	
Fe_2O_3	10-118-1	14.97	291.8	NM	BW	0.204	400	Spheroidal fragments with some material remaining on hearth	
	10-119-1	14.94	298.8	2140	BW	0.204	400	Fine fragmentation	
	10-119-2	14.93	290.4	2096	BW	0.250	400	Fairly coarse fragmentation	
	10-120-1	14.94	288.7	1962	BW	0.224	400	Sample remains as one piece	
	10-120-2	14.95	294.5	1931	BW	0.208	400	Fragmentation	
Fe_3O_4	10-121-1	14.94	289.7	2119	BW	0.199	400	Fragmentation	
	10-121-2	15.01	289.1	2082	BW	0.255	400	Fragmentation	
$(Fe_3O_4 + Fe)^a$	10-122-1	14.90	288.7	2021	BW	0.236	400	Coarse fragmentation and flat platelets	
$(Fe_3O_4 + Fe)^b$	10-122-2	14.92	287.6	1962	BW	0.205	400	Very coarse fragmentation	
$(Fe_3O_4 + Fe)^b$	10-124-1	14.80	283.3	1915	BW	0.107	400	No fragmentation	
Fe_2O_3	10-124-2	14.94	288.2	NM	BW	0.226	400	Moderately fine fragmentation	
	10-125-1	14.97	282.9	NM	BW	0.170	400	Fine fragmentation	
	10-125-2	14.98	284.9	NM	BW	0.001	400	No fragmentation, BW fires as sleeve rises.	
	10-126-1	14.95	288.1	1919	BW	0.210	400	Fragmentation	
	10-126-2	14.98	285.5	1927	BW	0.168	400	Fragmentation	
	10-127-1	14.97	286.3	1780	BW	0.194	400	No fragmentation	
	10-127-2	14.94	283.0	1986	BW	0.184	400	Fragmentation	
	10-128-1	14.96	282.9	1838	BW	0.227	400	Fragmentation	
	Metallic Corium-A ^c	10-128-2	14.95	289.2	1784	BW	0.189	400	Difficult to keep entirely molten. No fragmentation. Glossy appearance. Metallic interior.
		10-129-1	14.90	284.9	1922	BW	0.255	125	Difficult to keep entirely molten. No fragmentation. Exterior is glossy black. Interior not metallic.
		10-129-2	14.51	279.4	2174	None	NM	125	No fragmentation. Glossy black.
$(Fe_3O_4 + Al)$ Thermite	10-130-1	14.55	284.0	1981	BW	0.437	400	No fragmentation. Sample in one piece.	
	10-117-1	10.2	288.1	NM	BW	0.205	400	Incomplete withdrawal of sleeve. No fragmentation. Metal globule atop black oxidic base.	
	10-130-2	36.2	277.0	NM	BW	0.149	400	Sleeve only partially rises. No fragmentation. Metallic globule within puddle of black oxide.	
	10-131-1	37.1	281.1	NM	BW	NM	400	Sleeve down at time of BW firing. No fragmentation. Metallic flat disc in frozen puddle of black oxide.	
	10-131-2	35.2	276.8	1684	BW	0.253	400	No fragmentation. Metallic glob nested in black oxide.	
	10-132-1	35.4	277.2	NM	DET	0.295	400	No fragmentation. Sample off hearth. Metallic glob nested in black oxide.	
	10-132-2	37.6	279.1	1654	DET	0.199	400	No fragmentation. Deformed metallic portion pulled from black oxide.	
	10-133-1	38.0	277.1	1860	DET	0.099	400	No fragmentation. Deformation of both metallic and oxidic portions.	
10-133-2	38.4	282.8	1772	DET	0.088	400	Shreds of metallic portion scattered in chamber.		

^a 55.1 at. % initial oxygen content.

^b 52.4 at. % initial oxygen content.

^c 39.3 at. % initial oxygen content.

^a In these experiments, 1.5 l of flooding water was used; melting atmosphere was argon at 0.083 MPa; blast x-ray imaging was not used. NM = not measured; BW = bridgwire; DET = detonator.

The results of the two analyses, one determined by oxygen evolution and the other by wet chemistry, are shown in Table 2-II for each of the 16 experiments in which fragmentation occurred. (Experiment Nos. 10-109-1 and 10-110-1, described in the previous quarterly report,¹ are also included.) In the right-hand column of Table 2-II the difference between the two analyses is indicated and, at the bottom of the table, the average difference in composition between the two analyses is given. At the 90% confidence level, the average difference in C/Fe between the two analyses is +0.0012, (essentially zero) with an uncertainty of +0.0161 and -0.0137; i. e., the two techniques yield ratios which seem to be identical within an experimental error of about ± 0.016 . The skewing of the data is not large, as shown in Figure 2-2 where the two analyses are plotted against each other.

TABLE 2-II

Comparison of Oxygen/Iron Ratios Associated With Steam Explosions
in Iron Oxide Melts, Determined by Two Independent Analytical Techniques

Experiment No.	Initial Ratio at Flooding ^a	Final Ratio After Interaction ^b	Difference Final-Initial
10-109-1 ^c	1.235	1.236	+0.001
10-110-1 ^c	1.251	1.241	-0.010
10-118-1	1.288	1.259	-0.029
10-119-1	1.172	1.157	-0.015
10-119-2	1.291	1.201	-0.090
10-120-2	1.178	1.203	+0.025
10-121-1	1.148	1.195	+0.047
10-121-2	1.177	1.189	+0.012
10-122-1	1.168	1.151	-0.017
10-122-2	1.101	1.133	+0.032
10-124-2	1.219	1.246	+0.027
10-125-1	1.268	1.285	+0.017
10-126-1	1.182	1.226	+0.044
10-126-2	1.260	1.233	-0.027
10-127-2	1.222	1.214	-0.008
10-128-1	1.216	1.226	+0.010

At 90% confidence level, difference = +0.0012 $\left\{ \begin{array}{l} +0.0161 \\ -0.0137 \end{array} \right.$

^a Derived from measuring the O₂ evolved up to water flooding.

^b Derived from wet chemistry analysis of the debris.

^c Flooded with borated water.

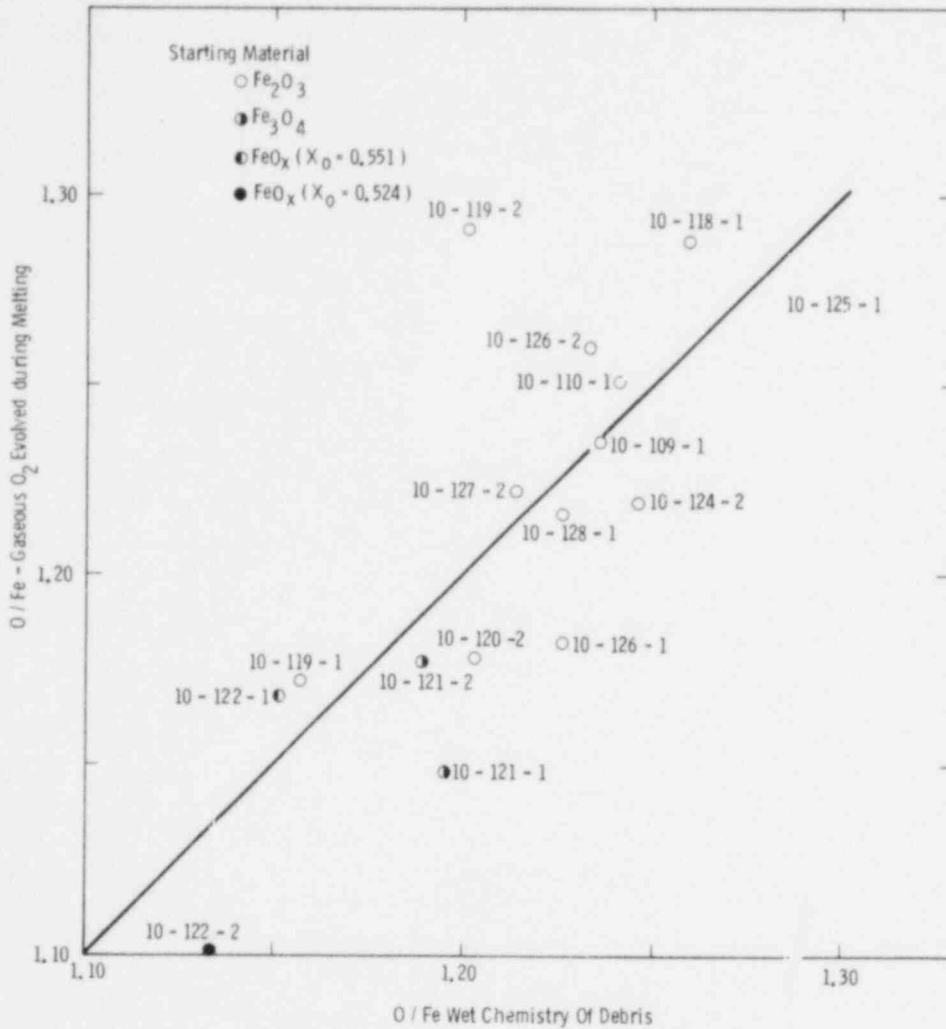


Figure 2-2. Comparison of Oxygen-Iron Ratios Determined by the Evolution of Oxygen During Melting and by Wet Chemical Analysis of the Debris Obtained from an Exploding Iron-Oxygen Composition. Note the absence of any marked skewing of the data.

The instantaneous melt analyses can be used to partially answer a concern which has existed since the beginning of the triggering experiments with decomposable oxides, namely, the relationship between arc melting time and composition of the material at time of flooding. The heating time of the materials, taken from the strip chart records of oxygen evolution during arc melting, and the corresponding compositions at flooding time from Table 2-II are shown in Table 2-III. These data for the four initial pellet compositions used here are plotted in Figure 2-3. It can be seen that there is poor correlation between these parameters.

The ability to determine the instantaneous composition of the iron-oxygen melts can be used to place a true composition scale on plots of peak pressure vs initial oxygen content of the sort shown in Figure 2-4. (This was Figure 2-7 in the April-June 1978 Quarterly Report.²) The maximum stage-2 pressures for the interactions of the 16 analyzed iron-oxide melts (see Table 2-7 with water

are plotted against actual instantaneous composition in Figure 2-5.^{*} Notice that there seem to be explosivity thresholds at both the high-oxygen and low-oxygen ends of a critical region. The cutoffs occur at about C/Fe = 1.11 and 1.27, as shown by the vertical dashed lines. The range of explosivity is indicated on the equilibrium phase diagram of the iron-oxygen system in Figure 2-6.

TABLE 2-III

Tabulation of Heating Time in the Arc Melter and Final Composition of Iron-Oxygen Melts at Flooding Time

Experiment No.	Starting Sample Composition	Heating Time (s)	Composition at Flooding (O/Fe) ^a
10-109-1 ^b	Fe_2O_3 ↓ Fe_3O_4 ↓	206	1.235
10-110-1 ^b		217	1.251
10-113-2		219	1.19
10-118-1		161	1.288
10-119-1		413	1.172
10-119-2		230	1.291
10-120-1		214	1.289
10-120-2		242	1.178
10-121-1		230	1.148
10-121-2		163	1.177
10-122-1	26 wt% oxygen	178	1.168
10-122-2	24 wt% oxygen	160	1.101
10-124-1	24 wt% oxygen	153	1.1
10-124-2	Fe_2O_3 ↓	175	1.219
10-125-1		160	1.268
10-125-2		189	1.254
10-126-1		146	1.182
10-126-2		142	1.26
10-127-1		145	1.264
10-127-2		150	1.222
10-128-1		137	1.216

^a Determined by measuring oxygen evolution.

^b Borated water used for flooding.

^{*} Also included in Figure 2-5 are two points, indicated by the square symbols, for which (only) wet chemical analyses of debris existed before this quarter (see Table 2-III of the April-June 1978 Quarterly Report,² also Figure 18 of the January-March 1978 Quarterly Report³). The excellent agreement between instantaneous melt composition and debris composition, shown in Table 2-II, makes the inclusion of these points seem warranted.

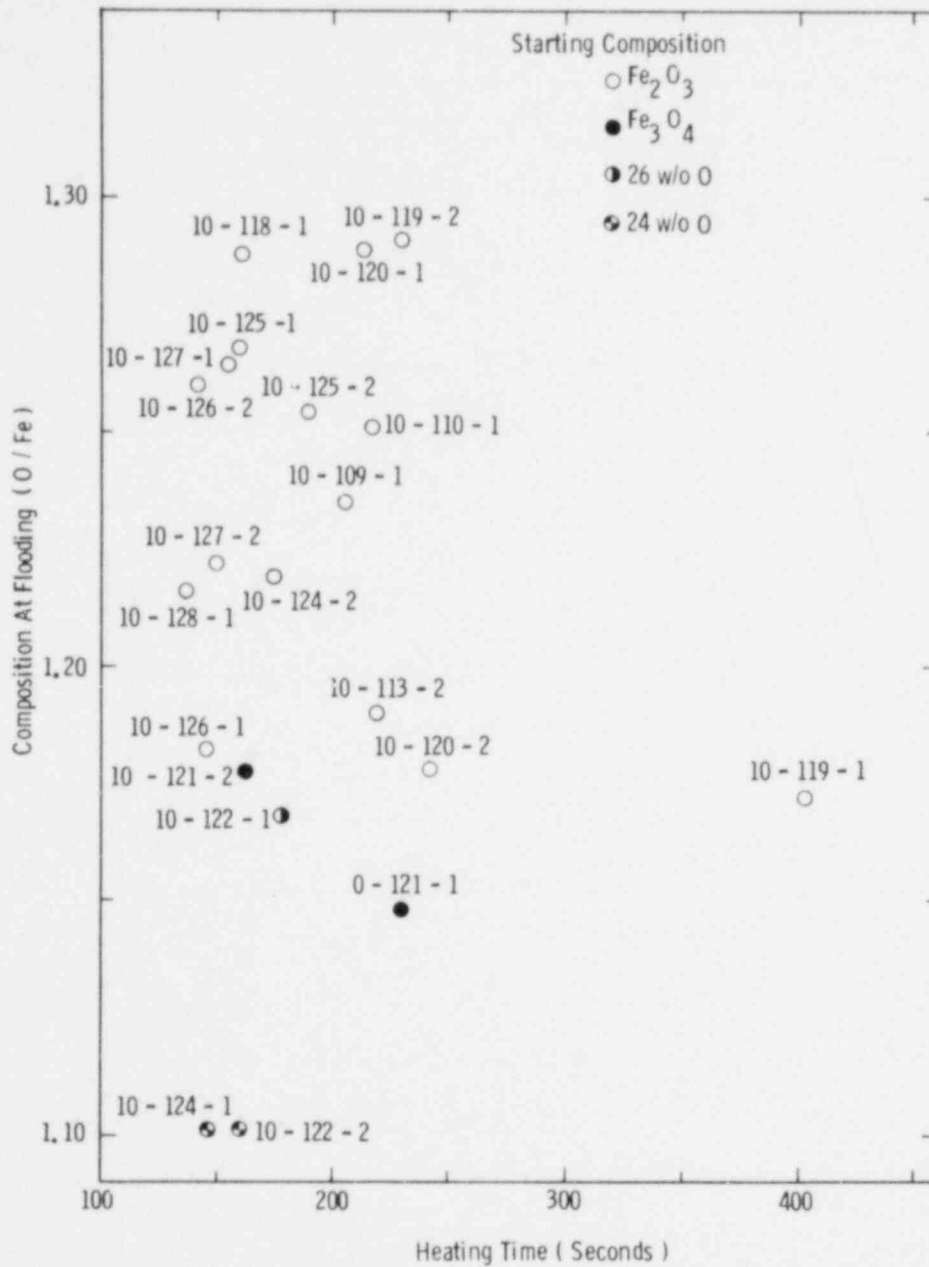


Figure 2-3. Iron-Oxygen Ratio as a Function of Heating Time for Several Starting Compositions. Note that there is little correlation between the ultimate composition obtained at flooding time and the length of time the sample was arc melted. (Data are taken from Table 2-III.)

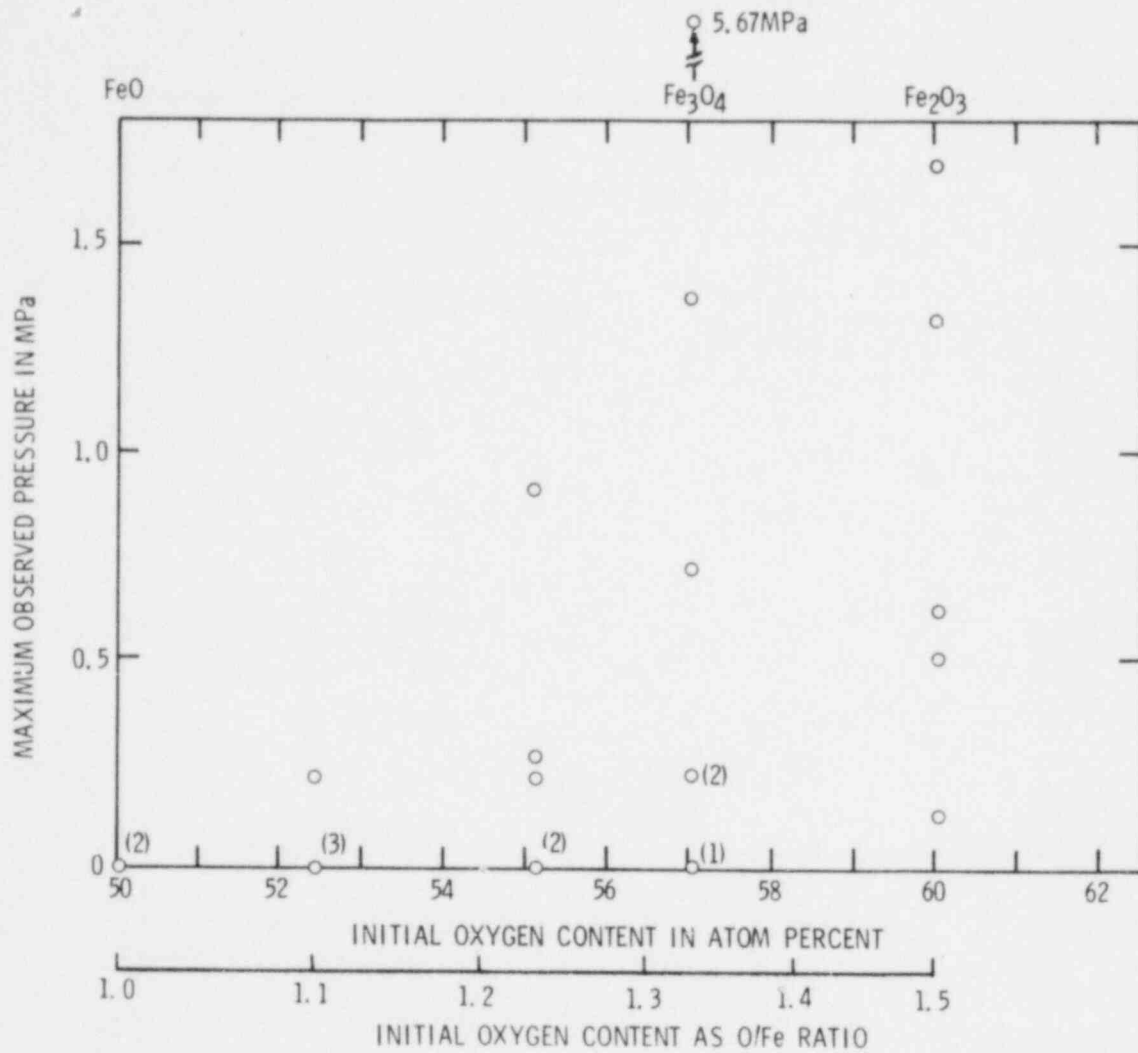


Figure 2-4. Maximum Observed Pressure as a Function of the Starting Composition of the Iron-Oxygen Starting Materials in Steam Explosion Triggering Experiments. These compositions should be compared with actual compositions shown in Figure 2-5. (This figure is reproduced from Figure 2-7, in the April-June 1978 Quarterly Report.)

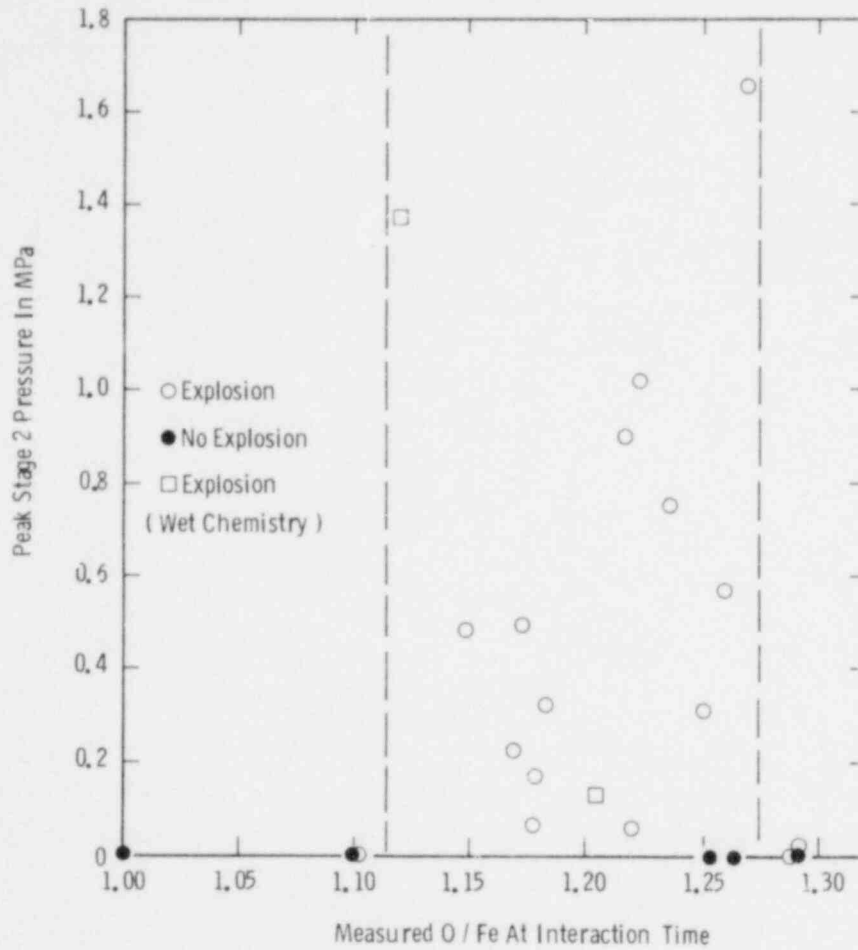


Figure 2-5. Instantaneous Average Compositions of Iron-Oxygen Melts as Measured by the Gaseous Oxygen Analyzer at the Time of Flooding. These compositions should be compared with those shown in Figure 2-4, which are starting material compositions. Note the apparent high and low O/Fe ratio cutoffs observed for these melts. (These data points are for new experiments; they do not represent the same experimental points as shown in Figure 2-4, which are shown here only for rough comparison.)

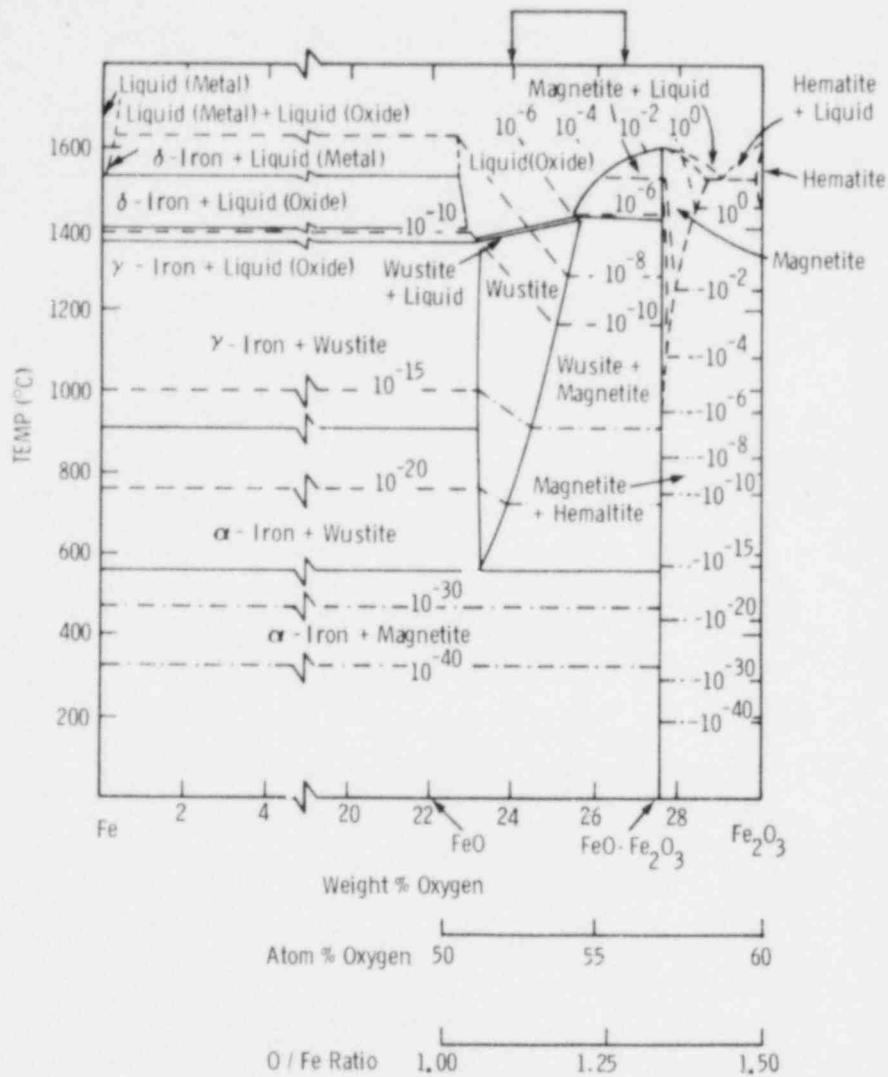


Figure 2-6. Iron-Oxygen Phase Diagram Reproduced From A. Muan, *Bull. Am. Ceram. Soc.* 37 (2), 81 (1958). The arrows at the top of the diagram indicate the region in which explosive interactions have been observed; these are the thresholds indicated in Figure 2-5.

The preliminary conclusions which seem warranted from these experiments are as follows:

- The composition of the debris after an explosive interaction of molten iron oxide with water is identical, within experimental error, to the instantaneous composition of the melt at flooding time.
- There seems to be little correlation between heating time in the arc melter and the final composition of the melt at interaction time.
- If there is gaseous oxygen evolved during the explosive interaction of molten iron oxide with water, the amount is small, $\leq 2 \text{ cm}^3$ at STP within experimental error.
- There is a critical range of melt compositions in which explosions occur under the conditions that prevail in the floodable arc melter, viz, $1.11 < \text{O/Fe} < 1.27$.

2.2.2 Metal-Rich Corium-A Simulants

To complete the series of steam explosion triggering experiments performed with Corium-A compositions, a highly metallic four-component simulant initial composition was studied (in atomic percent, U = 19.7, Zr = 16.1, Fe = 24.9, O = 39.3, taken from the meltdown compositions of M. Peehs⁴). This four-component mixture was difficult to melt and, upon examination of the solidified material, seemed to have been multiphase at interaction time. No explosions were observed, using the conditions indicated in Table 2-I.

2.2.3 Thermite/Water Interactions

Eight experiments were performed with $\approx 37 \text{ g}$ pellets of compacted magnetite/aluminum powder thermite composition. The pellets were ignited by a slight touch of the arc to the top of the pellets as they rested on the water-cooled hearth of the arc melter. The molten material was flooded with water shortly after ignition took place. A bridgewire or detonator was used in the attempt to initiate a steam explosion with this melt. The objective of these experiments was to learn whether explosive interactions of the sort observed in the field with up to 13 kg of similar thermite melts (see Section 2.3) could be initiated on a laboratory scale.

Each experiment yielded a chunk of frozen solid which suggested that clearly separated metallic and nonmetallic melts had coexisted. The solidified metallic phase is silvery, shiny, and magnetic, while the corresponding nonmetallic phase is black and brittle. In the least-disturbed samples, the metallic phase is found nested in a cup-like configuration of the nonmetallic phase (Figure 2-7).

Even though both bridgewire and detonator stimulation were used and also a variety of time delays between flooding and attempted initiation (Table 2-I), it was not possible to initiate an interaction in the arc melting apparatus which could be regarded as a typical steam explosion. It was possible, however, to drive the melt into unusual configurations, 10-132-2, 10-133-1, and 10-133-2 (Figure 2-7). The configuration for 10-132-2 is similar to the detonator-induced deformation in arc melted stainless steel, shown in Figure B-10 of Reference 5.

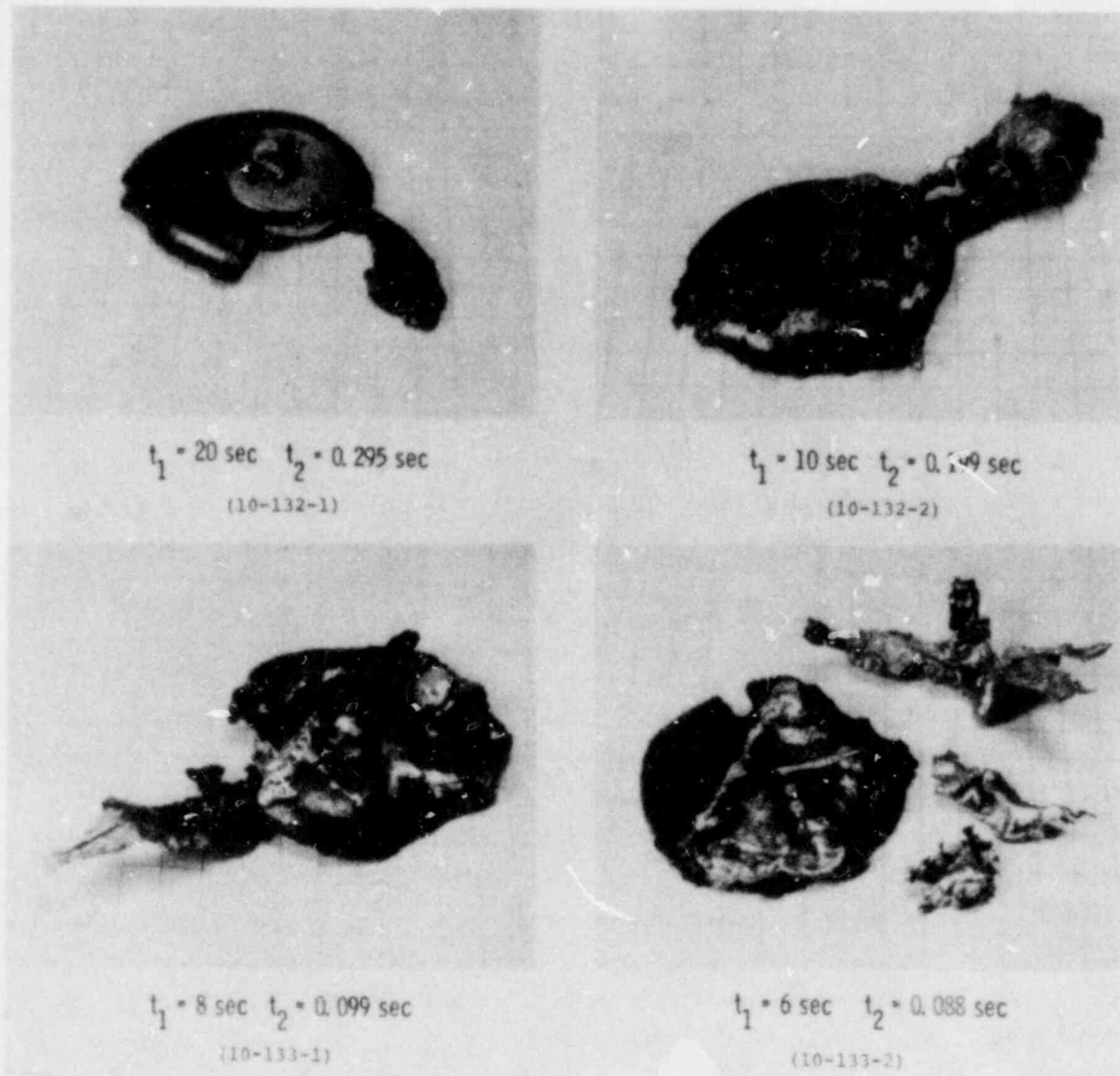


Figure 2-7. Residues From the Interaction of (Fe-Al-O) Thermite Interactions With Water. Initial sample weights were 38 grams. The samples were ignited with a low current in the floodable arc melter apparatus. t_1 is the interval between the ignition and the onset of flooding. t_2 is the interval between the initiation of flooding and the firing of the detonator. Initiation of these interactions was attempted by the use of submerged minidetonators. Grids are 6 mm.

2.3 Efficiency Scaling Studies (L. D. Buxton, W. B. Benedick)

2.3.1 Introduction

The first 40 efficiency scaling experiments that used 1 to 27 kg melts generated by a metal-thermic reaction were reported rather completely in the 4 previous quarterly reports^{1-3,6} and the results of all 40 were summarized in the last quarterly report.¹ Eight additional experiments of that general type are reported here. One of them was performed specifically to investigate the effect of high vapor content in the coolant on the efficiency of large steam explosions (Section 2.3.2). Another was performed in a manner designed to allow a better estimate of the energy of the water slug which is driven from the tank in a steam explosion (Section 2.3.3). The other six experiments were all attempts to rapidly get large quantities of melt into the tank, before the explosion occurred (Section 2.3.4). Table 2-IV contains a summary of the test parameters and results from all eight experiments performed this quarter.

Data obtained using lithium niobate pressure gages in some of the recent experiments will be discussed in Section 2.3.5. Pressure records from wall-mounted quartz gages (installed in the tank in collaboration with D. E. Mitchell) in experiment 48 will also be discussed there. Finally, Section 2.3.6 will present the conclusions derived from these tests and future plans.

2.3.2 High Vapor Fraction Effect Experiment

Since the power to the heaters was shut off a few seconds before the pour was started in the boiling water experiments reported previously, some concern has been expressed that this might have had an effect on the results because the water conditions were not really representative of a vigorously boiling situation. Although the melt should, in fact, immediately reestablish a vigorously boiling situation in the immediate vicinity of the melt, it is not clear how far this high vapor fraction region would extend. Consequently, in Thermite 41, a system was devised to artificially create a high vapor fraction throughout the tank by injecting air into the water. The system was composed of two concentric rings of copper tubing with tiny holes drilled in the walls at many points. The rings were connected to each other and to an air supply hose. The rings were then placed in the bottom of the tank so that the air bubbled up through the water, creating a large vapor fraction in the water. The water visibly simulated vigorous boiling even though it was cold.

An SEI detonator was installed for this experiment to be used in an attempt to initiate an explosion if one did not occur spontaneously. When no explosion had occurred after approximately 2 s of melt pouring, the detonator was fired. It initiated an explosion at 2.34 s after pour initiation which blew ejecta an average of 6 m into the air. The amount of honeycomb crushed in this experiment was considerable and there was also a small amount of plastic deformation of the interaction vessel wall. Based on an assumed melt quantity present of 9.4 kg, the explosion efficiency was estimated to be 0.26%. This value is very consistent with what has been seen previously under similar conditions, so the large vapor fraction had no obvious effect on the explosion except possibly inhibiting a spontaneous triggering mechanism.

TABLE 2-IV

Summary of Efficiency Scaling Experiments

Experiment No.	Primary Test Purpose	Quantity Water (kg)	Water ^a Temperature (K)	Quantity Melt (kg)	Diameter Pour (mm)	No. Explosions	Time to Explosion (s)	Efficiency (%)	Remarks
41	Vapor fraction	820	300	9.4	76.2	1	2.34 ^(b)	0.26	Air injection
42	Slug diagnosis	820	300	6.1	76.2	1	1.22	1.34	Cover plate
43	Pour rate	820	300	9.3	101.6	1	1.16	0.43	4 in. melt plug
44	Pour rate	820	300	9.5	203.2	1	1.89	0.09	Melt link, doors stuck
45	Pour rate	820	300	7.0	203.2	1	0.34	0.04	Some predribbling
46	Pour rate	820	300	13.6	203.2	0	-	-	Very slow leak
47	Pour rate	820	300	5.1	203.2	1	0.16	0.07	Very quick explosion
48	Pour rate	820	300	13.6	203.2	2	0.61	0.43	Good quartz gage records

^a Approximate; ambient conditions determine exact temperature.

^b Artificially triggered

2.3.3 Water Slug Diagnosis Experiment

In each of the earlier tests in this series, an estimate of the water slug energy was made by observing the average height above the tank to which the water is expelled and then using that height to determine the potential energy difference. Since it was suspected that the slug actually had more energy than was being determined by this method (it was presumably dissipated by drag forces as the slug broke up) and the motion of the diffuse water front could not be timed very well, Thermite 42 was performed with a cover plate on top of the tank to allow better diagnosis of the slug motion. The cover plate used was about 1.07 m in diameter and 26.2 mm thick. The generator was bolted directly to the plate for a total mass of about 250 kg for the unit. A hole was provided in the plate directly underneath the generator to allow the melt to pour into the water. The cover plate was not bolted to the tank but merely rested on blocks ~ 3 cm thick placed between the tank flange and the plate. The purpose of leaving the gap was to provide room for instrumentation brackets. It should be noted that the fall distance between the melt generator and the water surface was much less than usual since a full tank of water was used.

From the movies of this experiment, we observed a mild pressurization starting very shortly after melt/water contact began which forced some water out of the gap between the tank flange and the cover. At 1.22 s after melt plug failure, there was a single large explosion which occurred spontaneously. The plate and attached generator were blown up and out of the field of view (> 12 m) within 0.25 s. Most of the water and debris stayed within view, although some appeared to be blown just outside the visible area. The plate unit reentered the field of view about 6.5 s after it left. Based upon the total time in flight as well as the estimated initial and final velocities of the plate (both ~ 32 m/s), it appears the unit went 50 to 60 m into the air. Since the water slug stopped considerably before that height and it is reasonable to assume that they had the same initial velocity, the hypothesis that a large fraction of the slug energy is normally dissipated by drag forces seems to be supported.

In addition to the large values for the estimated energies given to the water slug and cover plate, it was also observed that the honeycomb crush was greater in this experiment than ever seen before; all three blocks were absolutely flattened. There was also a minor amount of plastic deformation of the tank walls. Since the total pour time was not observed in this experiment, an estimated pour rate of 5 kg/s was used to determine the melt energy of 18.9 MJ. About 1.34% of that energy was converted into measurable mechanical work. This value is approximately one-third larger than any peak efficiency seen previously. Some of the increase may be due to obtaining a better estimate of the slug energy, or because the large water volume and metal cover provided a greater amount of inertial confinement against the vapor expansion. On the other hand, it could be a random fluctuation.

2.3.4 Pour Rate Effect Experiments

Several previously reported experiments in the series were devoted to the study of pour rate effect. This is believed to be important because any melt which enters the water and freezes before the explosion cannot participate in that explosion. Faster pour rates should reduce the possibility

of that happening. High pour rates are also desirable because of the problem of spontaneous initiation of explosions at early times and the desire to produce explosions with large quantities of melt in the tank.

The previous tests all involved relatively slow pour rates even though attempts were made to use very large melt plugs in tests 31 and 33. The very large melt plugs did not melt uniformly, however. Consequently, in most of the experiments to be reported here, a new generator design was tried which used a dual trapdoor arrangement on the bottom of the generator to quickly open a very large hole. In essence, the whole bottom plate of the generator disappeared with the trapdoor arrangement, making the pour diameter equal to the inside diameter of the generator (~ 0.2 m).

One pour rate effect experiment did use a melt plug. Thermite 43 had a pour hole about 0.1 m in diameter covered with a steel melt plug. The generator design was identical to that used for the last several tests except for the larger pour hole. The time from thermite reaction initiation until melt plug failure was longer than usual for Thermite 43, but the melt stream seemed to develop well and the hole did open completely. At 1.16 s after melt plug failure, there was a single spontaneous explosion. The pour reestablished after the explosion but ended about 2.5 s after plug failure. The efficiency analysis assumed a pour rate of 8.0 kg/s to yield a quantity of melt in the tank at explosion time of 9.3 kg. The efficiency was then calculated to be 0.43%. For such a large amount of melt, this value is relatively high compared to earlier efficiencies (e.g., tests 8, 31, 35, and 38).

Thermite 44 was the first test to use a trapdoor generator. The bottom of the generator consisted of two doors which were hinged on the sides of the generator and connected in the middle by a metal link. Insulation was placed on top of the doors except in the immediate vicinity of the connecting link. The intent was for the thermite reaction to progress down through the generator and melt the connecting link, allowing the doors to fall open. From the movies, it was observed that the first melt started from the generator about 10.2 s after initiation. However, the pour stream did not appear to be very substantial until about 1.25 s after the first melt was visible. Perhaps the initial pouring was only a fast leak through the crack. At 1.89 s there was a single, spontaneous explosion which blew a very large quantity of highly luminous melt into the air (probably that melt which was still falling when the explosion occurred).

The efficiency analysis for this test assumed a pour rate of only 5 kg/s because the initial pour was slow and also because the high-speed film indicated that the doors never opened fully (the hinge tolerance was not sufficient). Even that rate implies 9.45 kg of melt should have been in the tank at explosion time which seems large based on the amount of melt blown about in the explosion. This may be why the estimated efficiency of 0.09% for Thermite 44 is so low.

Thermite 45 was also a trapdoor generator experiment but the method used to hold the doors shut while the thermite reacted was altered somewhat. Instead of a fusible melt link on the inside of the generator, a phenolic tube was slid into two sockets on the outside of the generator, one on

each of the trap doors. An explosive detonator was used to break the tube and allow the doors to open. The purpose of this arrangement was to prevent premature door opening before the thermite had all reacted.

There was also some leakage of melt through the crack between the doors in Thermite 45 but it was fairly small. The detonator to break the phenolic was fired at 14.61 s after ignition of the thermite and the doors seemed to open reasonably well although the view was not very clear. At about 0.34 s after the detonator was fired, there was an explosion which again made a very large, luminous cloud by dispersing the still falling melt. The efficiency analysis tried to account for the fact that the melt does not instantaneously fall the 0.5 m distance to the water by using a melt quantity of 7 kg. With that assumption, the efficiency was estimated to be 0.04% for test 45. Part of the reduced efficiency may be the result of the explosion occurring very high in the tank.

Thermite 46 was intended to be a repeat of Thermite 45 but malfunctioning equipment forced some last-minute rerouting of detonator trigger signals and this was not done properly. Consequently, the detonator to open the doors did not function at the intended time and most of the melt leaked very slowly out of the generator. It leaked for about 30 s total but there was no explosion with this very low pour rate. A small amount of the oxide froze and stayed in the generator.

Thermite 47 was also performed by using the same setup as for Thermite 45. There was also a slight leak in this test before the door-opening detonator was fired, but no luminous melt appeared to fall into the water from the leak. The detonator was fired to open the doors at 9.64 s after thermite ignition and there was an explosion 0.33 s later. From the 64 fps movies it appears that 0.16 s elapsed between first water contact and the explosion. The high-speed movies indicate the time delay could have been as short as 60 ms. Using the larger value and an assumed pour rate of 32 kg/s, an efficiency estimate of 0.07% was determined. Again, the explosion occurred very high in the tank.

Thermite 48 was the final experiment of the quarter and was yet another repeat of the trap-door arrangement used in the last few tests. No leakage was evident in this experiment. The door-opening detonator was fired at 12.52 s after thermite ignition and the pour seemed to develop very quickly. The first melt appeared to get to the water about 0.125 s after the detonator was fired. A mild surface interaction was seen to start at about 0.297 s which disturbed the melt stream somewhat. At 0.609 s after detonator firing, there was a large spontaneous explosion which blew water and debris about 8 m into the air. The cloud was fairly dark, indicating the absence of much hot melt. A spray of water was also blown out the back side of the tank. The generator was torn loose from the frame and blown about 10 m into the air.

The interaction vessel was destroyed in this experiment. There was a vertical tear down the whole back side of the tank, even through the heavy flange. There was also considerable plastic deformation which apparently occurred before the tank fractured. The honeycomb crush was substantial, especially considering the fact that four honeycomb blocks were used instead of three;

this means a third larger than normal forces were required. The efficiency estimate for Thermite 48 was 0.43% and it is assumed that all 13.6 kg of melt were present in the water at explosion time, since the tank was destroyed. It is indeed fortunate that we finally got all or almost all of the melt in the tank before the explosion.

2.3.5 Pressure Measurements

Most of the experiments performed this quarter have had lithium niobate pressure gages installed in the interaction vessel with the signals from them being recorded on an FM tape deck. However, these gages are fragile and do not withstand the severe environment of a steam explosion very well. They frequently produce signals with severe baseline shifts soon after the explosion begins or, sometimes, it appears their time constant is radically reduced due to partial shorting or cracking of the crystal. Therefore, only a few valid traces have been obtained.

Figure 2-8 is one such trace which was recorded during Thermite 41. The time scale is arbitrary as to starting time in all the traces to be discussed. The initial rise is very fast in this record, but the time-to-peak pressure is a few hundred microseconds. There is a very large amount of high frequency ringing in the signal which could be caused by system reverberations or ringing in the gage itself. Since the oscillations are so nonuniform, at least some of the ringing is attributed to many separate explosive events occurring over an extended period of time. The initial spike at ~ 4 ms is attributed to electrical noise when the detonator was fired.

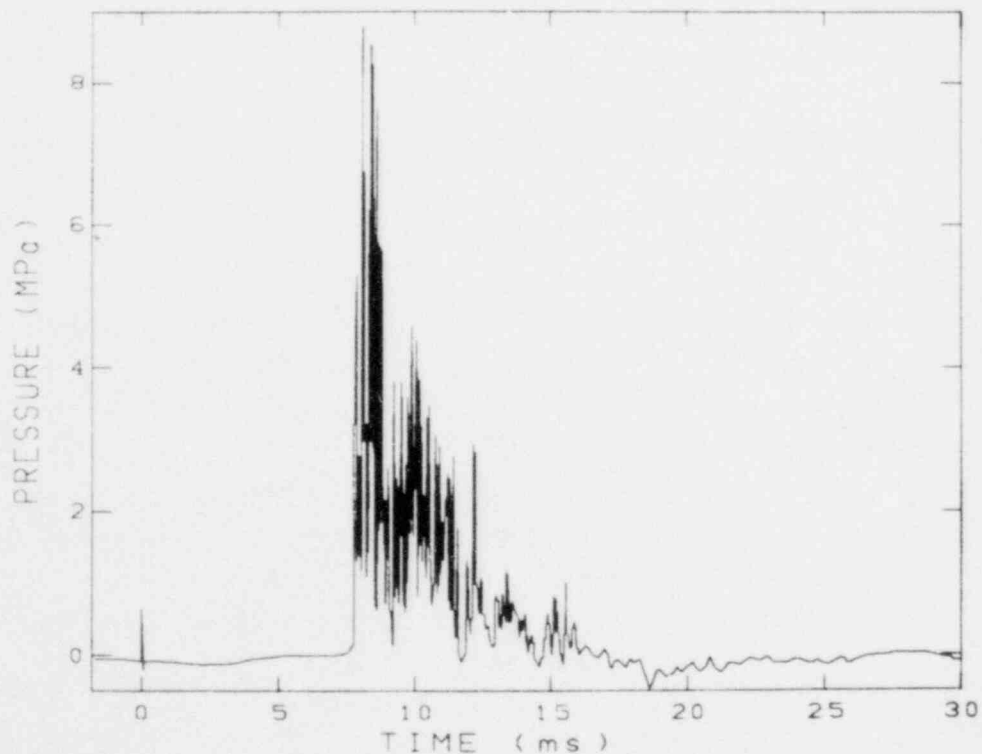


Figure 2-8. Lithium Niobate Pressure Gage Record From Thermite 41

Figure 2-9 is a similar trace from Thermite 43. Again, the time-to-peak pressure is seen to be a few hundred microseconds. The impulse (area under the curve) from that record seems to be a little larger than in Thermite 41, which is consistent with the fact that the efficiency estimate was also larger in Thermite 43.

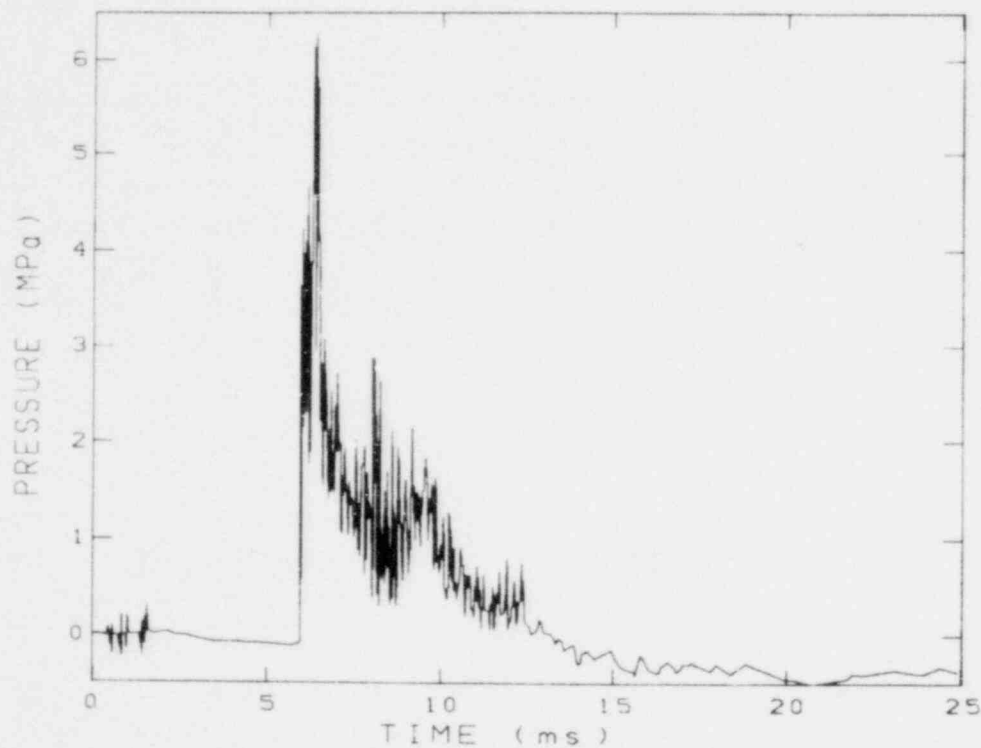


Figure 2-9. Lithium Niobate Pressure Gage Record From Thermite 43

The trace shown in Figure 2-10 from Thermite 44 is quite different in appearance from the two discussed above. The risetime to peak pressure is even longer than seen in Figures 2-8 and 2-9 and the pulse duration is considerably shorter. This is believed to be the result of the explosion occurring very high in the tank and relieving quickly. The impulse is again consistent with the low efficiency predicted for this test.

Figures 2-11 and 2-12 are signals from two different quartz gages (Kistler 606A) installed in the walls of the interaction vessel with the help of D. E. Mitchell. These gages were on opposite sides of the tank about 0.75 m down from the top of the tank, or at about the same level as the lithium niobate gages. Unfortunately, both lithium niobate gages used in this test failed (apparently due to a cracked crystal) so that no direct comparisons could be made. The quartz gage records are shown inverted to indicate that their normal output signal is reversed in polarity from lithium niobate.

The initial rise time recorded is slower than is usually observed with the lithium niobate gages. This is apparently not because of the electronics of the gage since the charge amplifier bandpass should limit the system and it is supposed to be 20 kHz. The risetime to peak pressure is ≈ 0.4 ms, which is consistent with what has been seen before. There again is a high-frequency pressure trace which seems to indicate some incoherence of the explosion. The low-frequency ringing (250 to 500 Hz) may be caused by waves traveling through the tank walls. The total duration of the pulse is about 5 ms for gage 4 which was closest to the vertical rip point. The pulse duration seems shorter for gage 2, but there is another small pulse at ~ 4 ms after the initial rise, so the apparent difference may be due merely to the fact that the gages are nearly a meter apart and may not be seeing the same detailed phenomena.

Combining the information in these traces with the pressure data discussed previously indicates that, although very high pressure spikes sometimes occur, the pressures which last over such a length of time (milliseconds) as to create a real hazard are only a few megapascals in magnitude. Of course, it is not known exactly what steam pressures are reached since the gages are probably not responding directly to a high-pressure steam bubble. Presumably the actual steam pressures are a little higher than the transmitted pressures seen by the gages.

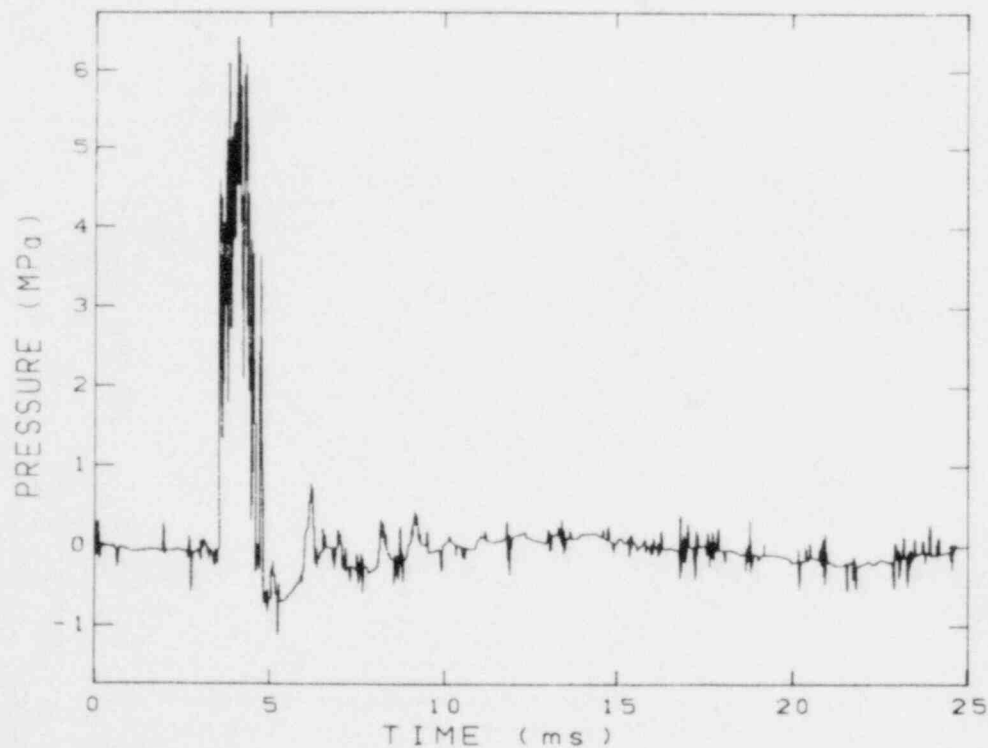


Figure 2-10. Lithium Niobate Pressure Gage Record From Thermite 44

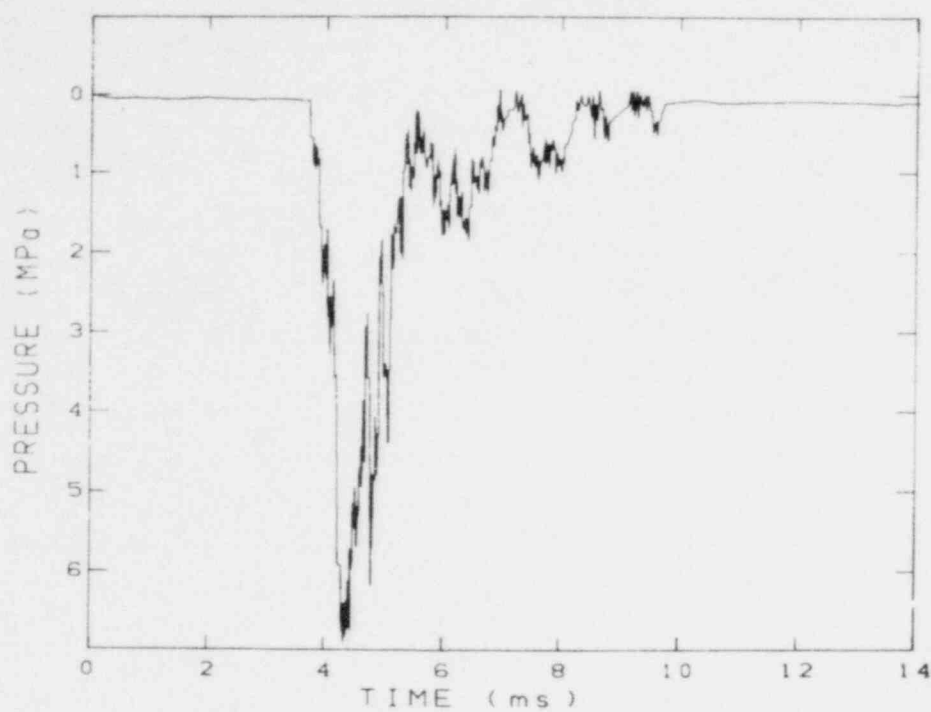


Figure 2-11. Quartz Gage No. 2 Pressure Record
From Thermite 48

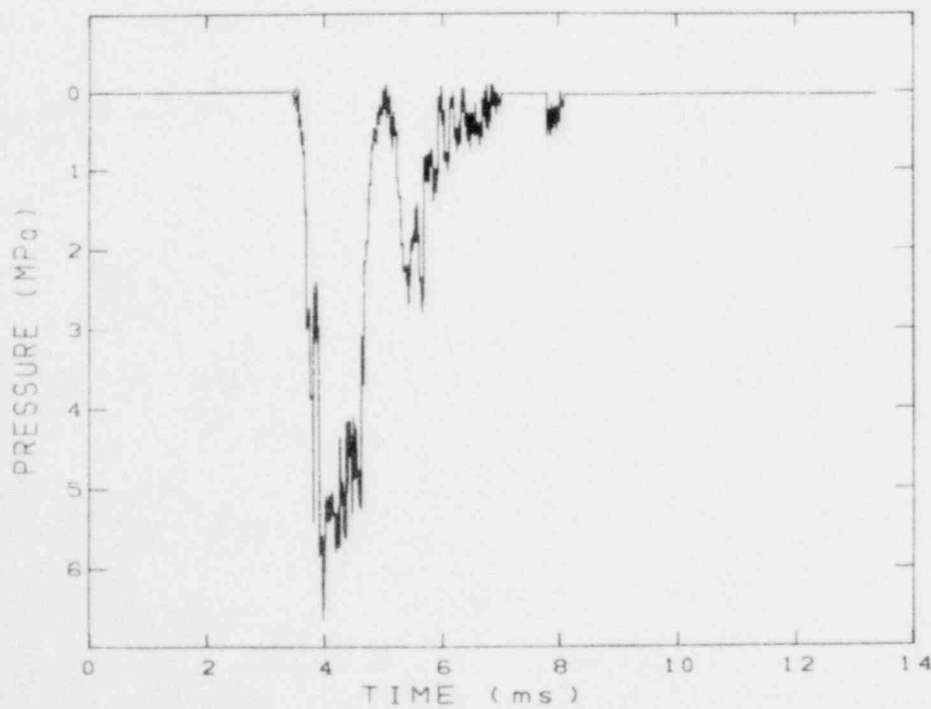


Figure 2-12. Quartz Gage No. 4 Pressure Record
From Thermite 48

2.3.6 Conclusions

The primary conclusion from this latest series of tests is that the decrease in estimated efficiency previously seen for large melt quantity tests was probably the result of the slow pour rate used in those tests since Thermite 48 produced a very efficient explosion. We also concluded that high initial vapor fractions have no significant effect on the explosions. The previous conclusion that all the spontaneous explosions seem to be surface-initiated does not seem to be well supported, at least for larger pour rates.

The current plans for the open geometry tests are to prepare a topical report on the tests already performed and then to perform a few tests with a Corium-type thermitite. Those tests will be reported in a supplemental report.

2.4 Fully Instrumented Test Series (D. E. Mitchell)

The fully instrumented test series (FITS) is a group of experiments planned to follow the open geometry tests conducted by Buxton, et al, and will use realistic simulants in 1 to 25 kg quantities. The objectives are

- Design experiments and apparatus to study the physics of fuel coolant interactions;
- Quantify the thermal-to-mechanical energy conversion efficiency as a function of melt/coolant, mass ratio, temperature, and composition;
- Investigate scaling as related to the conversion efficiency;
- Apply modeling techniques to aid in understanding the interactions.

To meet these objectives, the project has been divided into six major areas: interaction chamber, melt generation methods, instrumentation, site preparation, analysis, and modeling and experiment design. A brief description and progress report on the work in each of these areas follow.

2.4.2 Interaction Chamber

The interaction chamber as planned will be a large pressure vessel designed to contain the interactions. Confinement of the interactions in a chamber is required to protect the melt apparatus and environment from the energy released. A closed system will also enhance the measurement of energy release rates, and containment of the debris will aid in estimating the amount of material which was involved in the reaction. Because of the large quantities of melt and estimated efficiencies, a containment chamber with a large free volume is visualized. Size will be consistent with budgetary and time constraints. Some of the sequential steps in designing the chamber design are

- Estimate design loads from existing open geometry experiments
- Obtain additional engineering load measurements from the remaining open geometry tests

- Specify features necessary for instrument and melt generator installation
- Design the structure to withstand expected dynamic and static loads.

Work during this quarter concentrated on determining the features required for the chamber. The preliminary design shown in Figure 2-1 is primarily intended to describe the overall chamber features.

Static overpressure and dynamic loads are being used to specify the chamber strength and size. Static overpressures have been estimated by using equilibrium thermodynamic methods. Dynamic loads, which are felt to be more severe, are being determined from the open geometry tests being conducted by Buxton, et al.

During this quarter, pressure transducers were installed in the walls of the tank on test 48. A peak pressure of 67 bars with a duration of 1.2 ms was observed in this fast pour rate experiment. These data and others from the earlier tests in the open geometry series are being used to estimate the size of the chamber. Preliminary analysis indicates that a chamber 1.8 m in diameter with a 19 mm wall will contain the interactions. The analysis is based on thin shell theory and further refinements will be needed.

A purchase order (P.O. 13-3084) has been placed with Ktech Corporation for assistance in the design, procurement, and installation of this apparatus.

2.4.3 Melt Generation

The materials to be used in the experiments include iron, iron oxide, and four component coriums. These will be melted using induction techniques so that melt composition, homogeneity, and temperature can be controlled. The difficulty in performing this task is that the melting temperatures of the materials to be used are high. The coriums melt at above 2000°C and most available technology does not permit this type of melting to be performed easily. The principal tasks in this phase of the work include the following:

- Gain familiarity with induction melting techniques and determine power supply requirements
- Perform analytical melts with simulants to determine melting temperatures and the effects of crucibles on composition
- Design crucibles so that quick-release methods can be used to inject the melt
- Evaluate injection methods which use pressurized crucibles or injection cylinders
- Design, develop, and test the crucible/injection methods
- Install power supply at Bldg 9940 to do the feasibility studies. This includes the design of bus bars to optimize the power delivered to the melt.

A 50 kW power supply, furnace, controller, and recorder have been obtained. This equipment is intended to be used for developmental activities and may be used in the actual tests. Capabilities of this power supply will be determined during the preliminary work. Work requests have been submitted to Plant Engineering for installation of this equipment at the Bldg 9940 site.

One analytical melt of metallic Corium-E has been prepared. The material was inductively melted and is being analyzed by using scanning electron micrographics (SEM) and microprobe techniques to determine homogeneity and composition. It was not clear from the solidified melt if the resultant product is homogeneous or if all the constituents melted. The 100 g specimen was heated at 2000°C for 30 min in a graphite crucible.

2.4.4 Instrumentation

While most measurements to be made are considered routine and will use "off-the-shelf" items in the way of transducers and signal conditioning and recording equipment, certain other measurements of difficult-to-observe quantities may require some new instrument development and/or research into existing methods. The most important of these quantities is the fragmentation rate, because it is linked directly to the thermal energy release rate. Some important parts of this task include

- Fragmentation observation using electromagnetic, optical, or mechanical methods. These methods could include the use of pulsed x-ray sources or acoustic techniques.
- Coolant motion sensors to monitor the coolant surface velocity which will give an estimate of energy released. At the present time specific apparatus needs have not been determined.
- Listing, evaluation, and procurement of sensors and signal conditioning and recording equipment.
- Interface with interaction chamber and site.

Work in this quarter concentrated on fragmentation measurement methods. Commercially available metal detectors and associated circuitry are being evaluated. Electromagnetic metal detection techniques appear to show promise.

2.4.5 Site Preparation

This task involves the preparation and design of site features to properly interface with the anticipated needs of the interaction chamber, melt generator, and instrumentation. Most of this work will be handled by Ktech and Plant Engineering. A work request has been submitted to Plant Engineering for site modification.

2.4.6 Analysis and Modeling

The processes which govern the release of energy from the melt to the coolant are not very well understood. Analysis and modeling coupled with developmental experiments must be done to

aid in designing the experiments and determining the quantities to be measured. While the main effort in this program is to quantify the amount and rate of energy released from a given quantity of reactants, the triggering and propagation phases cannot be overlooked since the rate of energy release is dependent on these processes. In these two areas, the use of hydrodynamic computer codes to study the effects of surface instabilities on melt fragmentation are being investigated. Preliminary work indicates that these codes may be useful in studying these effects on a small scale.

2.4.7 Experiment Design

Previous experimental methods, measurements, and apparatus are being studied. Experimental methods to be used and measurements to be made will place a strong emphasis on observing fragmentation (at least dispersal at the time of energy release), quantifying the amount of reactants, and determining the mechanical work potential.

2.5 Theoretical Analysis of Steam Explosions (M. L. Corradini)

2.5.1 Small-Scale Triggering Experiments

The experimental results of the small-scale steam explosion experiments have been reported by Nelson, et al,¹ and are briefly summarized in Table 2-V. The purpose of this portion of the steam explosion research is to analyze the experimental results in light of existing steam explosion theories and, where these theories are deficient, propose new models or concepts. The analysis is expected to be based initially upon phenomenological modeling of the mechanisms because any rigorous treatment is not considered necessary or even possible at this time.

Effects of the Melt Composition on Steam Explosions -- Steam explosions appear to be eliminated if the initial oxygen content of the prepared powder of Corium-E or iron oxide is low (i. e., no explosion < 50 to 54 at. % oxygen < explosion). One hypothesis advanced to explain these observed results has been a pressure pulse initiated gas release mechanism.

The dissolved oxygen present in oxidic melts, coincident with an external pressure pulse, could fragment the melt. Recent experimental work with the iron-oxide system by Nelson as reported in this quarterly progress report (Section 2.2.1) indicates that the initial amount of dissolved oxygen in the melt is quite small ($\sim 2 \text{ cm}^3$ at STP) and that the melts oxygen content is different than the initial powder composition (O_2 initial - O_2 melt $\approx 1000 \text{ cm}^3$ at STP).

As pressure increases, successful triggering requires longer times between flooding and application of initiating transient. Thus the driving potential for melt fragmentation by gas release is reduced from initial conditions and its capability to fragment the melt must be assessed. Another possibility that must be explored is how the thermophysical properties of the melt change with the oxygen content. These two avenues of investigation are currently being pursued and some preliminary ideas are briefly described below.

TABLE 2-V

Major Experiment Findings

Melt Composition

- Corium-A (U-rich) is very difficult to trigger (1 time in 40 experiments) but occasionally shows spontaneous coarse fragmentation (3 times)
- Corium-E (Fe-rich) triggers easily
- FeO_x closely simulates Corium-E behavior; has extensive literature base
- Explosivity of both Corium-E and FeO_x fall to zero as initial oxygen content of melt decreases

Applied Pressure Transient

- Need only small transient (≈ 1 MPa) to initiate explosion
- Larger magnitude transient (≈ 10 MPa) breaks up melt, but does not trigger inactive melts
- Transient applied through the hearth has never initiated explosions

Subcooling

- Explosions cannot be triggered with 1 MPa pulses at subcoolings of less than:
31 K for Corium-E
24 K for FeO_x

Ambient Pressure

- Corium-E and FeO_x with high initial oxygen contents explode unchanged up to 0.5 MPa; same material could not be triggered at 0.75 or 1 MPa.

To assess the capability of the free oxygen in the melt to fragment it to the observed experimental sizes, two things could be estimated: (1) the work potential of the dissolved gas, and (2) the energy required to overcome the interfacial and frictional forces. If the work potential exceeds these energy requirements, then the possibility of a steam explosion due to a gas release mechanism is a viable hypothesis.

The maximum work potential from the gas would occur if it were assumed that the gas is not dissolved but exists as high-pressure vapor pockets in the melt. This neglects the complex effects of oxygen diffusing toward a growing gas bubble, and assumes all the free oxygen is initially available to fragment fuels. An isentropic gas expansion is also assumed which would maximize the work potential. The energy equation for the isentropic expansion process would be

$$\Delta W = m_g C_{v_g} (T_i - T_f) \quad (1)$$

where

m_g = mass of free oxygen gas

C_{v_g} = specific heat of gas

T_i and T_f = initial and final temperature.

Rearranging,

$$\Delta W = m_g C_{v_g} T_i \left[1 - \left(\frac{T_f}{T_i} \right) \right] \quad (2)$$

Now for a perfect gas isentropic expansion the ratio of initial and final temperatures are related to the volume, V , by the expression

$$\frac{T_f}{T_i} = \left(\frac{V_i}{V_f} \right)^{\gamma-1} \quad (3)$$

This can be substituted into Eq (2) to give

$$\Delta W = m_g C_{v_g} T_i \left(1 - \left(\frac{V_i}{V_f} \right)^{\gamma-1} \right) \quad (4)$$

If the mass of oxygen available to do work is taken to be the average value from Nelson's calculations in Section 2.2.1 (3 cm^3 at STP or $\approx 3.8 \text{ mg}$) the maximum work is calculated to be 5 J.

The energy required to fragment the drop (E_{frag}) is used to create new surface area and overcome friction as the melt is accelerated and fragmented. Cho and Fauske⁷ estimate this energy to be

$$E_{\text{Frag}} = \frac{6V_{\text{drop}} \sigma}{D_f} + 1.81 C_d \rho V_{\text{drop}} \left(\frac{V_{\text{drop}}^{2/3}}{t_{\text{mix}}^2} \right) \left(1 - \frac{D_f^2}{4V_{\text{drop}}^{2/3}} \right) \ln \left(\frac{2V_{\text{drop}}^{1/3}}{D_f} \right) \quad (5)$$

where

- V_{drop} = initial volume of the melt ($\sim 3 \text{ cm}^3$)
 D_f = final diameter of the melt fragments ($\sim 100 \text{ }\mu\text{m}$)
 t_{mix} = mixing and fragmentation time ($\sim 1 \text{ ms}$)
 C_d = drag coefficient (~ 1)
 σ = surface tension ($\sim 700 \text{ dyn/cm}$)
 ρ = density.

The approximate values for the Fe_2O_3 -water system are given in parentheses. The major unknown value is the representative density in which the fragmentation takes place. It could vary from a two-phase water density ($\sim 0.5 \text{ g/cm}^3$) to the molten oxide density ($\sim 5 \text{ g/cm}^3$). For a minimum value of $\rho = 1 \text{ g/cm}^3$, the minimum energy required is about 4J. Thus the viability of impulse-initiated gas release as a mechanism for fragmentation is not clearly demonstrated. Further work on the mechanisms for impulse-initiated gas release and melt fragmentation are now underway.

The second area of investigation is to assess the effects of the oxygen content on the thermo-physical properties of the melt. This task is difficult with Corium-E as the melt is quite complex because of the many alloy components. Thus the iron oxide melt is being investigated first to see if any trends are discernible. Theoretical or experimental properties (k , ρ , C_p , σ) for molten iron oxide are not well known. At the present time, values for the density, specific heat, surface tension, and viscosity of liquid iron oxides have been for a limited range of temperatures and composition. A literature survey is underway and to date the thermal conductivity has not been quantitatively identified as a function of oxygen content. Elliott has measured the thermal conductivity of molten iron oxide (FeO) with silica present.^{8,9} The trend of the data thus far accumulated indicates that the interface temperature between water and iron oxides rapidly decreases as the oxygen content increases. To illustrate this, the interface temperatures (T_I) can be computed for iron and water and Fe_3O_4 and water and compared assuming constant properties. The expression for T_I is

$$T_I = \frac{T_{\text{hot}}}{1 + \beta} + \frac{\beta T_{\text{cold}}}{1 + \beta}$$

where

$$\beta = \sqrt{\frac{K\rho C_p \text{ cold}}{k\rho C_p \text{ hot}}}$$

$$T_I = 1950 \text{ K for iron-water}$$

$$T_I < 1650 \text{ K for Fe}_3\text{O}_4\text{-water}$$

where

$$T_{\text{hot}} = 2000 \text{ K}$$
$$T_{\text{cold}} = 300 \text{ K}$$

This is because of the decreasing thermal conductivity of the hot material. This would suggest a less stable film boiling regime and, if a thermal-physical explanation for steam explosion based on coolant vaporization is advanced, this would indicate a greater potential for film destabilization and subsequent explosions for more oxidic melts.

The effect of Different Triggers on the Steam Explosion -- Nelson has indicated that the exploding bridgewire trigger (~0.8 MPa) has produced reproducible explosions under varying conditions.¹⁰ In addition minidetectors were used to produce larger pressure pulses (~10 MPa) when melt compositional effects were investigated. The results indicated that both triggers could produce explosions when oxygen content was high (~62%) and no explosion when it was low (~52%). However, when a detonator-driven projectile was used to impact the melt's rigid hearth from below and produce a pressure pulse in the melt, no explosion occurred regardless of the oxygen content. The pressure-pulse-initiated gas release hypothesis would predict that all three methods of pressure pulse application should produce an explosion. This discrepancy between the theory and experiment may be due to the method of application of the pressure pulse from below. The projectile produced a high-pressure planar pulse (~1 MPa) into the melt. The duration of the pulse may have been too long, causing the melt to see a positive pulse without the expected negative reflected pulse which would be characteristic of the other pressure trigger applications. It is that negative pulse which is viewed as the trigger needed to allow gas release in the melt to fragment it. Thus the mode of pressure application may not have satisfied a requirement of the gas release hypothesis. If future funding allows, experiments will be performed with a thin steel projectile which will give a large but short-duration pressure pulse. If this is successful, experiments can be carried out with and without water present as a definitive test of the gas release hypothesis. If this hypothesis is valid, the presence of water should not affect the melt fragmentation behavior and the gas release mechanism.

Water Subcooling and Ambient Pressure Effects on Steam Explosions -- When the water temperature was raised (subcooling lowered) to 70°C, the steam explosion's second stage pressure pulse was inhibited for the Corium-E and iron oxide melts. As the temperature was raised higher, the first stage of interaction could also be suppressed. In all tests, only exploding bridgewires were used. Nelson has suggested that the film boiling regime is more stable at higher water temperatures.¹⁰ The higher water temperatures do not allow as much energy to be conducted away from the coolant vapor-liquid interface. As a result, more energy goes into coolant vaporization and the vapor film becomes larger and more stable. Therefore, a pressure pulse would be less effective at high water temperatures in collapsing the film and triggering the interaction.

When the ambient pressure was raised from 0.1 MPa to 0.5 to 0.75 MPa (~5 to 7.5 atm), the two-stage steam explosion was suppressed for bridgewire pressure pulses (~1 MPa at 2 cm) for both Corium-E and iron oxide. Nelson used minidetectors at the same high ambient pressures and reported that no explosions occurred.¹⁰ However, for this set of experiments the pressure pulses generated by the minidetectors were significantly below their normal output (ΔP at 2 cm ~ 5 MPa). These misfires were caused by water leakage into the explosive canister reducing the explosive pressure pulse to about double that from a bridgewire pulse. This high-pressure cutoff might be caused by two phenomena: (1) the trigger pulse cannot collapse the vapor film at high ambient pressures and therefore the interaction is not triggered; (2) the ambient pressure affects the propagation of the explosion due to vapor bubble growth considerations;^{11, 12} thus the interaction is nonexplosive. Both explanations are being considered with special emphasis on the former. The reason for this is that significant progress has been made by Henry^{11, 12} in the second area and very little previous work has been done on pressure-driven film destabilization. In addition, there may be a commonality between the water subcooling cutoff and the high-pressure cutoff, based on the film destabilization behavior during the triggering phase.

The investigation of vapor film destabilization by pressure pulses has centered around the film boiling behavior of a hot molten sphere in water. This initial geometry is spherically symmetric and is amenable to simple phenomenological modeling of the film collapse process. The dynamic film boiling process is modeled by considering the molten drop, vapor film, and surrounding coolant as lumped parameter volumes and writing an energy equation for each region coupled by temperatures and heat fluxes. The behavior of the film collapse due to an applied pressure pulse is then observed for a number of different initial water temperatures and ambient pressures. The transient pressure pulse is assumed to be applied symmetrically around the molten drop. Preliminary results of this theoretical investigation indicate that the film does not collapse as readily when the water temperature or the ambient pressure is high. Future work will investigate initial conditions similar to those in the small-scale tests by Nelson.¹⁰ Although the results from these studies are not directly applicable to Nelson's tests, they should indicate the effect of different initial conditions on film collapse, thereby helping to determine if the temperature and pressure cutoffs are based in the trigger phase of the explosion.

2.5.2 Large-Scale Propagation Experiments

At the present time, two separate programs are underway to investigate the effects of various parameters on the propagation and efficiency of steam explosions at intermediate scales (melt mass ~ 10 to 25 kg). The open geometry test series has conducted 48 experiments of various parameter variations. The fully instrumented test series (FITS) was begun recently, and its purpose is to provide more detailed results of the explosion's propagation and efficiency. Because the open geometry test results are mainly qualitative and no tests have been completed in the FITS series, the phenomenological modeling effort in this area has been directed toward identifying the possible fragmentation and heat transfer mechanisms involved during the propagation phase of the explosion. Simple phenomenological models will be constructed to be included in larger calculational models to analyze the future experimental results. Some of the possible mechanisms are briefly described.

Melt fragmentation is physically caused by acceleration or relative velocity differences between the fuel and the coolant. These differences cause the melt's fragmentation by Taylor or Helmholtz instabilities. The cause of such acceleration and/or relative velocities can be the result of a number of physical events: (1) possible passage of a shock wave through a melt-coolant mixture where the initial relative velocity causes acceleration perpendicular to the flow; (2) pressure pulse on the surface of the melt (e.g., due to nearby explosion or vapor film collapse) which cavitates the melt interior and the melt fragments because of the acceleration outward of dissolved gases; (3) rapid coolant vapor formation, at the interface of the melt and coolant, causing a local high-pressure zone which accelerates the melt and can fragment it. Although the resulting fragmentation behavior is similar, each initiating mechanism is different and thus probably will have different characteristic times and length scales which describe the phenomena. Each should be considered to determine which may govern the overall process.

The heat transfer mechanisms possible during the propagation may be quite complex but initially could be classified by two physical models: (1) the melt and the liquid coolant come into liquid-liquid contact because of an external or random pressure pulse momentarily collapsing the film boiling regime, and (2) the film boiling regime may not totally collapse and quite efficient heat transfer may occur across a thin vapor film. In the first case, because the melt temperature is so high (2000 K), this liquid-liquid contact cannot be maintained and a critical fluid is locally formed at high temperature and pressure. This event will fragment the melt and drive more melt-water interfaces to contact and the explosion continues. The second explanation may apply when the initial trigger is too small to collapse the film but simply decreases its size and thereby significantly raises the heat transfer rate.

2.6 Assessment of Containment Failure Capability (M. L. Corradini)

The major reason why steam explosions are of interest in hypothetical core melt accidents is that they can provide a separate mechanistic path for radiological transport into the containment and possible containment failure. Therefore, the final portion of this research work is to couple the experimentally observed and expected steam explosion efficiencies with an analysis of the containment failure capability. The proposed approach to this portion of the work is composed of four tasks:

1. Assume a conservative upper bound on the coherent release of energy from a steam explosion and evaluate the ways the reactor vessel may fail, and possibly generate a missile.
2. Perform order-of-magnitude analyses to assess the various ways the energy may be dissipated during the coolant slug acceleration phase, before reactor head impact, and during the missile flight toward the containment.

3. Use simple models to predict if containment failure occurs by

- static overpressure
- dynamic pressure shock
- missile generation and penetration.

(If the result is containment failure, iterate with less conservative assumption and/or consider No. 4.)

4. Use structural codes to assess possible containment failure due to pressures or missiles generated by steam explosion.

The status of each task will be reviewed briefly.

2.6.1 Possible Release of Energy and Reactor Vessel Failure Due to Steam Explosions

The open geometry tests as reported by Buxton and Benedict in this quarterly report (Section 2.3) indicate that the steam explosions at an intermediate scale have a thermal energy to mechanical work conversion ratio of around 1%. At the present time, there is no way of extrapolating these results to the hypothetical full-scale reactor accident because no scaling experiments at larger scales have been undertaken nor phenomenological models developed to indicate the effect of scale. However, if the intermediate and full-scale conversion ratios are assumed to be about the same, then the energy released could be quite large. This energy release will most probably be in the form of local shock waves and acceleration of the water column in the lower plenum as a slug, impacting the reactor vessel head. This impact could simply breach the reactor vessel, allowing a release of some of the core inventory, or could also generate a missile by failure of a part or the whole head. WASH-1400 considered that a steam explosion would fail the whole reactor vessel head below the head flange by a brittle failure mechanism. This was considered a conservative failure mechanism in that no credit was given to plastic deformation. Henry has suggested that a steam explosion with a conversion ratio as high as 3% could not fail the reactor vessel if the failure occurs at the head bolts by a purely ductile failure.¹³ This should be recognized as a highly optimistic analysis. These two simple analyses could be looked upon as the bounds to the problem of coupling the impulse of water slug impact to the breaching of the reactor vessel and/or generation of missiles. More mechanistic analysis is being planned to narrow the bounds on this issue to a more realistic spectrum of alternatives.

The potential for containment damage if a steam explosion occurs in the reactor cavity will also be evaluated. The conclusion of WASH-1400 was that this scenario for a steam explosion would not lead to containment failure.

2.6.2 Dissipation of the Energy From the Steam Explosion

The two areas where energy dissipation can occur are (1) incoherencies in the formation and acceleration of the water slug up to reactor head impact, and (2) the obstructions that can dissipate a missile's energy, once formed, as it approaches the containment. In the first case, the two major energy dissipation mechanisms will be the heat transfer from the hot, high-pressure

water vapor to the water slug and to the solid steel structures remaining in the vessel. Based upon past work by Theofanous¹⁴ and Corradini,¹⁵ this heat transfer could reduce the slug's energy by more than a factor of 2. It should be emphasized, though, that the amount of energy dissipation is dependent upon the accident scenario, because this preimpact expansion phase is affected by internal reactor vessel geometry.

The second phase of energy dissipation would occur when a missile is thrown toward the containment. The missile may impact obstructing objects before it reaches the containment wall. Some examples of possible obstructions are the control rod drive assemblies, the above-vessel missile shield, the fuel transfer crane, and the polar crane. The possible energy losses to each should be estimated.

2.6.3 Simple Models to Assess Capability of Containment Failure by a Missile

The ability of a missile to penetrate a concrete containment has been estimated with simple empirical models for containment penetration developed from experiments at Sandia and by others.¹⁶ The applicability of these models to the issue at hand is approximate. The empirical models developed by Sandia through earth penetration tests are based on data from penetration targets which are essentially infinite in depth in comparison to the missile size. In contrast, the French experiments employed concrete missiles being propelled against reinforced concrete walls of finite depth. However, the results from application of all of these models generally indicate a common conclusion: the fraction of energy dissipated in penetrating a containment structure similar to that in current LWRs is small when compared to the total energy of the missile (e.g., 5% to 20% of the total energy). This result is based upon neglecting the dissipation mechanisms in the vessel and containment and directly coupling the missile's energy to the energy from a steam explosion with a 1% conversion ratio. The missile size was either the reactor vessel head size or a part of a control rod drive assembly, assuming both to be hard missiles.

Besides examining the effect of missile impact on the containment, the effects of dynamic pressure pulses will also be examined. In addition, the overall question of what type of containment failure occurs should not be overlooked. The analysis of WASH-1400 assumed a failure location at the top of the containment with a large hole ($\sim 20 \text{ ft}^2$) created. The temperature of the release (hot or cold) was assumed to be dependent upon the previous containment condition before the steam explosion. Reevaluation of these assumed conditions is planned.

References for Section 2

1. M. Berman, Ed., Light Water Reactor Safety Research Program Quarterly Report July - September 1978, SAND79-0359, Light Water Reactor Safety Department, Sandia Laboratories, Albuquerque, NM, April 1979.
2. M. Berman, Ed., Light Water Reactor Safety Research Program Quarterly Report April - June 1978, SAND78-1901, Nuclear Fuel Cycle Safety Research Department, Sandia Laboratories, Albuquerque, NM, January 1979.
3. M. Berman, Ed., Light Water Reactor Safety Research Program Quarterly Report January - March 1978, SAND78-1411, Nuclear Fuel Cycle Safety Research Department, Sandia Laboratories, Albuquerque, NM, October 1978.
4. M. Peehs, "Investigations of Molten Corium Phases," Thermodynamics of Nuclear Materials 1974, International Atomic Energy Agency, Vienna, Austria, IAEA-SM-190/10, 1975.
5. L. S. Nelson and L. D. Buxton, Steam Explosion Triggering Phenomena: Stainless Steel and Corium-E Simulants Studied With a Floodable Arc Melting Apparatus, SAND77-0998, Sandia Laboratories, Albuquerque, NM, May 1978.
6. D. A. Dahlgren, Ed., Light Water Reactor Safety Research Program Quarterly Report October - December 1978, SAND78-0600, Nuclear Fuel Cycle Safety Research Department, Sandia Laboratories, NM, June 1978.
7. D. H. Cho, et al, "Some Aspects of Mixing in Large-Mass, Energetic Fuel-Coolant Interactions," ANS-ENS Fast Reactor Safety Meeting, CONF-76001, October 1976.
8. J. F. Elliott, et al, "Measurement of the Thermal Diffusivity of Liquid Oxides and Metallurgical Slags," Metal Transactions B, vol. 7B, June 1976.
9. J. F. Elliott, "Experimental Problems in Measuring the Thermal Conductivity of Liquid Oxide," Canadian Metallurgical Quarterly, vol. 14, No. 3, 1975.
10. L. S. Nelson, L. D. Buxton, and W. B. Benedick, Steam Explosion Triggering Phenomena. Part II: Corium-A and Corium-E Simulants and Oxides of Iron and Cobalt Studied with a Floodable Arc Melting Apparatus, Sandia Laboratories, Albuquerque, NM, to be published.
11. R. E. Henry and K. Miyasaki, "Effects of System Pressure on Bubble Growth from Highly Superheated Water Droplets," ASME Winter American Meeting, December 1976.
12. R. E. Henry, "Vapor Explosion of Freon 22 with an External Trigger," Light Water Safety Information meeting, November 7, 1978.
13. R. E. Henry, Fuel Meltdown Program Review and Information Exchange Meeting, December 5, 1978.
14. T. G. Theofanous and H. K. Fauske, An Energy Dissipation Mechanism Due to the Cladding of the Fission-Gas Plenum During an HCDA, ANL/RAS 72-31, September 1972.
15. M. Corradini, N. E. Todreas, W. M. Robsenow, and A. A. Sonin, Heat Transfer and Fluid Flow Aspects of Fuel-Coolant Interactions, MIT Report, COO-2781-15TR, September 1978.
16. C. Berriand, "Local Behavior of Reinforced Concrete Walls Under Hard Missile Impact-- Translation," SAND77-6021, 4th SMIRT Conference August 1977, November 1977.

3. Statistical Analysis (T. J. Bartel, M. Berman,
R. K. Byers, G. P. Steck)

3.1 Summary

This program is directed toward the development and application of statistical methods for predicting the probable distribution of peak clad temperature (PCT) during a loss-of-coolant accident. Values of PCT calculated with RELAP4/MOD6, with various data sets, are used to produce a response surface prediction. This approach has been chosen to limit the number of long, expensive computer runs.

Effort in this study has centered on the analysis of results for the blowdown portion of a LOCA, and on investigations of methods to be used in analyzing the reflood phase. Some of the model assumptions used in the calculations were changed, and the results of these variations were examined. Results of the quarter's work follow.

Studies were made of the effects, during blowdown, of the choice of gap conductance models (MacDonald-Broughton or Ross-Stoute), of metal-water oxidation reaction parameters (Cathcart-Pawel or Baker-Just), of fuel state (fresh or once-burned), and of decay heat modeling (old ANS standard or revised). The results of combining some of these options were also examined. Based on these analyses, decisions were made on which models to use in performing another series (BD5) of statistical blowdown runs. Results of these runs were used to develop a PCT response surface and rank statistical input variables in order of importance.

In preparation for carrying out the response surface analysis for the reflood portion of a LOCA, several questions concerning the proper initialization of reflood problems were addressed. These included using results at the end of blowdown to define fuel rod temperature distributions and system conditions at the start of the reflood calculations. A method of extending the decay heat description from the end of blowdown was also considered, and compared well with RELAP calculations. Results of these studies, as well as other considerations, led to the augmentation of the list of statistical variables to be used for reflood calculations. It is still unclear how best to implement these "dials," as well as those associated with the blowdown phase, for RELAP reflood runs. However, the anticipated use of TRAC (which should be capable of a continuous LOCA calculation from break through reflood) may eliminate these problems.

The steady-state fuel code, FRAPCON-1, was received from Idaho National Engineering Laboratory and run successfully on a test problem. The code will allow us to verify initial fuel states for the statistical study.

3.2 Statistical Blowdown Calculations

During the quarter, approximately 95 blowdown calculations were performed using RELAP4/MOD6 and the nodalization shown in Figure 3-1. A small number (~10) of these calculations were made to investigate the effects of various changes in some of the models used in the study (see Sections 3.2.1 and 3.2.2). The remainder comprise a part of the series we have termed BD5, for use in developing the PCT response surface from the RELAP output. The BD5 series differs from the BD4 series previously reported¹ in employing two input sampling techniques (Latin hypercube and fractional factorial), and in the use of a different model for the fuel-clad gap conductance (see Section 3.2.1). The first 26 of these calculations repeated the BD4 series, using the McKay-Conover input selection technique; input (or "dial") sets 26 through 41 were chosen with that technique modified to introduce a bias toward higher temperature results. Fractional factorial input sampling was used for runs 42 through 83. Finally, three calculations were performed as the beginning of a sensitivity study, in which subsets of the statistical input variables were changed and the effects noted. Results of the BD5 series of calculations are discussed in Section 3.5.

3.2.1 Gap Conductance Models

An investigation was performed on the gap conductance models used by RELAP4/MOD6. Two models are available: the modified Ross-Stoute (R-S) and the MacDonald-Broughton (M-B). The important model assumptions are given in Table 3-I.

TABLE 3-I
Gap Conductance Model Assumptions

<u>Modified Ross-Stoute</u>	<u>MacDonald-Broughton</u>
BE in MOD 6 (EM in MOD5)	BE in MOD6 only
No burnup dependence, i.e., fresh fuel	Functional dependence on burnup (set to fresh fuel in MOD6)
Axisymmetric fuel-clad expansion	Relocation model--movement of a portion of the fuel to contact the clad (~30% of fuel assumed to be in contact with clad at 0% burnup)
INEL recommends pressurized fuel rod	INEL recommends unpressurized fuel rod

It was found that the M-B model with a multiplier of 6.0 on the final gap conductance was used in the BD4 series and earlier statistical calculations. The multiplier was provided by Idaho National Engineering Laboratory (INEL) in an attempt to match the fuel stored energy

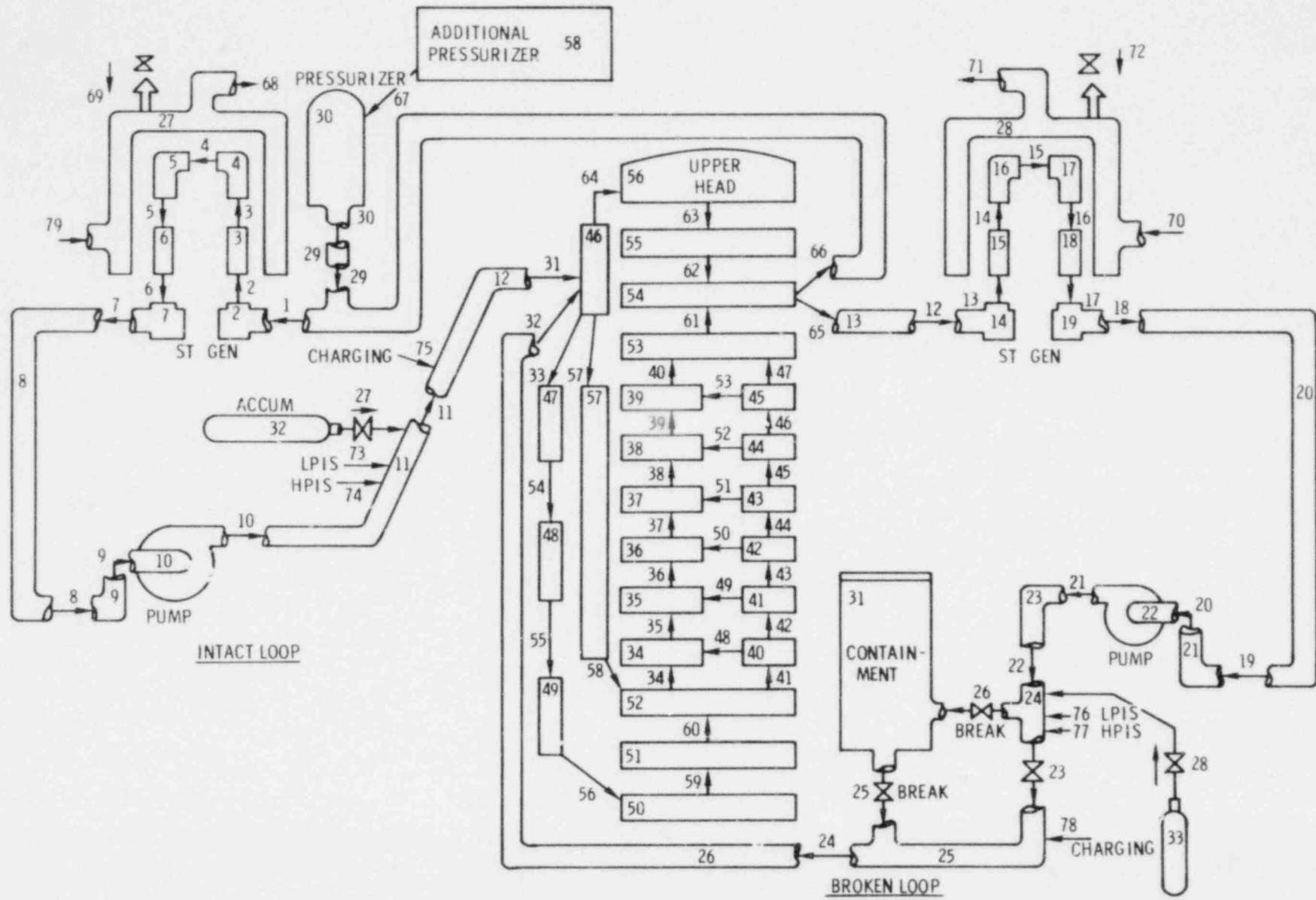


Figure 3-1. Nodalization for RELAP Statistical Blowdown Study

from a FRAP-S calculation. It is uncertain which conductance model was used by FRAP-S; however, it appears that the R-S model was used. It was also determined that the M-B model had an error in the radiation heat transfer term. Tests showed that this error had an insignificant effect on the fuel temperatures.

Table 3-II is a comparison of the two original fuel conductance models and the M-B x 6 model for the base case statistical blowdown calculation. The effect of the multiplier is clearly illustrated by the very small temperature drop across the gap. The R-S model predicted the highest PCT while the M-B x 6 the lowest. An additional effect of the multiplied M-B version was to reduce the ranking of the gap size as a statistically important variable. Table 3-III illustrates the effect that changing gap width has on the temperature drop across the gap and PCT for M-B x 6 and R-S. One can see the large changes in these parameters for the R-S model while the M-B x 6 model shows little change. This phenomenon is due to the relative weighting of the gap thickness in the conductance models. The nature of the M-B model, given a relocation amount, reduces the effect of the gap thickness; however, the use of the 6.0 multiplier dominates the calculation and effectively eliminates the gap width as a parameter. But, since the R-S model is a classical axisymmetric model, the gap thickness has a direct effect on ΔT_{gap} . Because RELAP uses volume temperatures as boundary conditions for initial temperature distributions in adjacent heat slabs, we would expect that initial fuel temperatures, hence stored energy, would be lower for the M-B case. We also expect the higher gap conductance to permit more efficient heat removal from the slabs. That these expectations are correct may be seen in Figure 3-2, showing fuel stored energy histories for the two calculations. Figures 3-3 and 3-4, comparing temperatures in two of the hot pin heat slabs, also show the effect. Quantities associated primarily with hydrodynamic response differed insignificantly between the two calculations. This is illustrated in Figures 3-5, 3-6, and 3-7, showing flows to the upper head, break flows, and flows to the upper annulus, respectively. Similar results were noted for input conditions other than nominal, although the magnitude of the effects varied greatly. Figures 3-8 and 3-9, showing slab temperature histories for two members of the statistical sampling set, demonstrate this point. We also note that temperature response after the time at which PCT occurs can be of quite a different character.

As a result of these comparisons, and because of the use of pressurized fuel, the BD5 series and subsequent calculations will be performed with the Ross-Stoute gap conductance model. The implementation of a relocation model into the basic R-S calculation may be considered at a later date.

TABLE 3-II

Comparison of Fuel Gap Conductance Models

Initial Conditions	Model ^{a, b}		
	1	2 ^c	3 ^c
T_{surface}	-	same	same
ΔT_{gap}	10-15°	150-170°	70-90°
T_{CL}	-	230-250° higher	80-100° higher
PCT Conditions (~6.5 s)			
PCT	-	100° higher	40° higher
ΔT_{gap}	2-5°	20-40°	10-25°
T_{CL}	-	180-200° higher	100-110° higher
Fuel Energy	-	3% higher	1% higher

^a Models: 1 - MacDonald-Broughton MOD6-Sandia
 2 - Modified Ross-Stoute MOD6
 3 - #1 without the 6.0 multiplier

^b All temperatures in °F
^c Compare with Column 1

TABLE 3-III

Sensitivity of Gap Widths in Fuel Gap Models
(all values in °F)

Model ^a	Base Case		Dial Set 1 DL Gap = -1.104		Dial Set 17 DL Gap = 1.299	
	1	2	1	2	1	2
Initial Condition ^b						
T_{surface}	618	618	617	617	611	611
T_{CL}	2195	2410	2710	2758	1844	2502
ΔT_{fuel}	1478	1578	2001	2027	1134	1392
ΔT_{gap}	13	128	8	30	24	425
PCT Conditions ^b						
	6.5 s		~4.5 s		~6s	
T_{surface}	1084	1177	1065	1072	1020	1318
T_{CL}	1241	1407	1744	1790	1104	1720
ΔT_{fuel}	149	193	658	674	79	331
ΔT_{gap}	4	31	10	36	2	66

^a Models: 1 - M-B Sandia BD4 Series
 2 - R-S BD5 Series

^b At Slab 15 (hot rod)

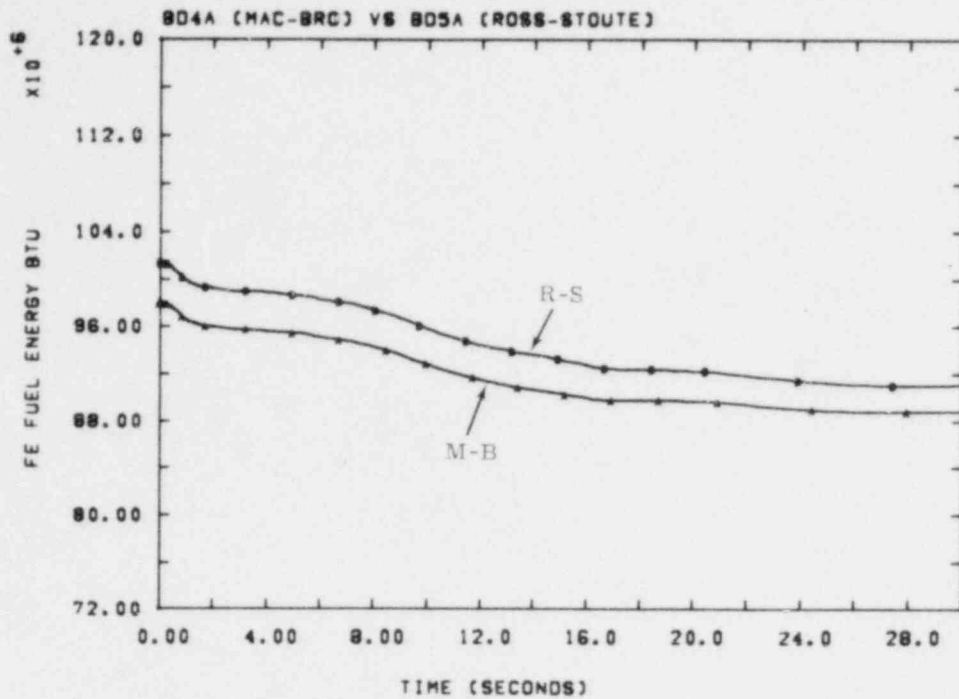


Figure 3-2. Fuel Stored Energy Histories, MacDonald-Broughton vs Ross-Stoute

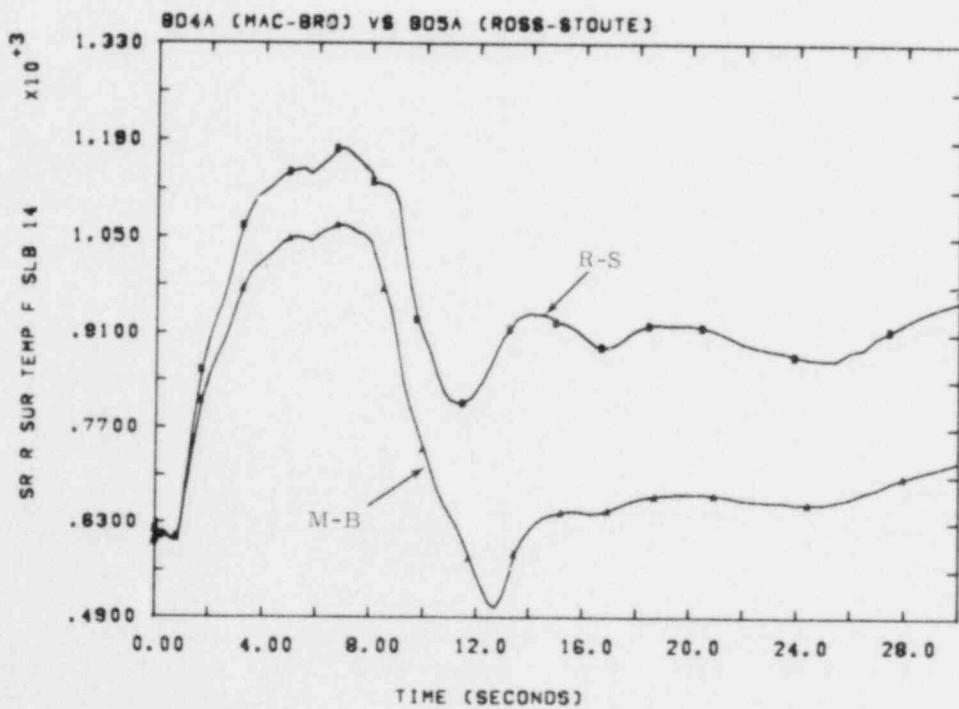


Figure 3-3. Slab 14 Temperatures, MacDonald-Broughton vs Ross-Stoute

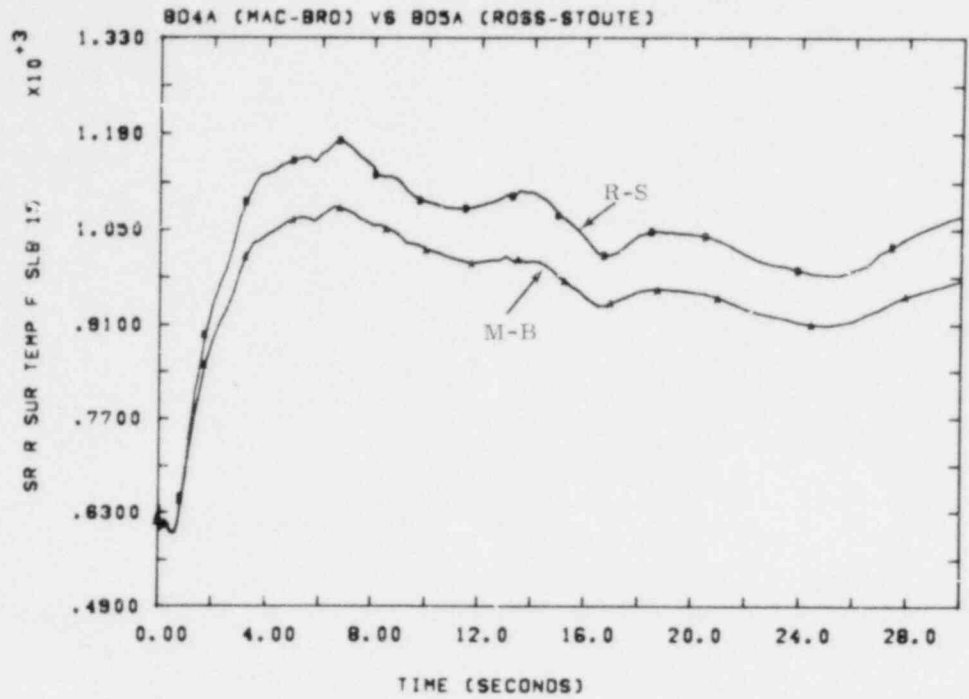


Figure 3-4. Slab 15 Temperatures, MacDonald-Broughton vs Ross-Stoute

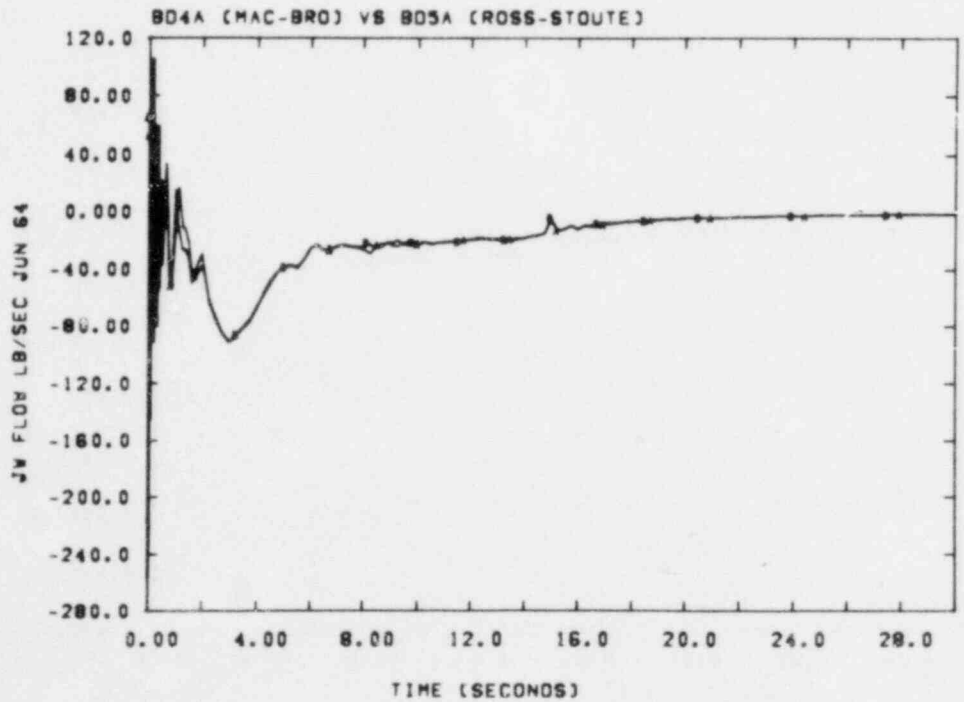


Figure 3-5. Flows to Upper Head, MacDonald-Broughton and Ross-Stoute

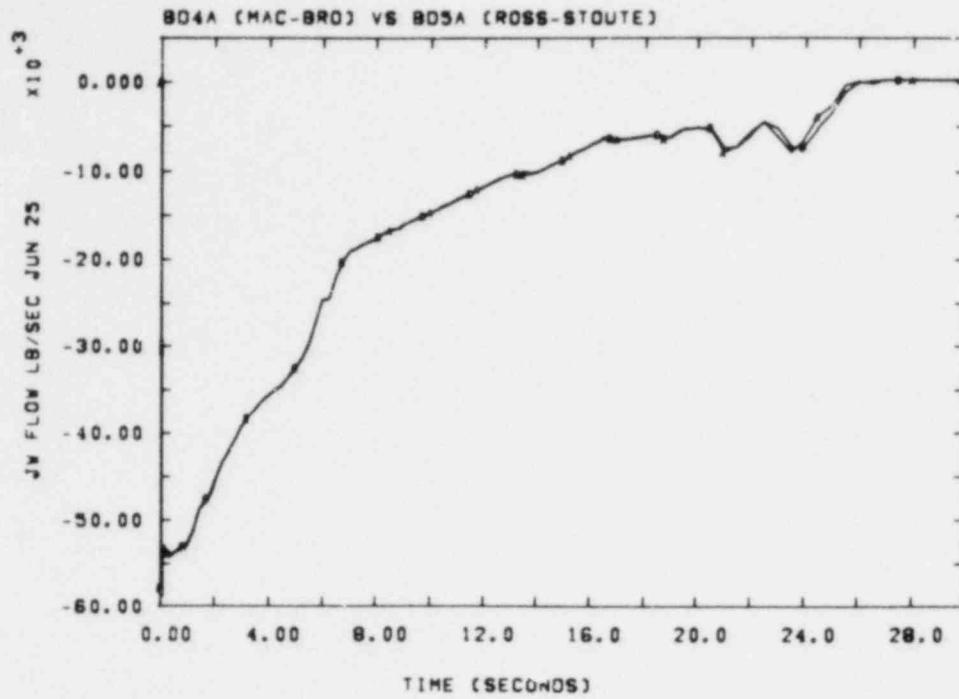


Figure 3-6. Break Flows, MacDonald-Broughton and Ross-Stoute

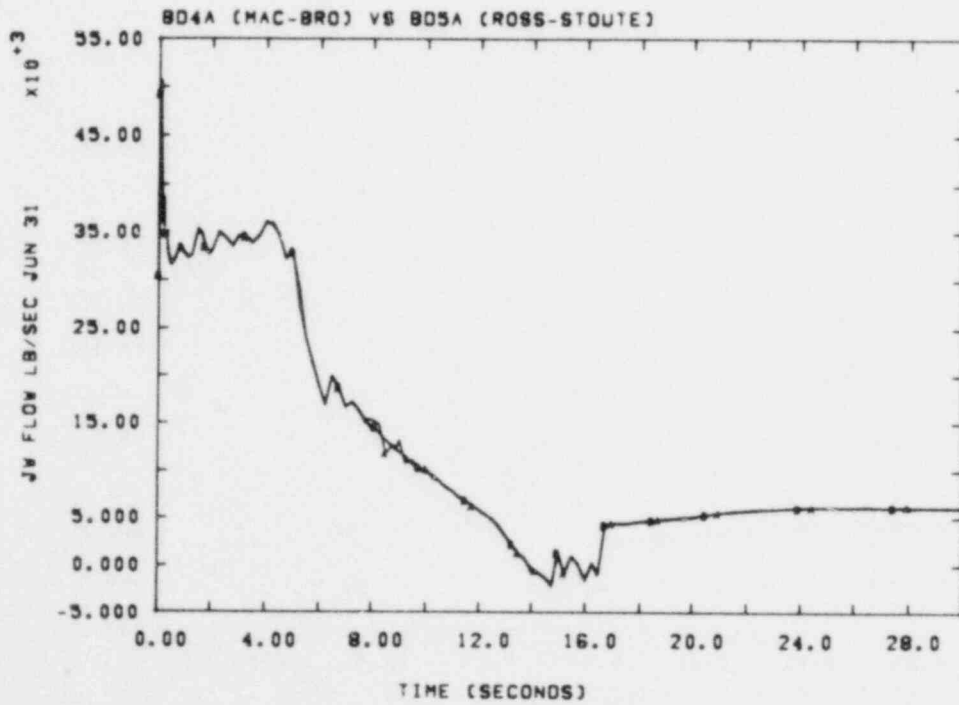


Figure 3-7. Flows to Upper Annulus, MacDonald-Broughton and Ross-Stoute

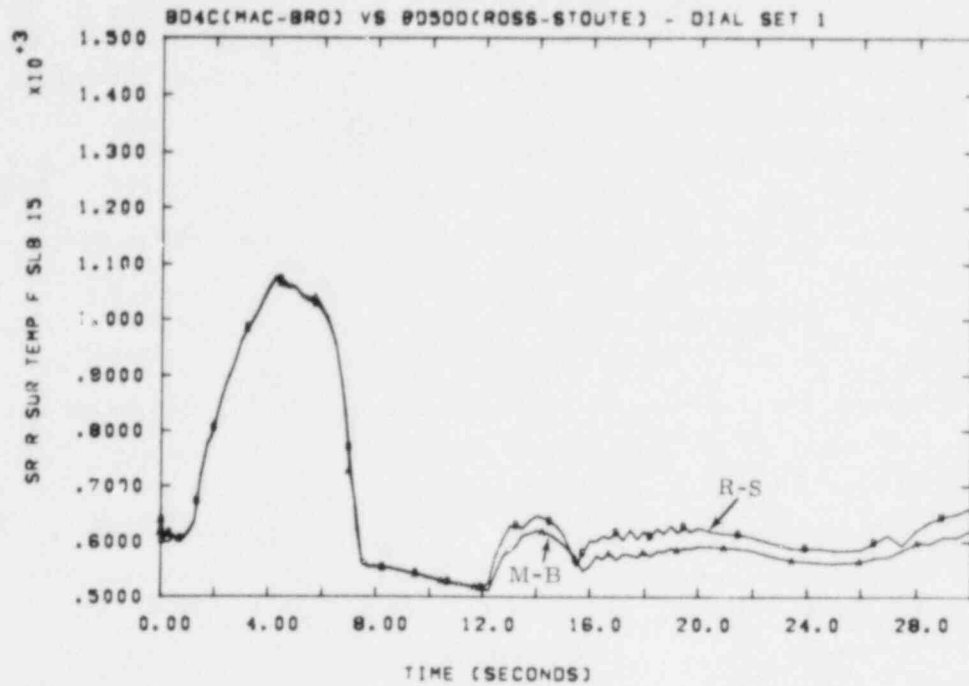


Figure 3-8. Slab 15 Temperature, MacDonald-Broughton vs Ross-Stoute, Dial Set 1

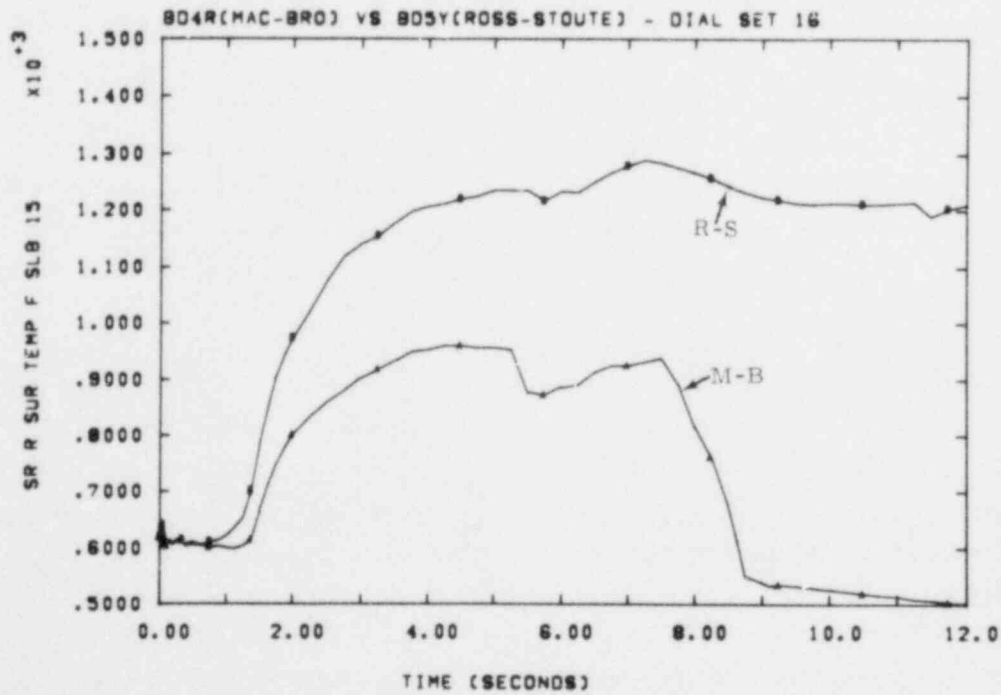


Figure 3-9. Slab 15 Temperatures, MacDonald-Broughton vs Ross-Stoute, Dial Set 16

3.2.2 Combined Effects of Some Modeling Options

To increase our understanding of the effects of some of the options available in RELAP4/MOD6, we have performed a number of calculations holding most of the input variables at values which are nominal for the statistical study. The additional calculations, together with the five mentioned in the previous section, form a set of nine on which some comparisons can be based.

In addition to the choice of gap conductance model, described in Section 3.2.1, one of the options was the choice of metal-water reaction parameters: Cathcart-Pawel (C-P) or Baker-Just (B-J). Other variations in this set of runs were fuel state (fresh or once-burned), time into the fuel cycle (TIC), and the choice between revised, old, or 1.2 times old ANS decay heat rates. Table 3-IV is a description of the various options used in these calculations. The table also displays initial and final fuel stored energy (FE) and PCTs for two of the hot pin slabs (15 and 16). Notice that all time-in-life values used were 226 months, with one exception; BDMUL1C used 230.9 months. Therefore the fuel was treated as being in the equilibrium cycle for all gap width, peaking factor, and decay heat calculations.

TABLE 3-IV
Model Comparison Runs

Run (BD-)	Gap Conductance	M-W Reaction	Fuel State	TIC (mo)	Decay Heat	FE (MBtu, approx)		PCT (°F, approx)	
						Initial	Final	Slab 15	Slab 16
4A	M-B x 6	C-P	Fresh	6	New	95.0	88.8	1087	1084
4B	M-B x 6	C-P	Once burned	6	New	98.1	88.9	1085	1081
4AN6F	M-B	C-P	Fresh	6	New	99.2	89.7	1126	1118
5A	R-S	C-P	Fresh	6	New	101.3	91.1	1183	1179
5B	R-S	C-P	Once burned	6	New	98.4	89.2	1102	1099
MUL1A	R-S	C-P	Fresh	6	Old	101.3	91.2	1182	1183
MUL1B	R-S	B-J	Fresh	6	Old	101.3	91.2	1183	1182
MUL1C	R-S	B-J	Once burned	10.9	Old	98.4	89.3	1060	1073
MUL1D	R-S	B-J	Fresh	6	Old x 1.2	101.3	92.1	1198	1195

As seen in Table 3-IV, no surprising or inconsistent effects on PCT were observed in these comparisons. As noted previously, the R-S gap conductance model results in a much larger effect of initial gap width on fuel stored energy. This, in turn, permits the choice of fuel state to influence results to a larger degree. Figures 3-10 and 3-11, showing fuel stored energy and a typical temperature history, respectively, demonstrate the comparison between results for fresh and once-burned fuel.

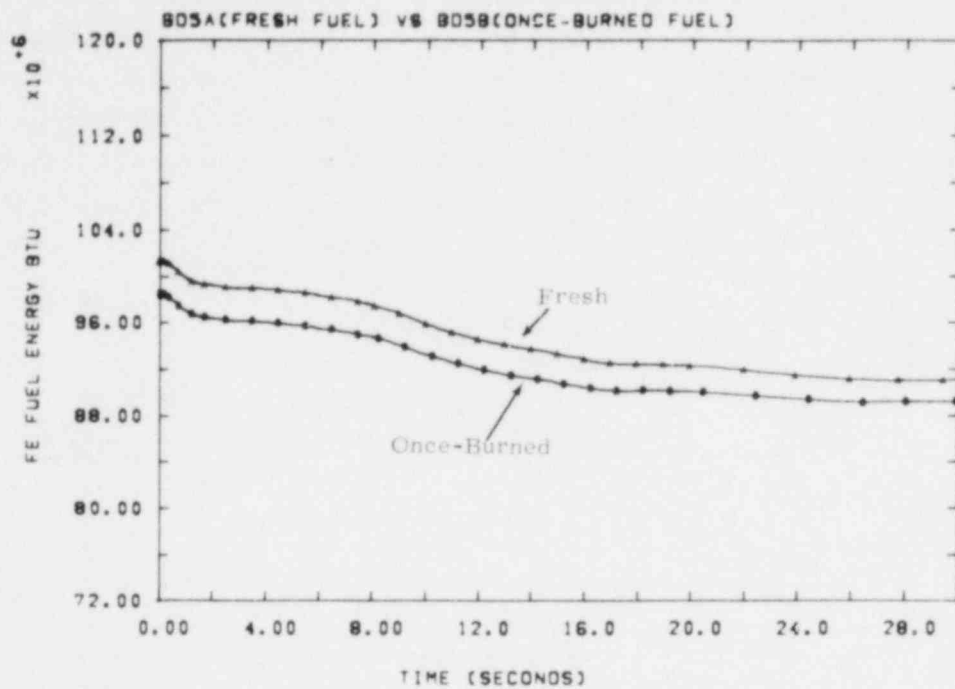


Figure 3-10. Fuel Stored Energy, Fresh and Once-Burned Fuel

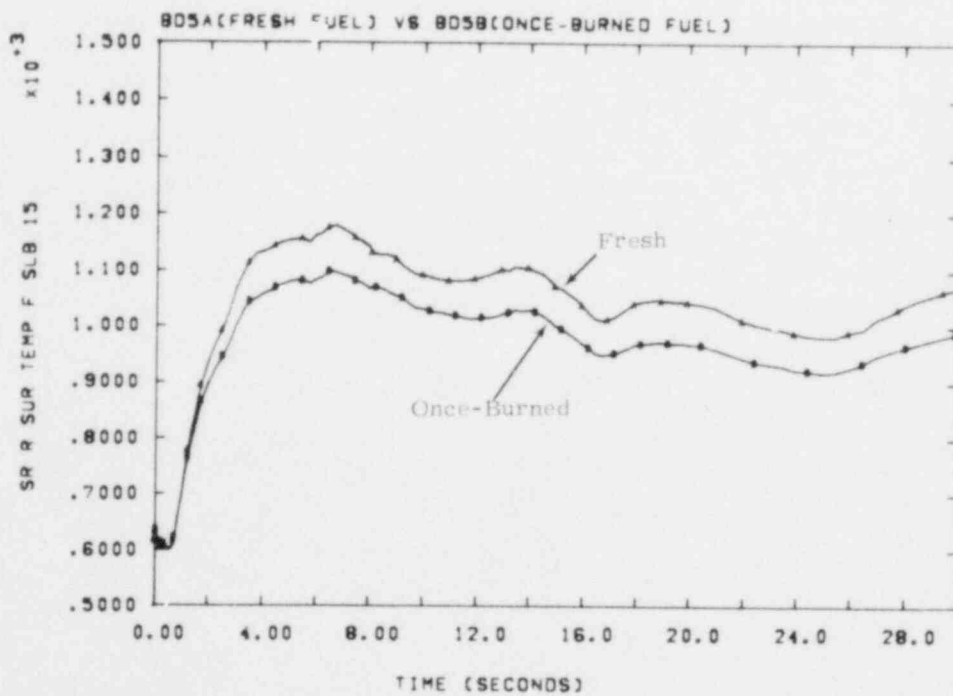


Figure 3-11. Slab 15 Temperature, Fresh and Once-Burned Fuel

For the temperature ranges expected in this group of calculations, we did not anticipate large consequences from the choice of metal-water reaction parameters. Fuel stored energy and flows to the downcomer and from the upper plenum, for example, were virtually unaltered (Figures 3-12, 3-13, and 3-14). Because of the difference in energy production rates, we expected, and observed, some changes in calculated temperatures, as seen in Figures 3-15 and 3-16. A somewhat puzzling result may be observed in Figure 3-15. At the conditions in the calculations around 11 s, the C-P parameters should, and do, produce the larger energy production rate. However, the temperature for this calculation is lower, and remains lower for the rest of the problem. It appears, from close examination of the calculated results, that the void fraction in the volume associated with Slab 14 decreases (from unity) more rapidly for the C-P calculation. This would make it cross the critical value (0.96) earlier, thus altering the heat transfer characteristics. We also note that the energy production rate from the metal-water reaction is insignificant at this time compared with that of the fuel.

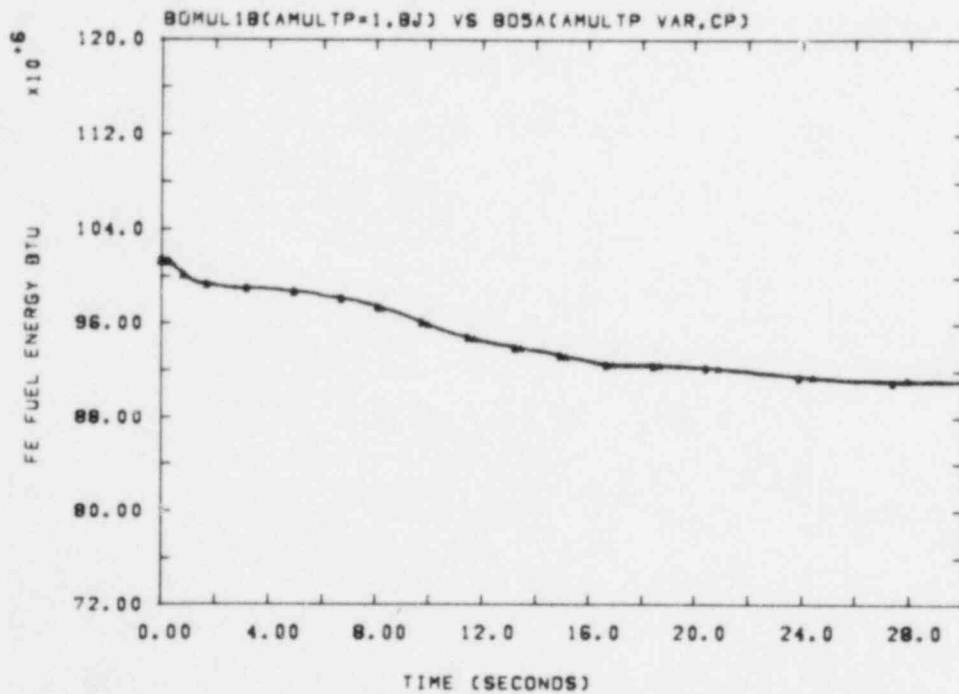


Figure 3-12. Fuel Stored Energy, Cathcart-Pawel vs Baker-Just Metal-Water Reaction

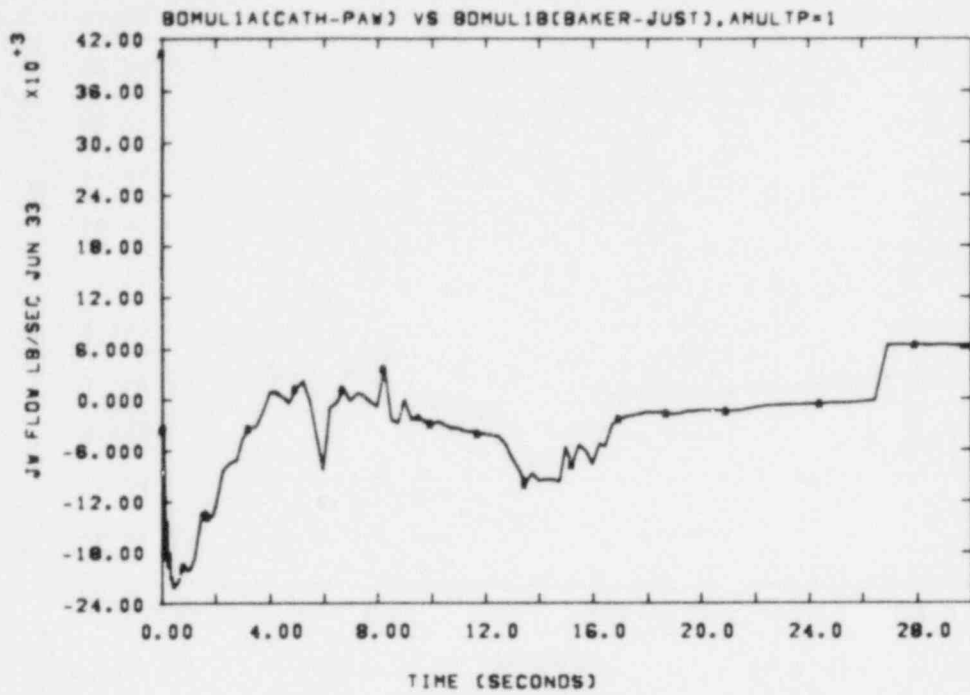


Figure 3-13. Flow to Downcomer, Cathcart-Pawel vs Baker-Just Metal-Water Reaction

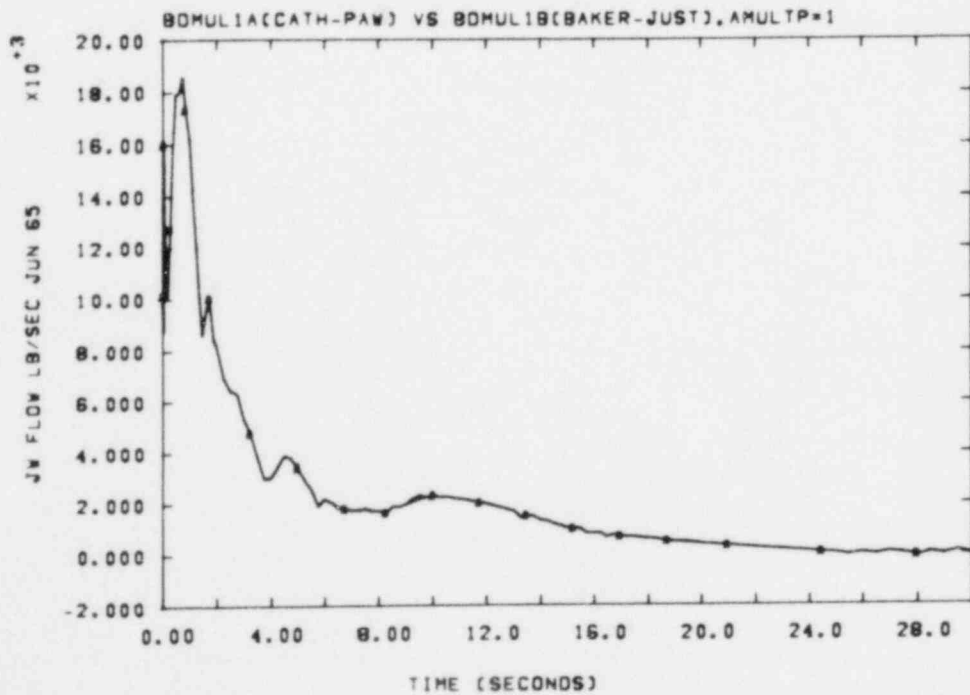


Figure 3-14. Broken Loop Flow From Upper Plenum, Cathcart-Pawel vs Baker-Just Metal-Water Reaction

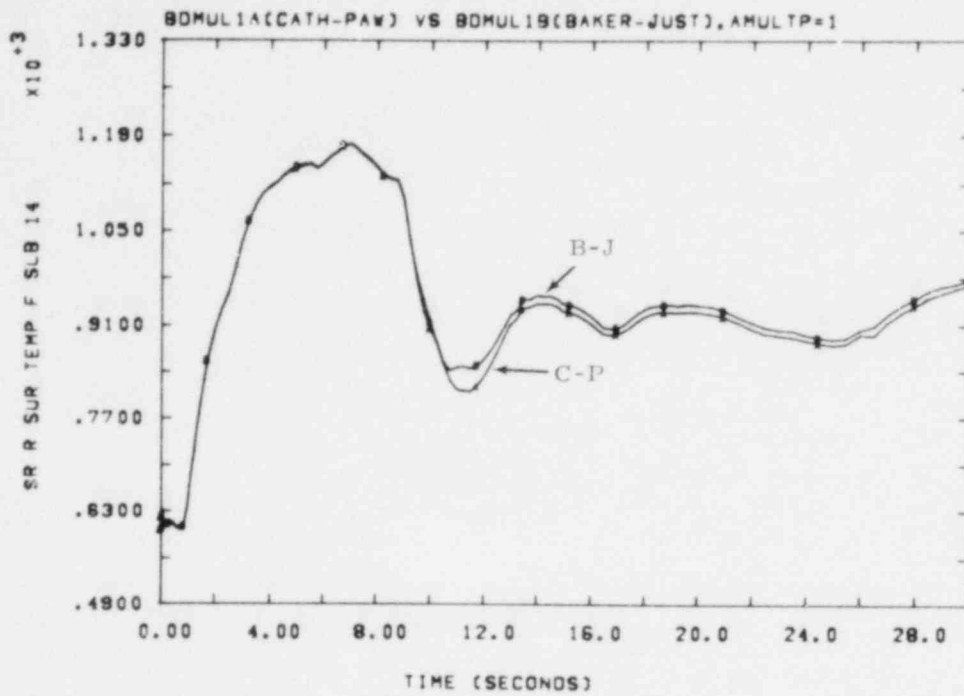


Figure 3-15. Slab 14 Temperature, Cathcart-Pawel vs Baker-Just

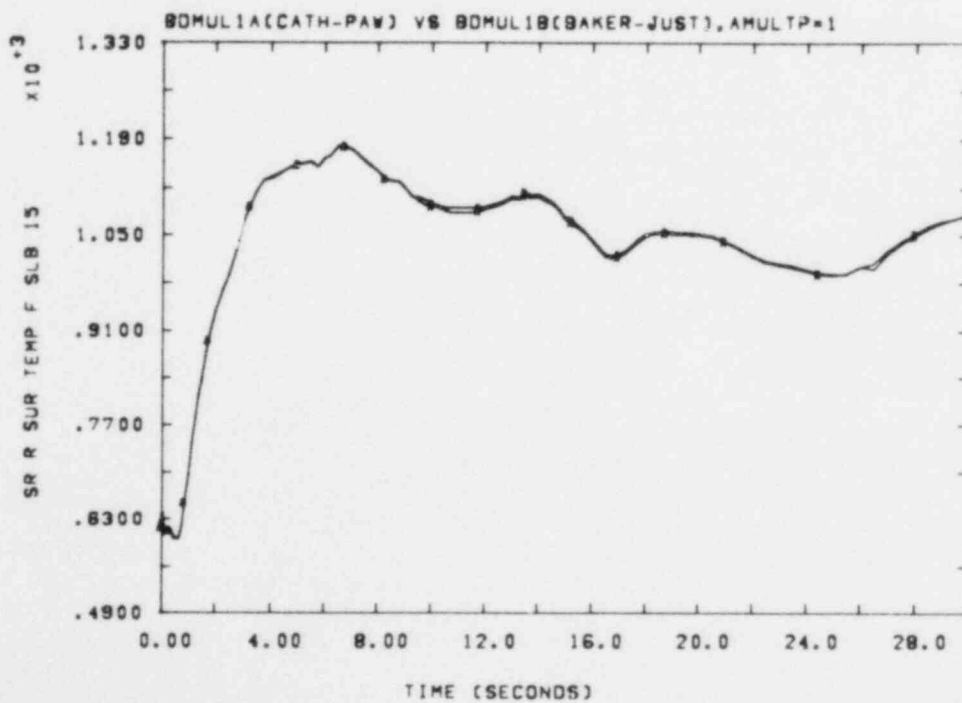


Figure 3-16. Slab 15 Temperature, Cathcart-Pawel vs Baker-Just

The effects of the choice of metal-water reaction parameters are somewhat accentuated by use of the old ANS decay heat rates. There is still no significant difference in fuel stored energy (Figure 3-17), but disparities in temperature histories increase by small amounts, as may be seen by comparing Figures 3-18 and 3-19 with Figures 3-15 and 3-16. Again, we observed no significant differences in hydrodynamic behavior. The effect of the choice of decay heat taken alone was also observed to be small; Figure 3-20 demonstrates a typical comparison of slab temperature histories.

Comparison between the nominal case (BD5A) and the case using once-burned fuel, old decay heat rates, and a high time-in-cycle (BDMULIC) yielded by now familiar effects: Figures 3-21 and 3-22 show the expected decreases in fuel stored energy and clad temperature, respectively.

Finally, we compared briefly the effect of using the new decay heat rate model vs 1.2 times the old model. Again, as anticipated, the significant differences appear in slab temperature histories (Figures 3-23 and 3-24). As was true for other comparisons among this set of calculations, we observed no significant differences in hydrodynamic behavior.

In summary, for the input variations we have considered in this set of calculations, we observed only one apparently anomalous result: the effect of the choice of metal-water reaction parameters. While analysis and calculated results indicate a higher energy production rate for the Cathcart-Pawel values, the Baker-Just values yield slightly higher temperatures. We saw virtually no differences in hydrodynamic behavior among the calculations; this is consistent with the fact that all variations made were connected directly only to fuel rod behavior.

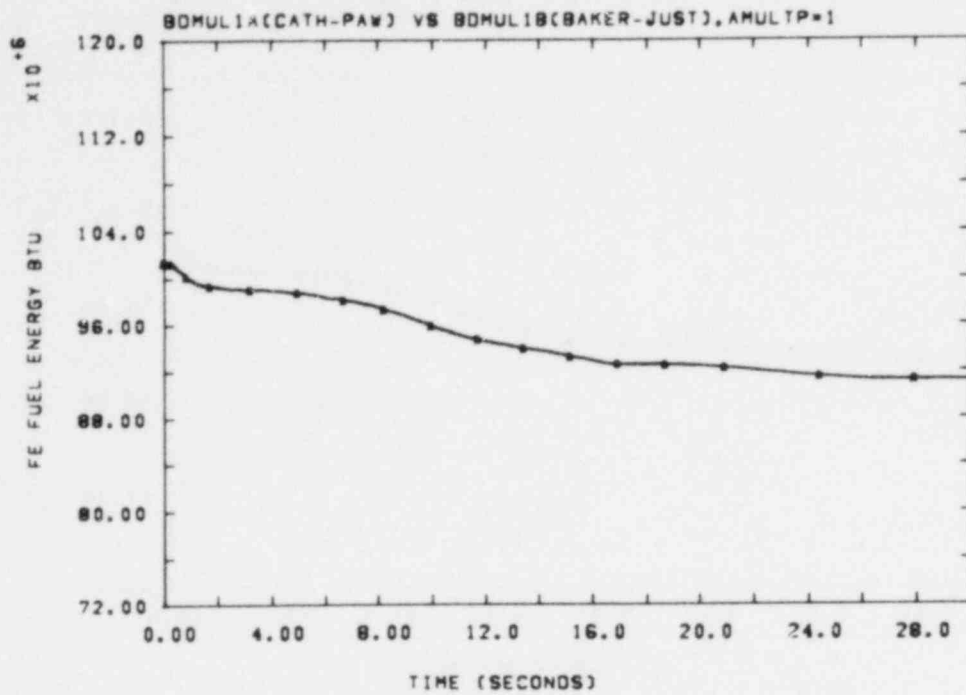


Figure 3-17. Fuel Stored Energy, Baker-Just and Old Decay Heat vs Cathcart-Pawel and New Decay Heat

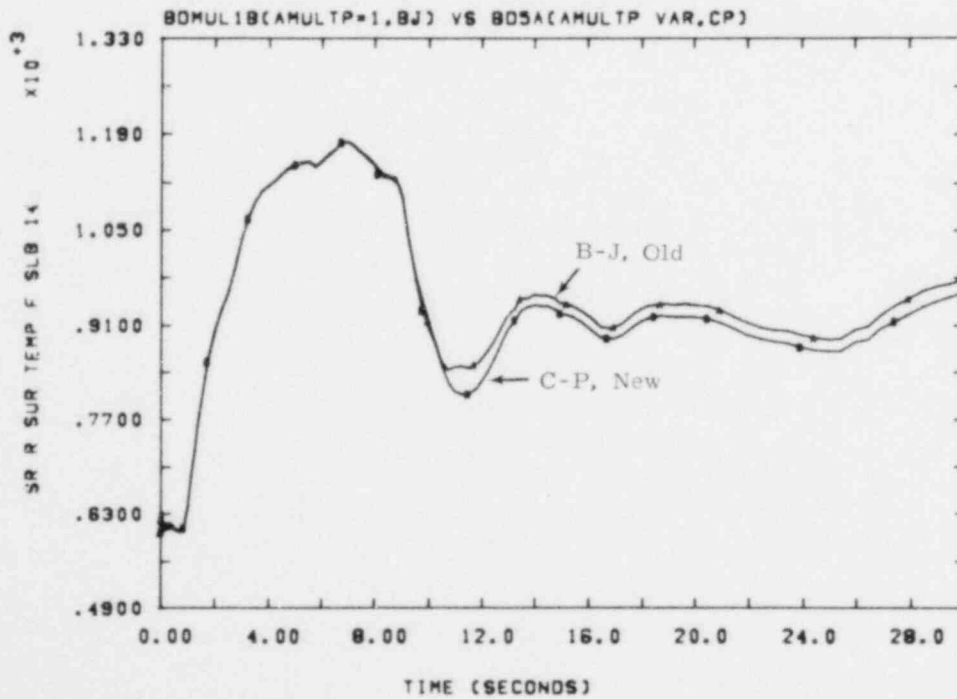


Figure 3-18. Slab 14 Temperature, Baker-Just and Old Decay Heat vs Cathcart-Pawel and New Decay Heat

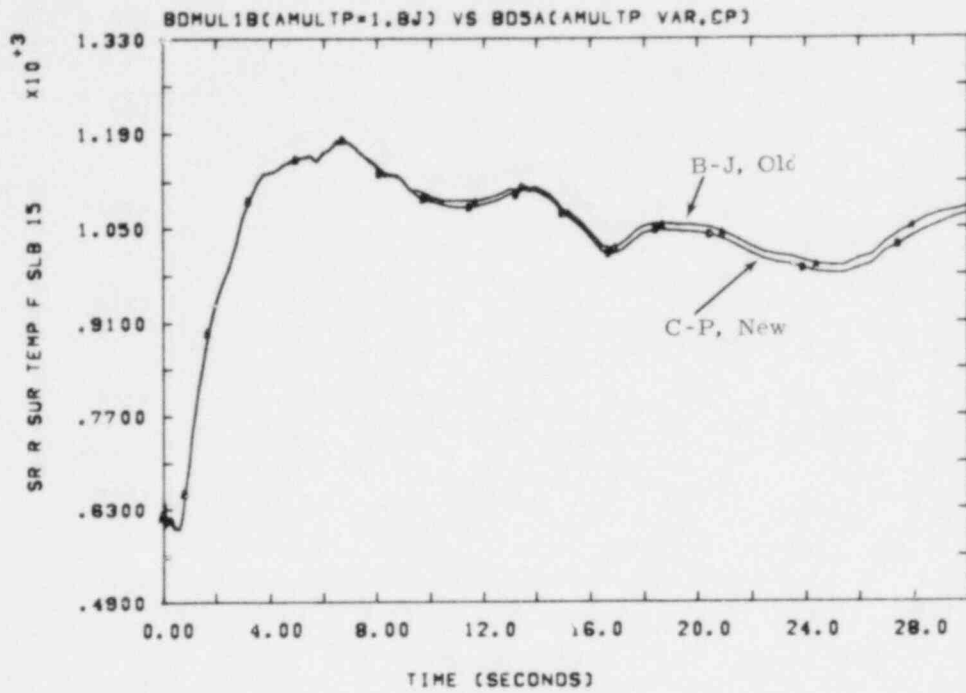


Figure 3-19. Slab 15 Temperature, Baker-Just and Old Decay Heat vs Cathcart-Pawel and New Decay Heat

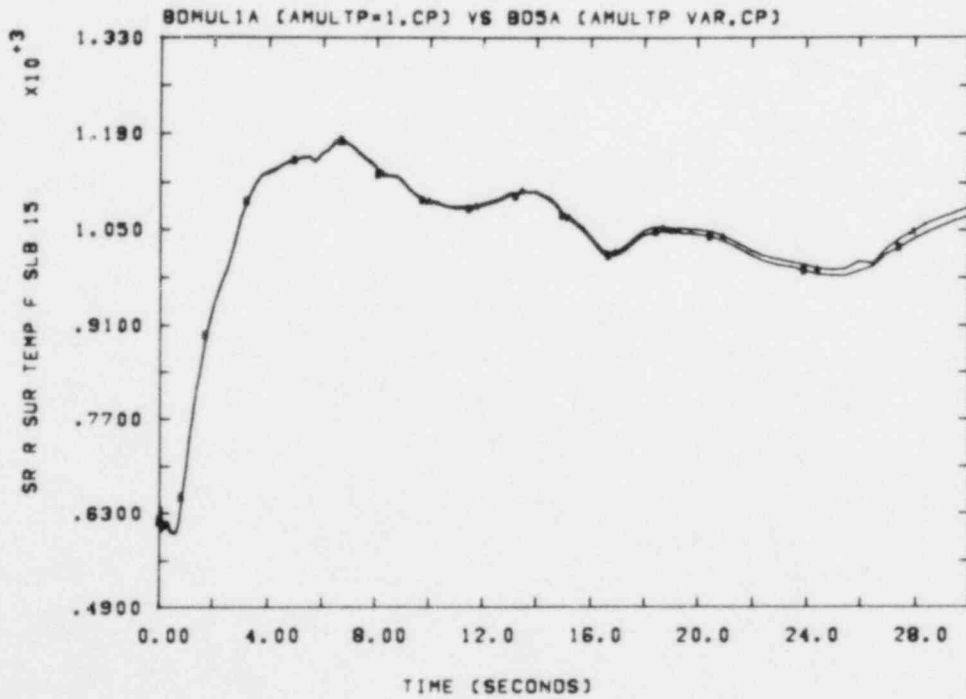


Figure 3-20. Slab 15 Temperature, Old and New Decay Heat Rates

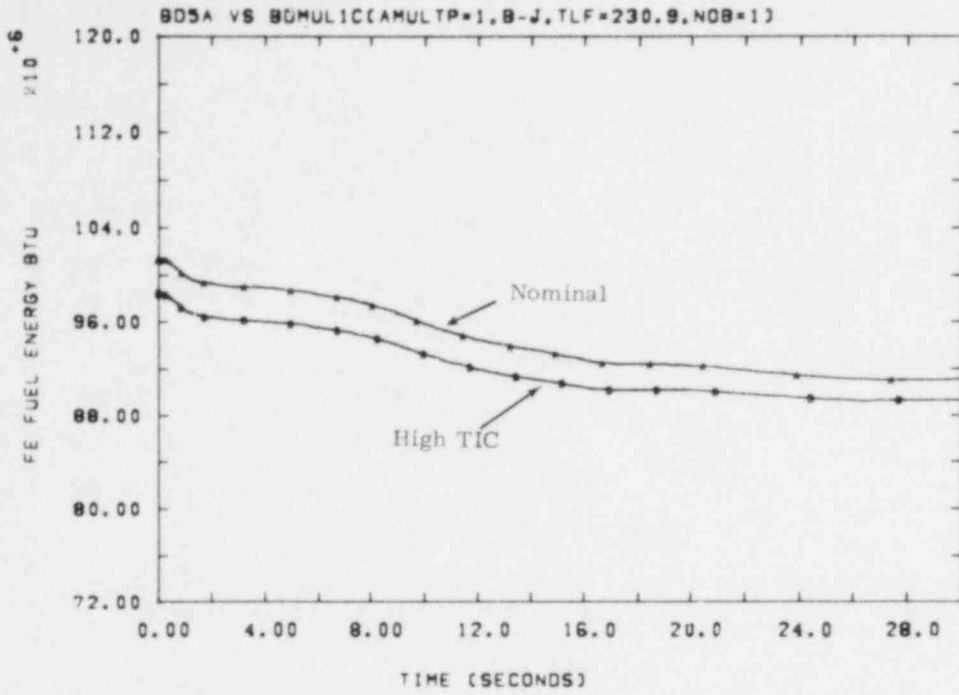


Figure 3-21. Fuel Stored Energy, Nominal vs High TIC

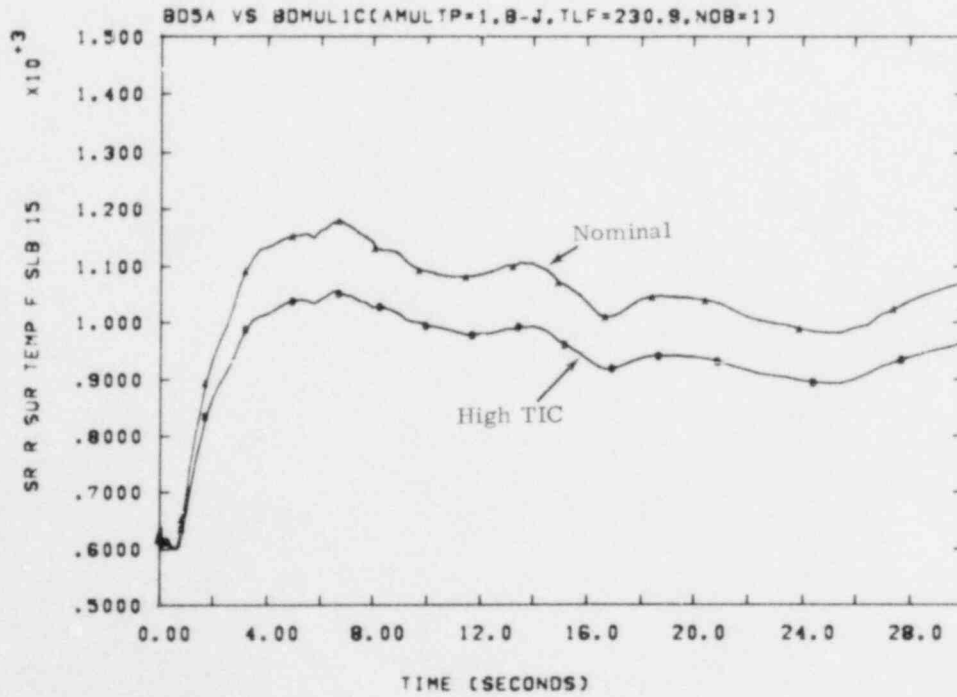


Figure 3-22. Slab 15 Temperatures, Nominal vs High TIC

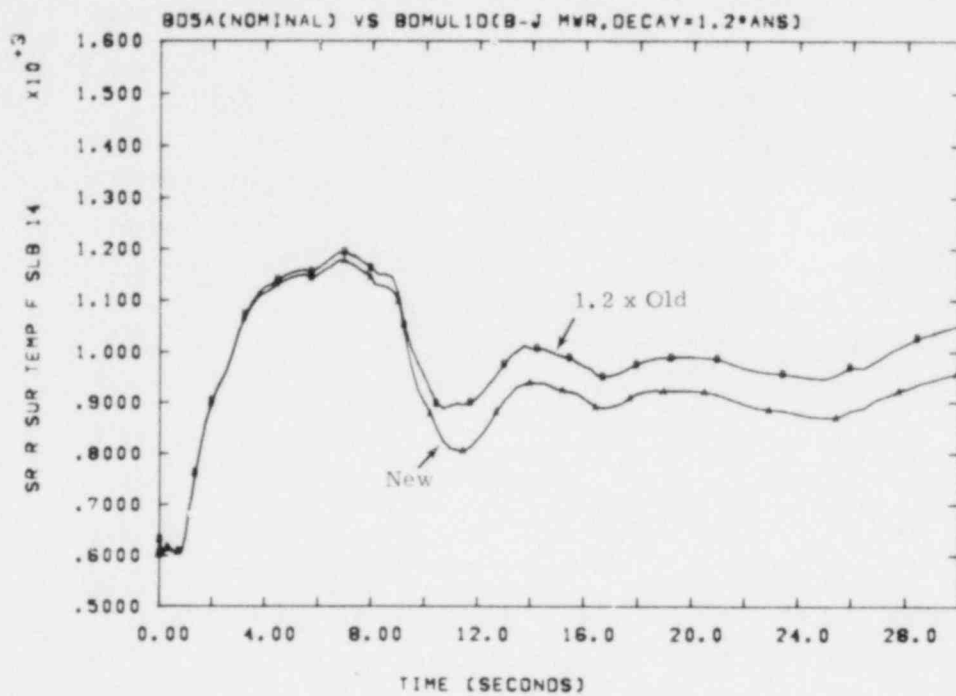


Figure 3-23. Slab 14 Temperatures. New vs 1.2 Old Decay Heat

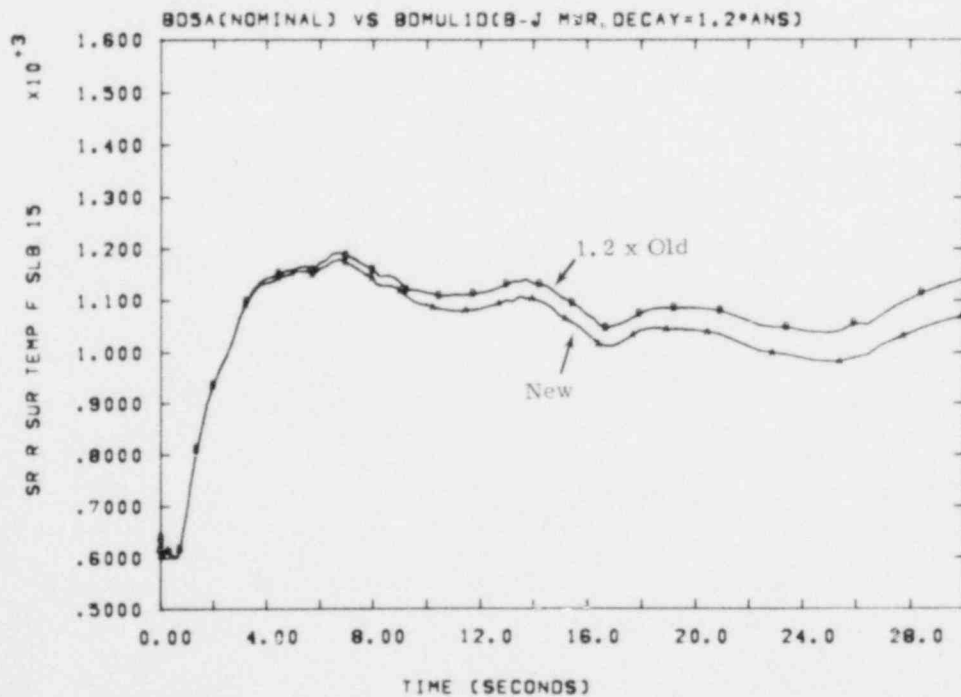


Figure 3-24. Slab 15 Temperatures, New vs 1.2 Old Decay Heat

3.3 Reflood Calculations

Work has begun on developing an acceptable procedure to perform the reflood phase of the statistical LOCA. The basic strategy was to use RELAP4/MOD6 to calculate the initial 20 s of the reactor blowdown. Then, because of the nonequilibrium conditions during refill, an algorithm would be used to 'bridge' the calculation from 20 s to the start of reflood (defined as the time at which the liquid level is at the bottom of the fuel rods). Finally RELAP4/MOD6, with the reflood options of heat transfer and moving mesh to follow the quench front, would be used to calculate the thermal-hydraulic conditions during the reflood phase until the time when the midplane of the rod quenched. These calculations would be performed numerous times to develop a response surface for the reflood PCT.

3.3.1 Refill Bridge

An algorithm to determine initial surface conditions at the beginning of reflood from the data at 20 s was developed at INEL.² This method provides fuel surface temperatures at the end of the thermodynamic nonequilibrium refill period. This strategy is illustrated in Figure 3-25. First, a correlation based on Semiscale data is used to obtain clad temperatures at 30 s from the 20 s RELAP values. Then, a modified adiabatic heatup period is assumed from 30 s to the start of reflood. An analysis of the input for the heatup phase indicates little sensitivity to physically realistic variations. For example, using a 10% higher heat transfer coefficient than recommended results in only a 0.2% change in the temperature.

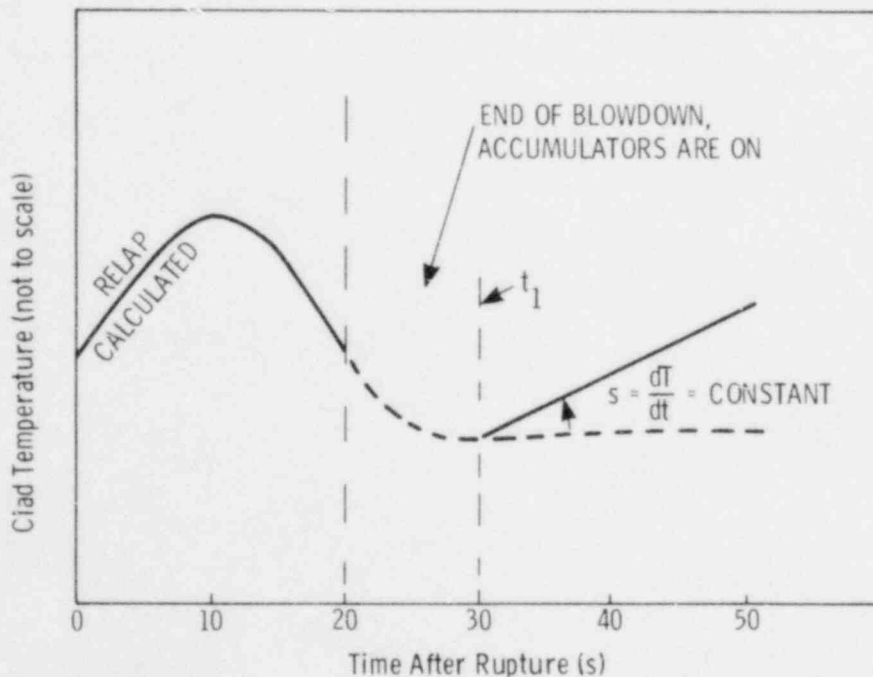


Figure 3-25. Conceptual Description of Refill Bridge

The bridge-predicted temperatures were only slightly higher than RELAP4/MOD6 results at 40 s; however, the predictions were about 50°F higher than TRAC results at 40 s. Both calculations were for a large PWR LOCA analysis. Therefore, it would be recommended that a statistical dial be incorporated into the bridge procedure. Its purpose would be two-fold: to account for the conservatism in the algorithm, and to provide a technique by which the contribution of the bridge temperature to the reflood PCT could be quantitatively determined.

3.3.2 Fuel Temperature Distribution

Since the reflood calculation will be initiated part way into the transient calculation, the steady-state fuel temperature procedure at initialization is not appropriate. Therefore, a fuel rod temperature distribution must be explicitly stated. A complication arises because the bridge algorithm discussed in the previous section provides only surface temperatures. An analysis of the blowdown statistical calculations indicates that the temperature drop from the fuel centerline to the clad surface for the average core and hot channel is about 50°F. The hot rod temperature drop varied from 50° to 250°F but is not modeled during the reflood calculation. Thus, the initial temperature profile will be determined by calculating the fuel centerline temperature assuming a statistically varying temperature increase to the bridge-predicted surface value and then determining the intermediate temperatures, using the linear interpolation scheme in the nodal coordinate system of RELAP. This method will result in a slight overestimate of the fuel stored energy.

3.3.3 System Conditions at Start of Reflood

For the beginning of reflood, the only initial condition which has been modeled is the fuel surface temperature. However, many other conditions are required and it is unclear what values some should have. For example, the question of permanent fuel clad deformation and clad oxidation thickness at the start of reflood are unanswered. Also, the effects of the flow blockage model using the single core volume are not known. In some cases, these initial values can be readily used as input for the RELAP models whereas others would require program changes.

Another problem area is the initial hydrodynamic state of the system. Based on initial TRAC results from the 12 kW/ft calculation, it is reasonable to assume the lower plenum and downcomer are filled with subcooled water and the remainder of the primary system with stagnant saturated steam at the pressure of the containment. However, the state of the secondary side of the steam generator has not been determined.

A problem area occurred in the reflood heat transfer surface (HTS-4) correlations during the startup of the calculation. A natural convection and radiation heat transfer correlation does not exist for core heat transfer; however, the assumed initial state of the system is stagnant steam. Work is in process to insert the appropriate correlation from the blowdown heat transfer surface (HTS-2) to replace the use of the Dittus-Boelter correlation. A minor problem occurred because the steam table properties routine for single phase (STH203) returns values for the liquid side of the vapor dome instead of the vapor side.

3.3.4 Decay Heat

A model was developed to bridge the radioactive decay heat from blowdown to reflood. A standard ANS decay table would not be satisfactory because the start time of the reflood is a statistical parameter and the generation of each decay group is coupled to the thermal-hydraulic environment of the fuel, which is varied in each blowdown calculation.

This algorithm initially assumes no generation in the decay groups. Therefore, the 11 standard delayed gamma emitter and U-239 and Np-239 group concentrations were advanced in time from the end of the blowdown to beginning of reflood by using an equation of the form

$$\gamma(t') = \gamma_0(0)e^{-\lambda t'},$$

where t' is the time measured from the end of blowdown. The concentrations of the 13 groups are readily available from RELAP restart data. This method was checked using a six volume RELAP nodalization calculated to 100 s. Essentially the RELAP code was used as a differential equation solver to calculate the coupled effects of the prompt and delayed groups. The algorithm deviated from the RELAP calculation by less than 1% when it was used to determine the power at 90s from the 20s concentrations. The difference is due primarily to the lack of a delayed neutron contribution. An exponential fit of this component could easily be performed on the six volume data and implemented as a constant additional component in the reflood calculation. Therefore, a method exists to couple the statistical variation during the blowdown phase to the heat generation calculation of the reflood phase.

3.3.5 Reflood Dials

In addition to the dial values used in the blowdown portion of the statistical study calculations (Table 3-V), input values unique to the reflood phase are required. Descriptions of these additional quantities are given in Table 3-VI, which may be considered a continuation of Table 3-V. It has not yet been decided what the ranges of the variables for the reflood study will be. Because of differences in modeling for blowdown and reflood, some of the first 21 statistical variables will influence the reflood calculations only by their effects on temperature at the beginning of reflood. Thus, because of the bridge algorithm, a response surface at 20 s would determine the important carryover parameters. The implementation of several of the other blowdown parameters is not readily obvious, as has been discussed in an earlier section. The remainder of the parameters are those unique to the reflood phase.

3.3.6 Future Work

A major program change occurred at the end of this quarter which directly affects the statistical reflood work. It has been decided by NRC that TRAC will be used in all further statistical studies. TRAC is capable of performing the blowdown-through-reflood phases in a continuous calculation. This eliminates the problems of initial system conditions and of implementing an algorithm to bridge the thermodynamic nonequilibrium code. Therefore, the majority of the problem areas for the reflood calculation should be resolved by the use of TRAC.

TABLE 3-V

Blowdown Statistical Dial Codes

1. C_D subcooled
2. C_D saturated
3. Slip
4. Form/friction loss
5. CHF
6. Condie-Bengston
7. Free convection and radiation
8. Dittus-Boelter
9. Hsu and Bromley-Pomeranz
10. Flow blockage
11. Cathcart-Pawel
12. Power
13. Containment pressure
14. Two-phase pump head
15. Accumulator and ECC temperature
16. Accumulator pressure
17. Time in life (fuel)^{*}
18. Peaking factor
19. Fuel conductivity
20. Gap thickness
21. Decay heat

^{*} Being dropped as an independent variable.

TABLE 3-VI

Reflood Statistical Variables Codes

22. Water swept out of lower plenum during blowdown
23. ECC bypass
24. Core entrainment
25. Deentrainment model from upper plenum
26. Fallback model
27. Forced convection to subcooled liquid
28. Nucleate boiling
29. Transition boiling
30. Film boiling
31. Dispersed flow
32. Superheated vapor
33. Natural convection and radiation
34. Energy partition
35. Steam generator heat slab temperature
36. Refill bridge
37. Non-core heat slab temperatures
38. Time of reflood
39. System initialization
40. Fuel centerline temperature

3.4 FRAP

The FRAPCON-1 steady-state fuel code has been received from INEL. The checkout problem has been performed and agrees with the INEL answers. The probable use of this code will be to verify the initial fuel state for the statistical analysis calculations.

3.5 Statistical Development

A total of 34 dial sets had been run by the end of the quarter, including 40 based on latin hypercube sampling (LHS) and 42 based on fractional factorial (FF) sampling.

The FF runs were made to address some criticism of the LHS approach. However, it is still our opinion that LHS is better for sensitivity studies than FF sampling, principally because it has worked better in the past.

The LHS method has been criticized because it gives rise to correlated inputs. While it is true that the inputs may be correlated, it must be remembered that in our response surface problem the responses are presumably without error. This means that correlated inputs can create numerical problems in a computer if the input matrix is nearly singular (inversion of a nearly singular matrix, for example) but it does not mean that moderate correlations are a priori bad. For example, imagine fitting a plane to 10 points which do, indeed, line on a plane. Unless these 10 points lie on line (correlation = ± 1), the correct plane can in principle be found, though there will be numerical problems if the 10 points lie too close to a line.

The LHS and FF methodologies were compared in a prediction study. Each set of points was used to create a model that would predict the other. The result was that the FF points predicted the LHS points with one-half the rms prediction error of the reverse. This should come as no surprise if one assumes that interpolation is better than extrapolation. When the FF points were doing the predicting there was interpolation in most coordinates; when the LHS points were doing the predicting there was extrapolation in all coordinates. The result of this prediction study does not necessarily demonstrate the superiority of FF sampling, but it does show the superiority of being "exterior" to where the predictions are made for certain situations.

During the quarter, changes were made in the modeling philosophy. Variable 17 (time in life) was dropped as an independent variable and, instead, incorporated into variables 18 (peaking factor uncertainty) and 20 (gap width dial), so that 18 became total peaking factor and 20 became the actual gap width. Models based on the new data and the new modeling considerations show variables 18, 19, and 20 (total peaking factor, gap conductance, and gap width) to be the dominant variables no matter how the modeling was done. Details of the modeling results will be presented shortly when the final report is prepared.

References for Section 3

1. Light Water Reactor Safety Research Program Quarterly Report, July - September 1978, M. Berman, Ed., SAND79-0359, NUREG/CR-0661, Sandia Laboratories, Albuquerque, NM, April 1979.
2. S. G. Margolis and C. A. Dolan, A Connection Between Clad Temperatures at End of Blowdown and Initiation of Reflood Based Upon Semiscale Experimental Data, CVAP-TR-78-022, Idaho National Engineering Laboratory, July 1978.

4. UHI Model Development

(T. J. Bartel, M. Berman, L. D. Buxton, R. K. Byers, R. K. Cole, Jr.)

4.1 Summary

Upper head injection (UHI) describes a new emergency core cooling system developed by Westinghouse for pressurized water reactors that use ice condenser containment systems. Analytic tools presently available for studying loss-of-coolant accidents (LOCA) are considered inadequate in treating several phenomena whose import has increased with UHI. These include, among others:

- Increased importance of two-phase flow with slip
- Occurrence of top quench in the core
- Upper head draining during refill.

Sandia has embarked on a model development and testing program to improve the treatment of these phenomena in the RELAP4 and TRAC codes. Following are the results for this quarter.

As reported last quarter, we have identified the basic source of the unstable slip behavior observed in RELAP calculations employing the Zuber-Westinghouse (ZW) slip model. Because the problem lies in the relative velocity correlation itself, and not in its implementation, we must in some sense "live with it," at least for now. During this quarter, we have investigated the interaction of the slip problem with other problem areas in the code, namely (1) the waterpacking correction, (2) the change to using incompressible-flow junction equations at low pressures, and (3) the junction specific volume calculation. Despite evidence of synergistic effects, we found no way to produce any significant improvement over previously reported calculations. However, we feel that the junction specific volume problem is more general, and deserves further examination.

Two problems involving RELAP4/MOD5 heat transfer were identified and corrected. Several calculations had terminated abnormally because of undiagnosed arithmetic errors in the heat transfer solution. The solution strategy, involving the modified Bromley film boiling regime, was changed to eliminate the problem. The Ross-Stoute gap conductance model was found to contain an improper multiplier. This has been removed.

We have continued to gain experience with the TRAC code, using nonrelease versions which contain many of the improvements to be included when P1A is released. Steady-state initialization of a PWR model was successful, using version 19.3, but unphysical behavior was observed in the subsequent attempt to simulate a double-ended cold leg break. A calculation of Semiscale MOD3 test S-07-1, using version 19.3, also indicated the need for some corrections in the code. Therefore, version 20.2+ was imported and installed. Because of errors found in this version, we are now waiting for TRAC20.3, expected early next quarter. We have found that plotting capability is essential to the interpretation of results of any large computer code, but no graphics package has been released for current versions of TRAC. Therefore, routines have been developed to generate one-dimensional plots from the TRAC graphics file, and work is proceeding on two- and three-dimensional plot routines.

4.2 Calculational Experience

As previously reported, we have determined that the stability of the RELAP conservation equations including slip is dependent on the particular relative velocity correlation used. When the ZW correlation is employed, the equations are almost certainly unstable in some flow regimes, notably the churn-turbulent-bubbly regime near the transition to film-annular flow at a void fraction of about 0.8. This instability expresses itself as large, unphysical oscillations in flows and pressures, particularly obvious in the downcomer at the time accumulator water starts to penetrate. The reduced time-step necessary to calculate these unphysical oscillations also often leads to a substantial increase in computer time required for a calculation.

Some improvement in behavior was obtained by modifying the correlation slightly to make the drift velocity V_{gj} and the distribution parameter C_o continuous functions of the void fraction α with continuous first derivatives. The basic calculation using this modified correlation and the nodalization referred to as UHL (Figure 4-1) was denoted UHL2G, and was described last quarter.

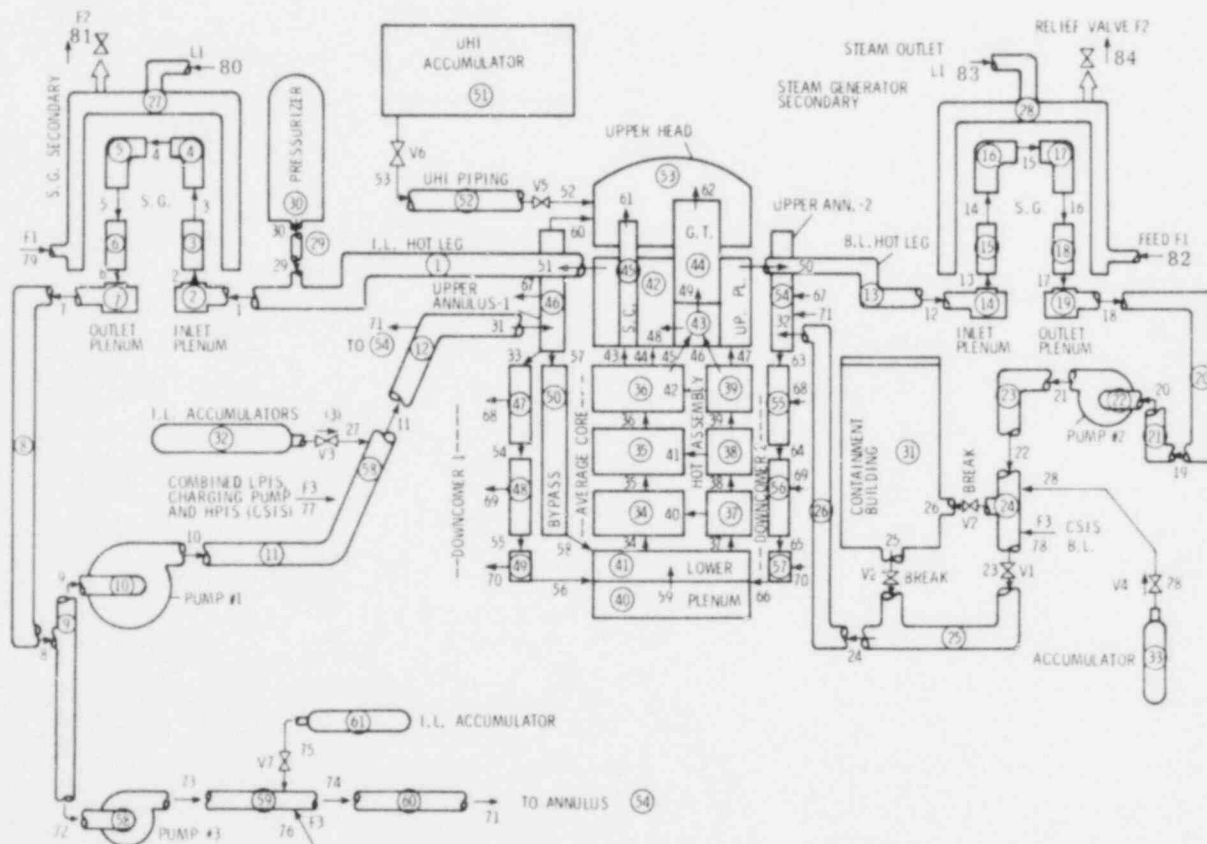


Figure 4-1. UHL, an Upper Head Injection Nodalization Scheme With Azimuthally Noded Downcomer

It is not clear how to further modify the ZW correlation to achieve stability of the RELAP equations. Therefore, at least in the short term, the only hope of producing an improved calculation seemed to be identification and elimination of additional "triggers" for the unstable behavior, as we did in smoothing the correlation. Three such potential "triggers" were suggested by careful examination of previous runs:

1. The waterpacking correction. Episodes of waterpacking were found to begin in the intact loop volumes just downstream of the pumps (the point of ECC injection) and propagate into the vessel, arriving at about the time that oscillatory behavior was first observed.
2. The change in momentum equation form at low pressure. Following past practice and Idaho National Engineering Laboratory (INEL) recommendations, the momentum equation option MVMIX = 0 (compressible flow with momentum flux) is only used at high pressures. In our version of the code, all junctions are reset to use MVMIX = 3 (incompressible flow without momentum flux) when the pressure in some volume (taken as core bypass, volume 50) falls below 50 psia. This change, and the disturbance resulting from it, appeared to occur just before the onset of oscillations.
3. The junction specific volume calculation. We had some evidence that part of the problem with use of MVMIX = 0 at low pressure involved the calculation of junction specific volume. This is an attempt to correct the donor-volume value for effects of mixture level, enthalpy transport, frictional losses, and the difference between "stream" (at junction location) and volume-center kinetic energy. As originally coded, this last correction is made using the previous time-step value for the stream kinetic energy. This produced unstable behavior in test problems, with the junction specific volume alternating between unreasonably small and unreasonably large values on alternate time-steps.

The first was easily investigated by turning off the waterpacking correction completely. This was found to require a reduction in maximum time step from 5 to 1 ms for the interval from 40 to 50 s. The second required removal of the code which reset MVMIX. The third was slightly more difficult. Our solution was to modify the routine PREW so that the stream kinetic energy was implicitly brought to the correct time level. Essentially, this required solution of a quadratic equation for the junction specific volume.

Several calculations were performed (Table 4-1) as variations of the basic UHL2G calculation. Because they were essentially test cases, each was terminated as soon as it had produced enough data to determine if a significant improvement had been achieved.

As may be seen by comparison of Figures 4-2 through 4-6 (note the different time scales, and the increased slab frequency in 4-3 and 4-4), no significant improvement was achieved in any case.

TABLE 4-I

UH, Test Calculations

UHL2G	Base case. Spline-smoothed ZW slip and all previous code corrections. Waterpack correction on at 10 s.
UHL2GC	UHL2G with waterpack correction off. Required reduced time-step from 40 to 50 s.
UHL2GC3	UHL2GC with no momentum equation change: 1 with UHL2GC (reduced) time-steps, 2 with UHL2G time-steps.
UHL2GC3S	UHL2GC (2) with consistent junction specific volume calculation. [*]

^{*} Also includes the improved Mode 6 heat transfer solution strategy described in Section 4.3.

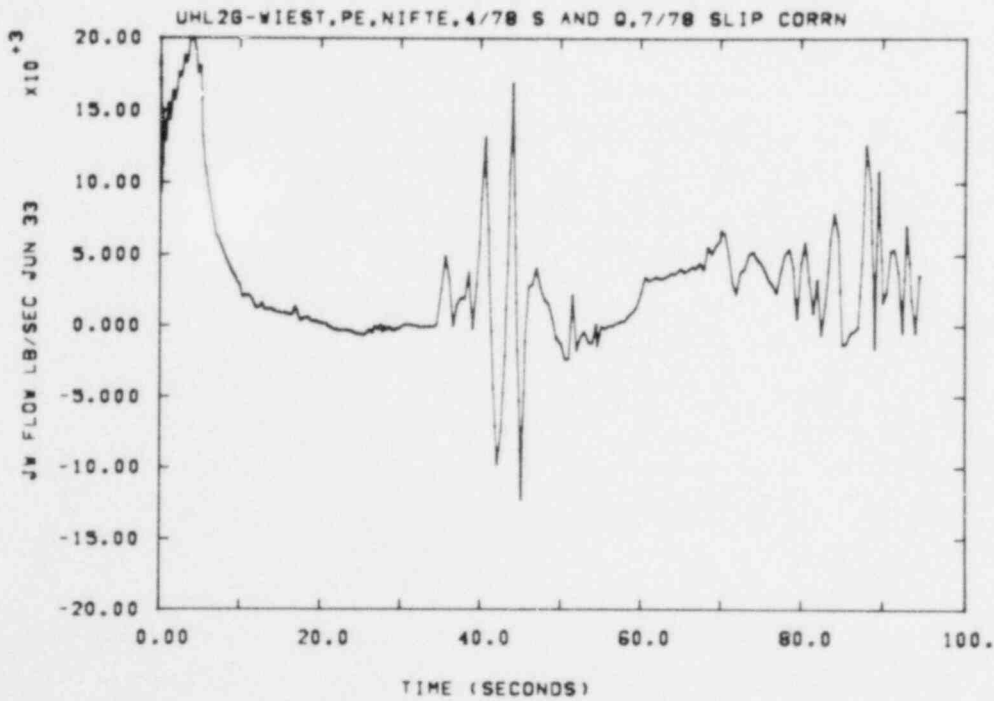


Figure 4-2. Mass Flow at Top of "Left" Downcomer, Base Case

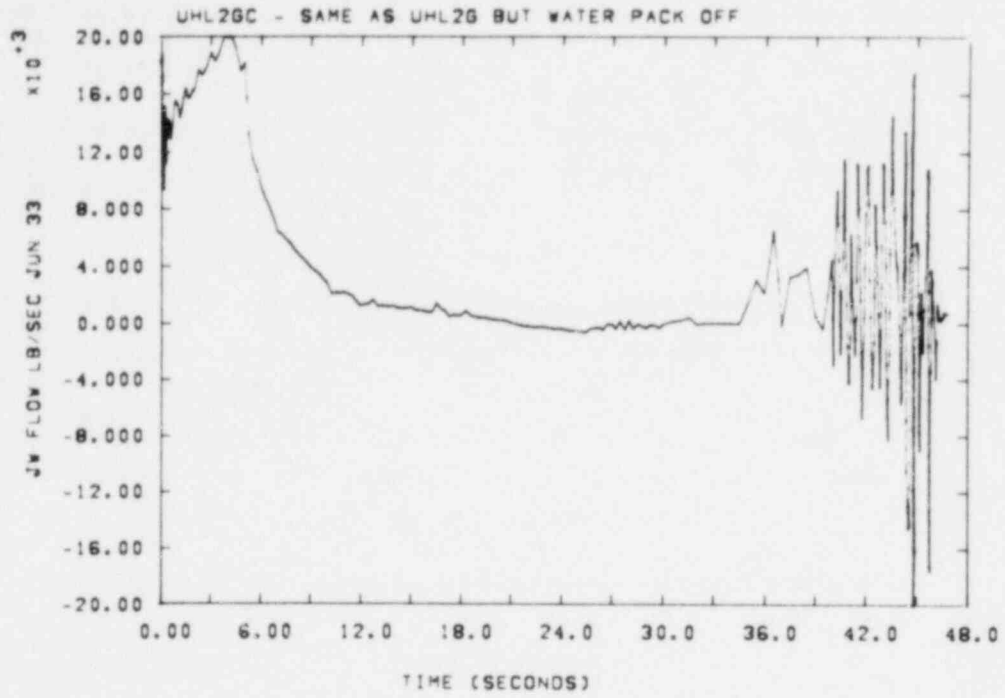


Figure 4-3. Top Left Downcomer Flow, Waterpack Correction Off

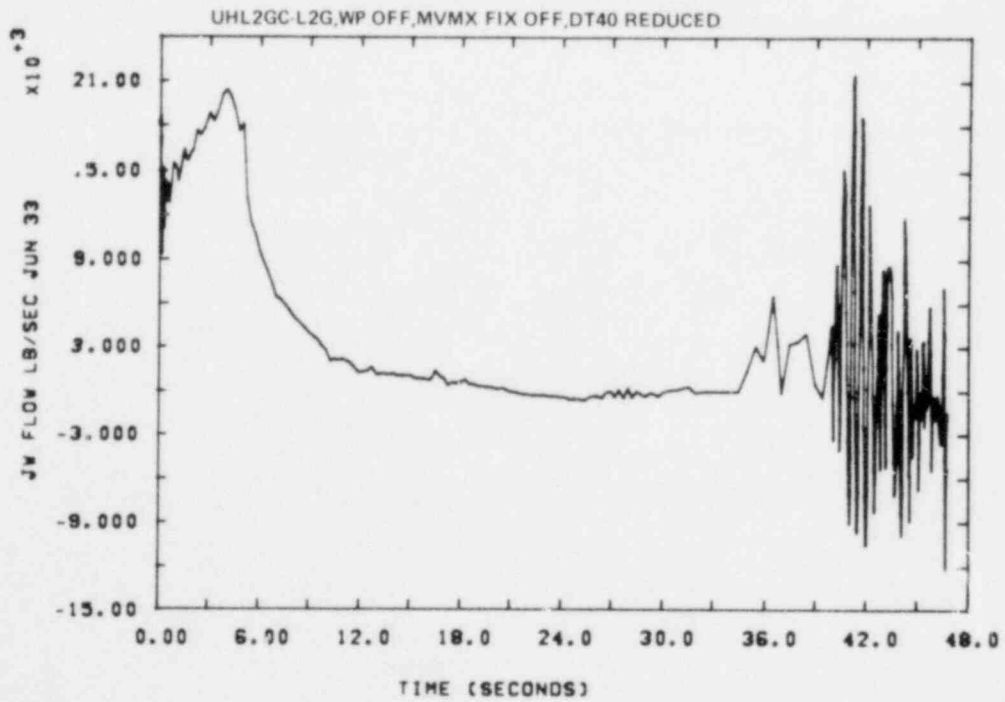


Figure 4-4. Top Left Downcomer Flow, No Flow Equation Change, DT40 Reduced

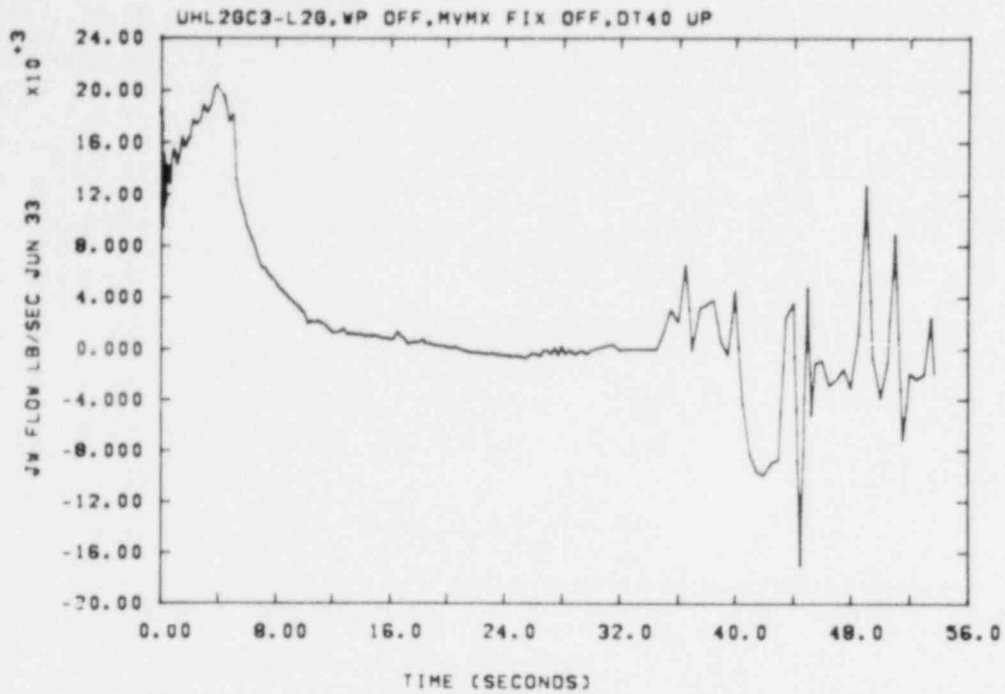


Figure 4-5. Top Left Downcomer Flow, No Flow Equation Change

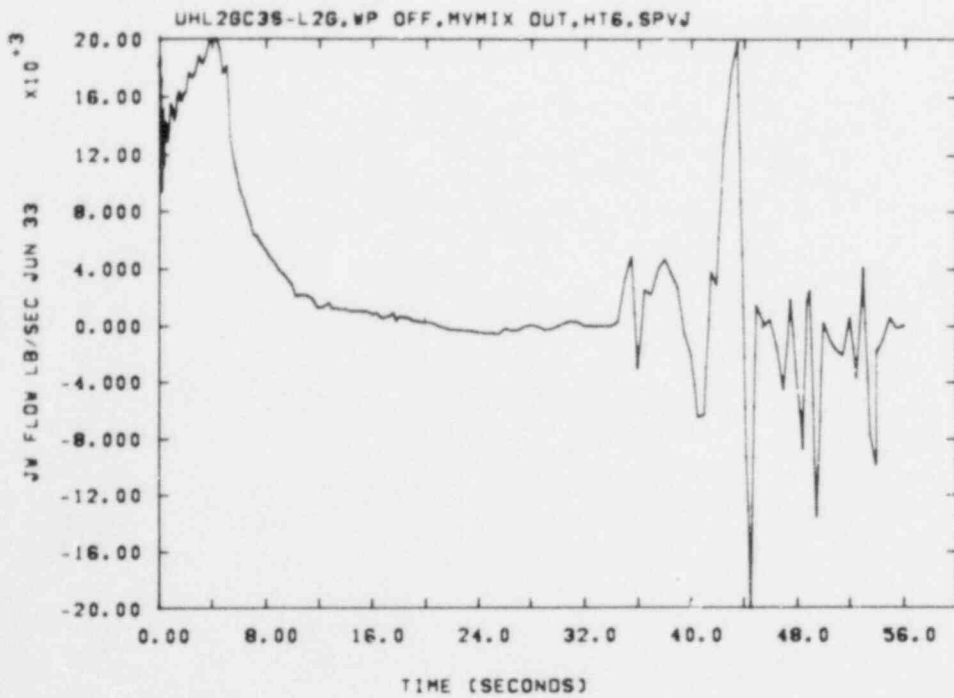


Figure 4-6. Top Left Downcomer Flow, Consistent Junction Specific Flow

We feel that the junction specific volume calculation deserves further consideration. The present version is at least unstable and perhaps wrong, and may be causing unrecognized problems in other areas.

4.3 Heat Transfer

Several calculations had terminated abnormally because of arithmetic errors in the heat transfer solution. This was traced to an attempt to evaluate the modified Bromley low-flow film boiling correlation (Mode 6) for negative superheat. Because the heat transfer is a function of $\Delta T^{0.75}$ where $\Delta T = T_{\text{SURFACE}} - T_{\text{SATURATION}}$, this caused a fatal arithmetic error.

RELAP4/MOD5 first determines coefficients in a conduction equation solution at the surface in the form $Q_C = AT_{\text{SURFACE}} + B$, and then uses an iterative scheme involving the heat transfer correlation to determine T_{SURFACE} . This can be written in the form $Q_C = A \Delta T + \beta$. As seen in Figure 4-7, no Mode 6 solution exists unless $\beta > 0$. That is, an intersection between the conduction and convection (Q_C) solutions exists only for positive β . Therefore, the problem can be avoided by first evaluating β and then calling the Dittus-Boelter (Mode 1) correlation if $\beta < 0$, eliminating any attempt to evaluate Mode 6. This changed strategy has been implemented in our version of RELAP4/MOD5 and has completely eliminated the arithmetic errors.

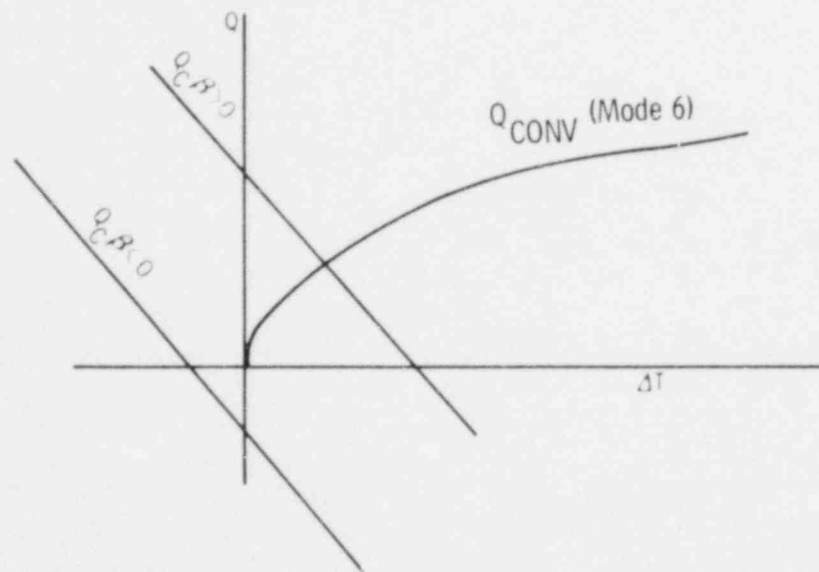


Figure 4-7. Mode 6 Heat Transfer Solution.

During an investigation of the gap conductance models used by RELAP4, it was noticed that the MOD5 version used at Sandia had a multiplier of 10.0 on the Ross-Stoute model. Although this model is regarded as conservative in the heat transfer calculations, the multiplier effectively eliminated the gap effect in the calculations due to the large conductivity. Therefore, the multiplier has been removed and all subsequent calculations will have the original Ross-Stoute model.

INEL is about to send a revised program tape of FRAPT4-LACE to correct the earlier version. This will contain all the LACE options to be used in the fuel modeling.

Future Work -- The effect of the Westinghouse carryout rate fraction on the core reflood rate will be investigated. Also, the sensitivity of reflood results to the number of core heat slabs, initial surface temperature, and exit core enthalpy will be determined.

4.4 TRAC-UHI

The TRAC code, developed by Los Alamos Scientific Laboratory,¹ was exercised on two different problems this quarter. The purpose of performing these calculations was to evaluate the ability of the initial version of TRAC (19.3) installed at Sandia to predict thermal hydraulic behavior in a normal pressurized water reactor (PWR). This was in preparation for performing similar calculations in a UHI configuration.

4.4.1 Four-Loop PWR

The first problem considered was the full-scale, four-loop PWR sample problem, the noding for which was furnished with TRAC. A schematic of the configuration used to calculate the steady-state behavior is shown in Figure 4-8. Two calculations were actually performed, one in which the reactor power was initialized at 2.68 s after the pumps were turned on and one with power initialization at 20 s after the pumps started. Figures 4-9 through 4-12 contain comparison plots for several representative variables from those calculations. It is seen that there were considerable differences in the values calculated at early times for each of these variables, starting when the power was turned on at 2.68 s for the first run. However, as shown, both calculations ultimately converged to about the same steady-state values. Slight differences were seen in the final upper head liquid temperatures (Figure 4-13); those differences were apparently caused by the fact that the flow areas to the upper head were so small that the steady-state criteria were satisfied even though a "true" steady state was not attained. Overall, the agreement seen in calculating the steady-state results is very encouraging in establishing the basic abilities of the TRAC code.

Following the generation of the four-loop PWR steady-state values, the configuration shown in Figure 4-8 was altered by replacing pipe 1 with two shorter pipes, both of which were connected to low-pressure breaks. This configuration was used to model a 200%, double-ended, guillotine break in the cold leg of one of the four loops. The time-dependence of the low-pressure breaks was chosen to simulate containment pressures expected during blowdown.

TRAC was exercised in the transient mode by using the configuration described above. The calculation was run to about 30 s of transient time. It was discontinued at that time, however, because peculiar behavior was observed to start at about 16 s. This behavior was seen in the cold legs of all three intact loops between the reactor vessel and the points where the accumulators inject cold water. The high-pressure and low-pressure injection systems also inject water in that section of the cold legs. All of the cold water being injected was instantaneously vaporized, even

though the heat sources did not appear to be sufficient to cause that. The pressure was also very low, less than 1 atm, near the injection points where this occurred.

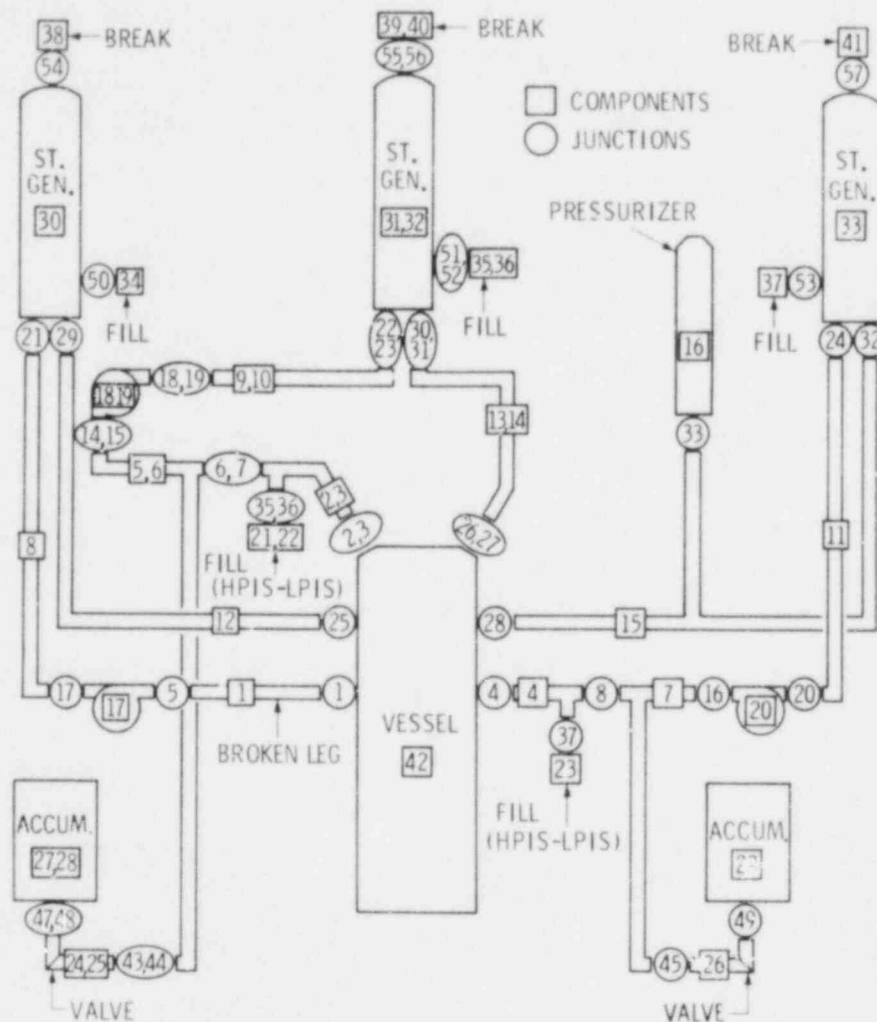


Figure 4-8. Configuration Used for Full Scale, Four-Loop Power Steady-State Calculations

There is a possibility that this behavior was caused by the use of tees with fully implicit primary tubes and semi-implicit secondary tubes, but the exact cause of the peculiar behavior was never determined since the version of TRAC (19, 3) which was used for these calculations was discontinued shortly after they were made.

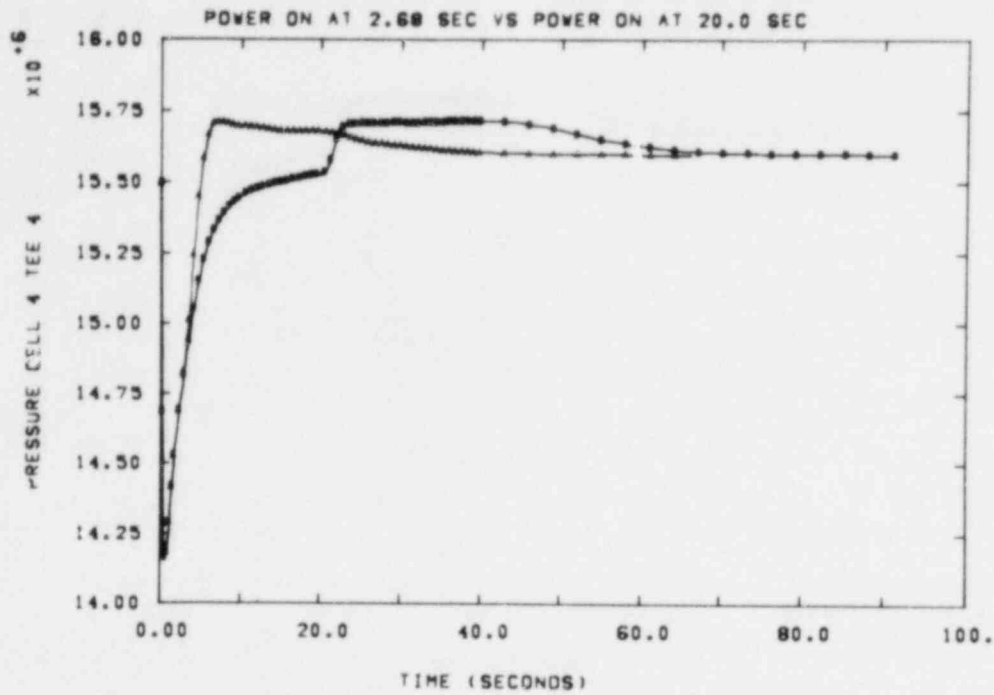


Figure 4-9. Comparison of Calculated Pressures in the Pressurizer Loop Near the Reactor Vessel

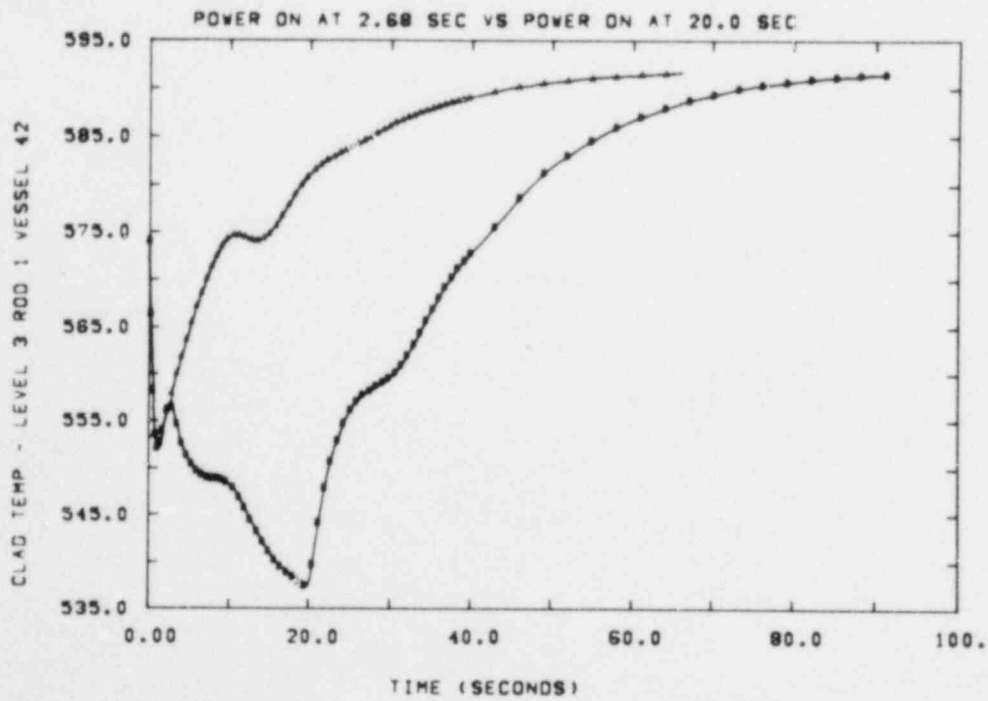


Figure 4-10. Comparison of Clad Temperatures Near the Core Center

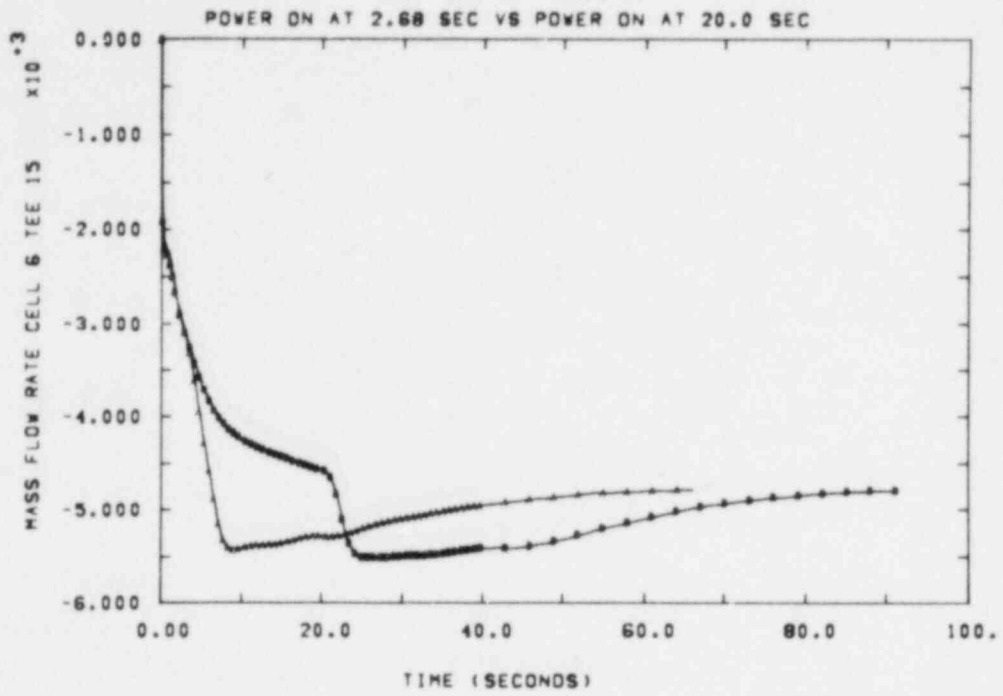


Figure 4-11. Comparison of Mass Flow in the Pressurizer Loop Near the Reactor Vessel

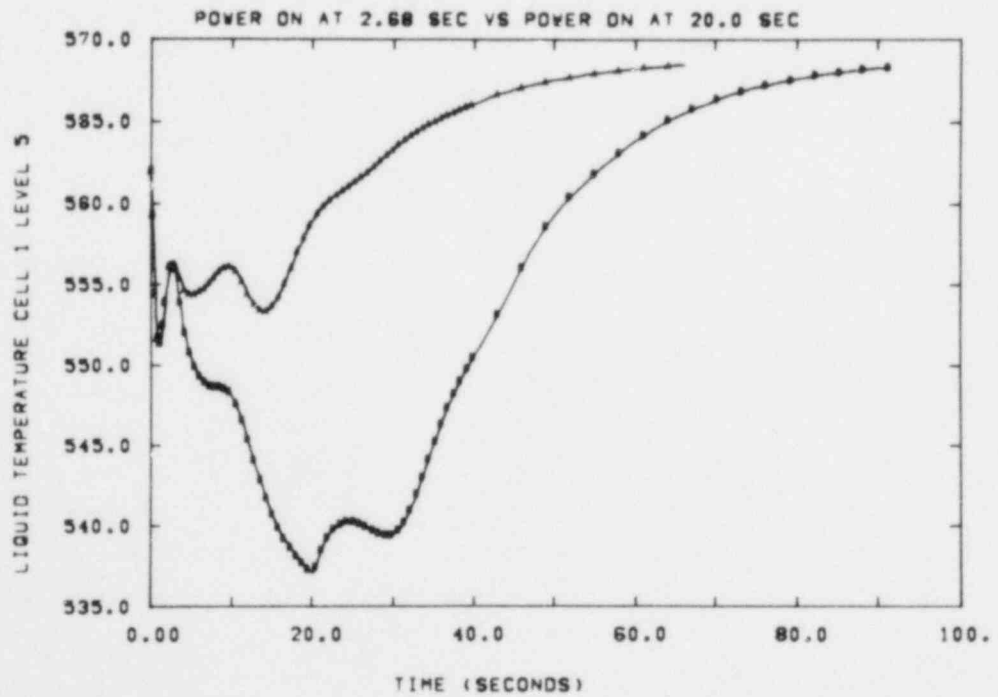


Figure 4-12. Comparison of Liquid Temperatures Near the Core Center

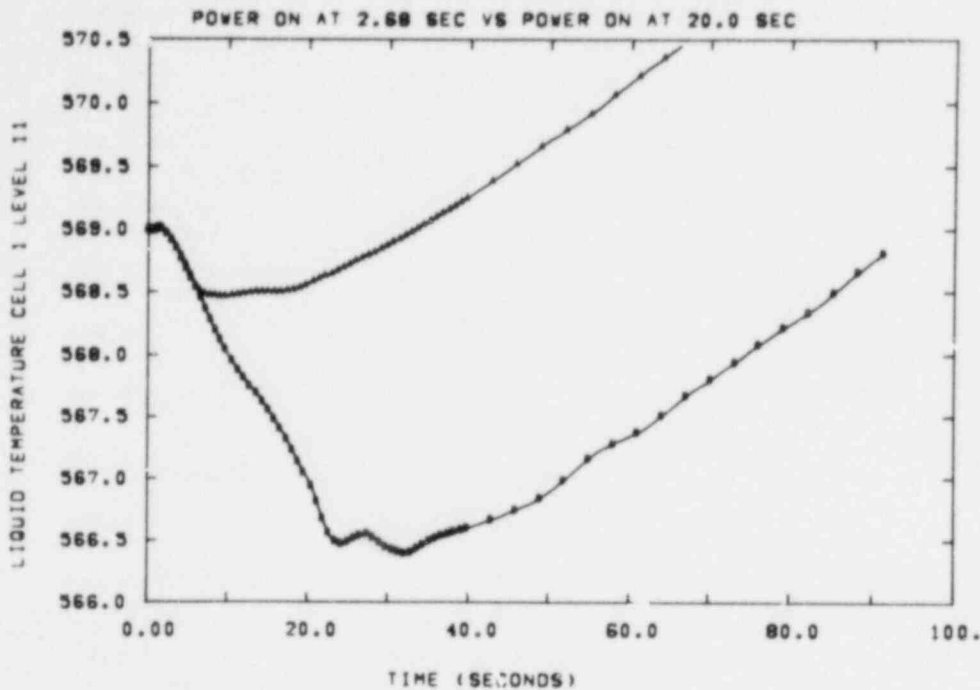


Figure 4-13. Comparison of Liquid Temperatures in the Upper Head

4.4.2 Semiscale MOD3

The second TRAC problem considered was one of the Semiscale MOD3 experiments, specifically test S-07-1. That particular test was chosen because, at the time this work was begun, more data was immediately available for it than for any other MOD3 test. It was also chosen because of its similarity to test S-07-6, for which downcomer water level oscillations of considerable interest were observed experimentally. The Semiscale S-07-1 calculations were initiated in cooperation with J. J. Pyun, of Los Alamos, who provided the initial nodding of the problem. He was simultaneously performing S-07-6 calculations at Los Alamos with that nodding.

According to Pyun, the output for the initial S-07-1 steady-state calculation at Sandia indicated certain corrections needed to be made to the version of TRAC being used at Sandia before the Semiscale problems could be correctly modeled. Since the version of TRAC being used (19.3) was several months outdated, the decision was made to import a completely new version (20.2+) rather than to attempt to selectively update the 19.3 version. This was accomplished fairly easily, with only a few minor TRAC modifications to accommodate operating system differences. Minor changes also had to be made to the Sandia-developed plotting routines to accommodate the modified graphics file structure in the 20.2+ version of TRAC. Unfortunately, after these changes were ready, it was discovered that several indexing errors were present in TRAC 20.2+. Therefore, provisions were made to replace it with version 20.3 early in the next quarter.

Note that neither of the versions of TRAC which have been installed at Sandia have been officially released versions. Instead, each was the most current version available at the time of implementation. The purpose for using such preliminary and only partially tested codes is to ensure the use of the latest improvements in models and numerical techniques. The versions used were considerably advanced from the version of TRAC-P1 released originally, and contained most of the features of TRAC-P1A which was not yet ready for release.

4.4.3 TRAC Graphics

The development of a one-dimensional plot capability to process the TRAC graphics file output was completed this quarter. Any of the cell-centered or cell-boundary variables present in the graphics file can now be plotted vs time. Variables can be plotted for selected time intervals or at all times for which the graphics file contains data. The ordinate scale is automatically set by the minimum and maximum array values but it can be overridden by input values. With minor modifications, plots from different runs can also be cross-plotted on the same figure, as was done in Figures 4-9 through 4-13.

Another plotting capability for which development was nearly completed this quarter is the ability to plot several adjacent node variables at a given time. This capability was developed so that the variation in selected variables around a complete loop of piping could be more easily visualized. The basic methods of generating these plots have been determined, but the models are not quite ready for general production use.

Work on two-dimensional vector and dot density plots and three-dimensional surface plot capabilities was also begun this quarter. These capabilities are being developed so that the variation in variables such as pressure, temperature, and velocity over two-dimensional slices through the reactor vessel can be graphically illustrated. Only preliminary work has been done in this area. It may be abandoned if the graphics package scheduled for release with TRAC-P1A provides sufficient capabilities.

Reference for Section 4

TRAC-P1: An Advanced Best Estimate Computer Program for PWR LOCA Analysis, NUREG/CR-0063, LA-7279-MS, Vol. 1, Los Alamos Scientific Laboratory, Los Alamos, NM 87545, June 1978.

5. Two-Phase Jet Loads (D. Tomasko)

5.1 Summary

The purpose of this study is to develop an improved approximate engineering model to characterize two-phase jets emanating from circumferential or longitudinal breaks in a typical PWR piping system. This model will be used to replace the currently used Moody model which assumes asymptotic jet expansion and thermodynamic equilibrium.¹

The actual development of the improved engineering model for two-phase jet loads has been divided into six phases, some of which will occur simultaneously. These are: investigating which of the available computer codes are applicable to the jet load problem and establishing background on their use; selecting the code which best simulates the two-phase jet; performing nodalization and parametric studies; acquiring experimental data on two-phase jets for use in model verification; and developing a final engineering model.

Presently, experimental data on two-phase jet loading have been acquired from the Federal Republic of Germany (FRG). These data are from Kraftwerk Union (KWU) in Erlangen (Research Projects BMFT RS93 and RS93A), Research Project RS-50 performed by Battelle-Frankfurt, and the Superheated Steam Test Facility (HDR). In all cases, the data are incomplete and the piping geometries used are difficult or impossible to model. However, the data are useful in determining some physical properties of the two-phase jet (radial and axial pressure profiles) and, with suitable approximations, can be used in computer code evaluations.

Two codes are currently being tested to determine their applicability to the two-phase jet problem. These are CSQ² and BEACON/MOD2.³ CSQ is a thermodynamic equilibrium (TE) computer code developed at Sandia Laboratories and BEACON/MOD2 is a nonequilibrium containment code developed at EG&G, Idaho. Initial results indicate that CSQ can reasonably model two-phase jets under TE conditions and that BEACON/MOD2 has certain problems that might preclude its use in this study.

Future work planned for the remainder of FY79 involves investigating the applicability of the LASL TRAC code⁴ to the two-phase jet problem, performing additional analysis with CSQ, and providing input to the future blowdown test series at the HDR Test Facility.

5.2 Experimental Data

The two-phase jet experimental data being analyzed at Sandia come from three sources in the FRG: KWU (RS93 and 93A), Battelle (RS-50), and HDR. A comparison of these facilities with a typical PWR (ZION) cold leg is given in Table 5-I.

TABLE 5-I

Experimental Test Facility Comparison

Facility	Pressure (bar)	Temperature (°C)	Diameter (cm)	Mass Flow (kg/s)	Mass Flux (kg/s/m ²)	Comments
ZION	157.23	276.7	50.85	4606	12019	PWR cold leg
KWU	30-100	234-311	1, 2.5, 5, 6.5	80	24108-	Tapered nozzle, adiabatic exit pipe
RS-50	140 max	300 max	10.	400 (double- ended break)	50929	Pressure vessel + steam surge tank 1/64 scale BIBLIS PWR.
HDR; Series 1	88 max	220 max	35	1222 max (steam)	12701	400% flow (all headers attached)
Series 3	110 max	310 max	35 or 45	1222 max (steam)	7683 or 12701	400% flow

5.2.1 KWU

Two-phase jet impingement studies were carried out at KWU - Erlangen under Research Projects BMFT RS93 and RS93A. The results of these tests can be found in the final reports, NRC 477⁵ and NRC 478.⁶

Blowdown tests were performed for initial conditions ranging from pressures of 30 to 100 bars, temperatures from 234° to 311°C, and nozzle diameters of 10 to 65 mm. System diagrams for circumferential and longitudinal breaks are shown in Figures 5-1 and 5-2. Figures 5-3 through 5-5 show typical results obtained for circumferential breaks. Note the bell-shaped pressure distribution found on the impingement plate.

Two geometries were used for the longitudinal break studies from pipes of 10 mm diameter. These are shown in Figure 5-6. Results for the longitudinal tests are shown in Figure 5-7 where a significant geometry effect is apparent.

5.2.2 Battelle RS-50

Research Project RS-50 is a 1/64 volumetric scale blowdown facility based on the 1200 MW BIBLIS PWR reactor.⁷ The test arrangement for RS-50 is shown in Figure 5-9. Possible break locations and reactor room compartmentalization are shown in Figure 5-8.

The use of both a pressure vessel model and a pressure surge tank in RS-50 should produce results more applicable to a PWR cold leg blowdown than facilities that only model the pressure vessel.

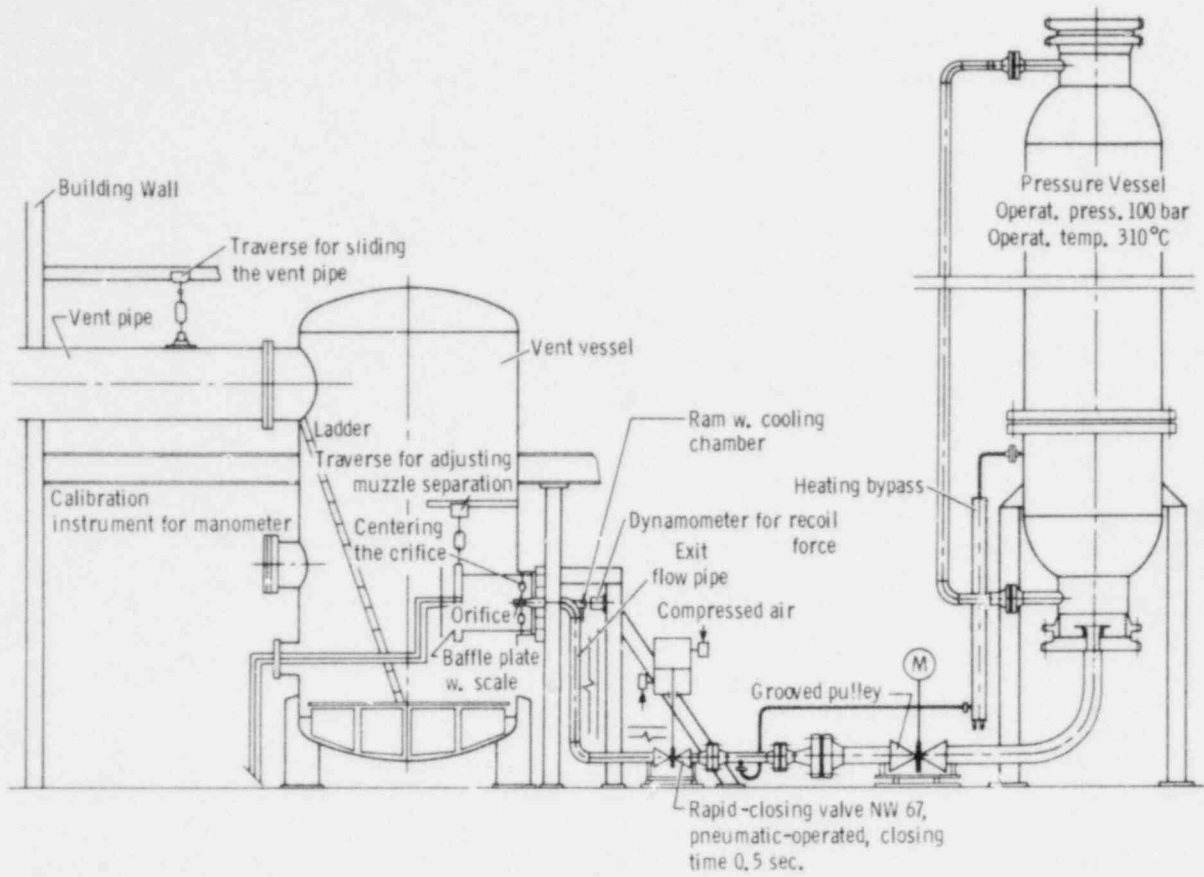


Figure 5-1. KWU Experimental Test Facility

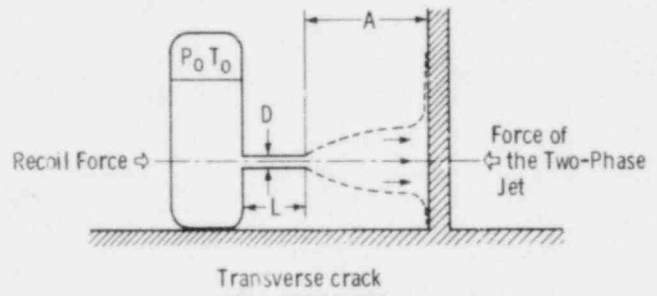
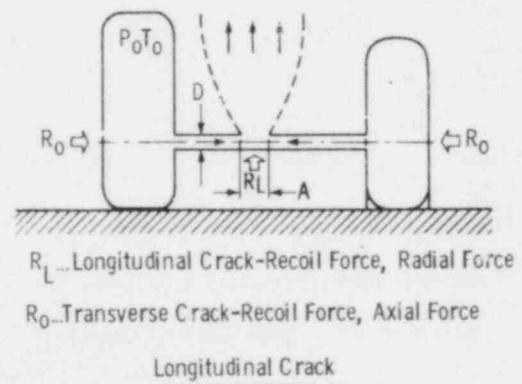


Figure 5-2. KWU Break Geometries



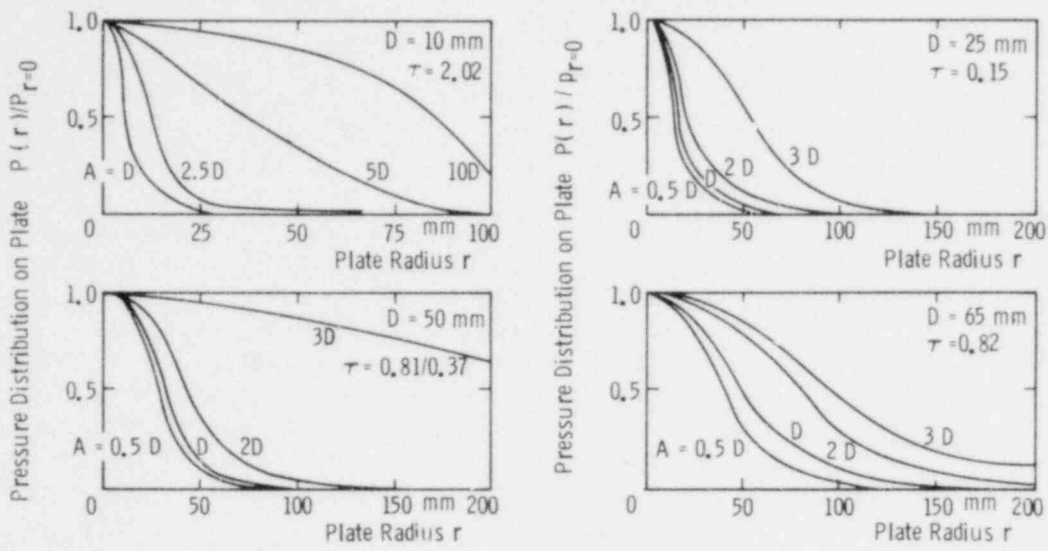


Figure 5-3. Pressure Distribution on the Baffle Plate for NW 10, NW 25, NW 50, NW 65 Orifices (KWU)

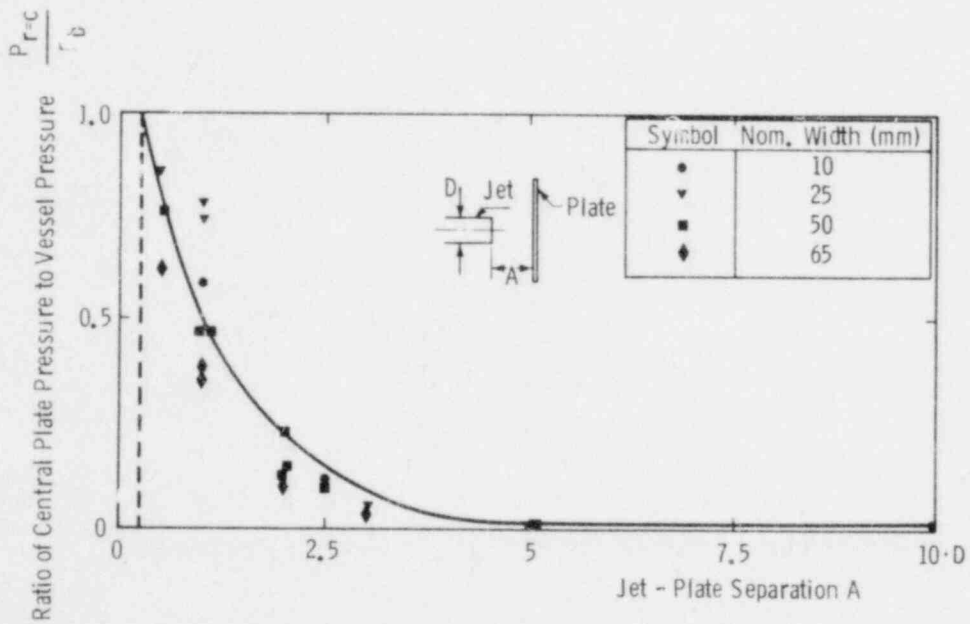


Figure 5-4. Range of the Two-Phase Jet (KWU)

- Jet expansion including zone of jet deflection on baffle plate for circular orifices ($A < .25D$)
- Jet expansion for elliptical orifices (surface area equal to $NW 50$)

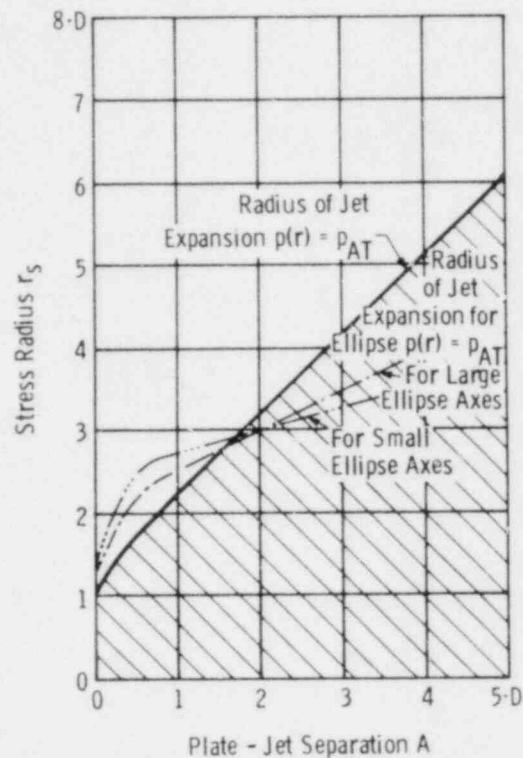


Figure 5-5. Determination of Load Surfaces on the Plate, Jet Expansion (KWU)

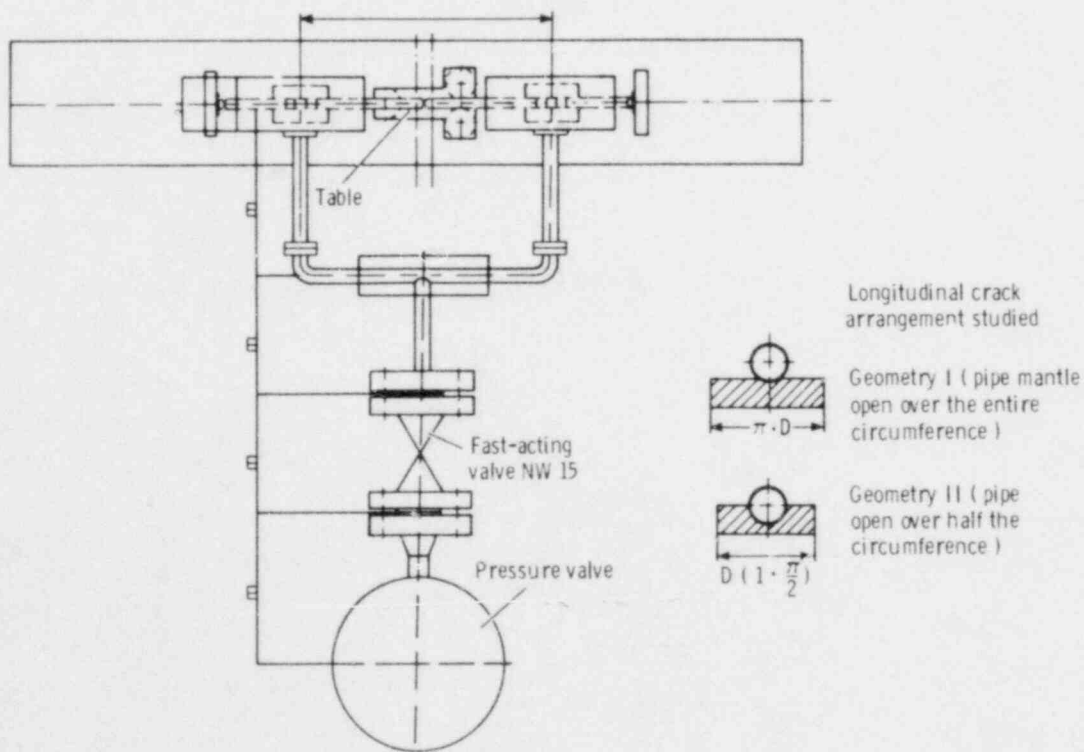


Figure 5-6. Set-Up for Longitudinal Crack Tests NW 10, $\zeta = 7.5$ (KWU)

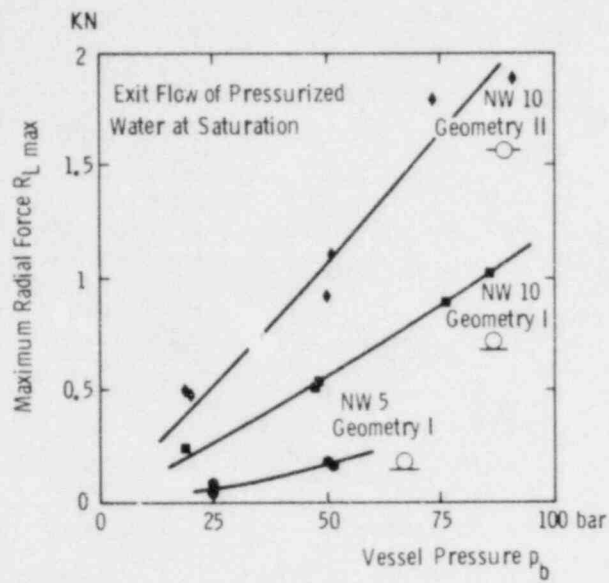


Figure 5-7. Maximum Radial Force for Longitudinal Crack Tests NW 5 and NW 10, Geometries I and II for $A/D = 0.61$

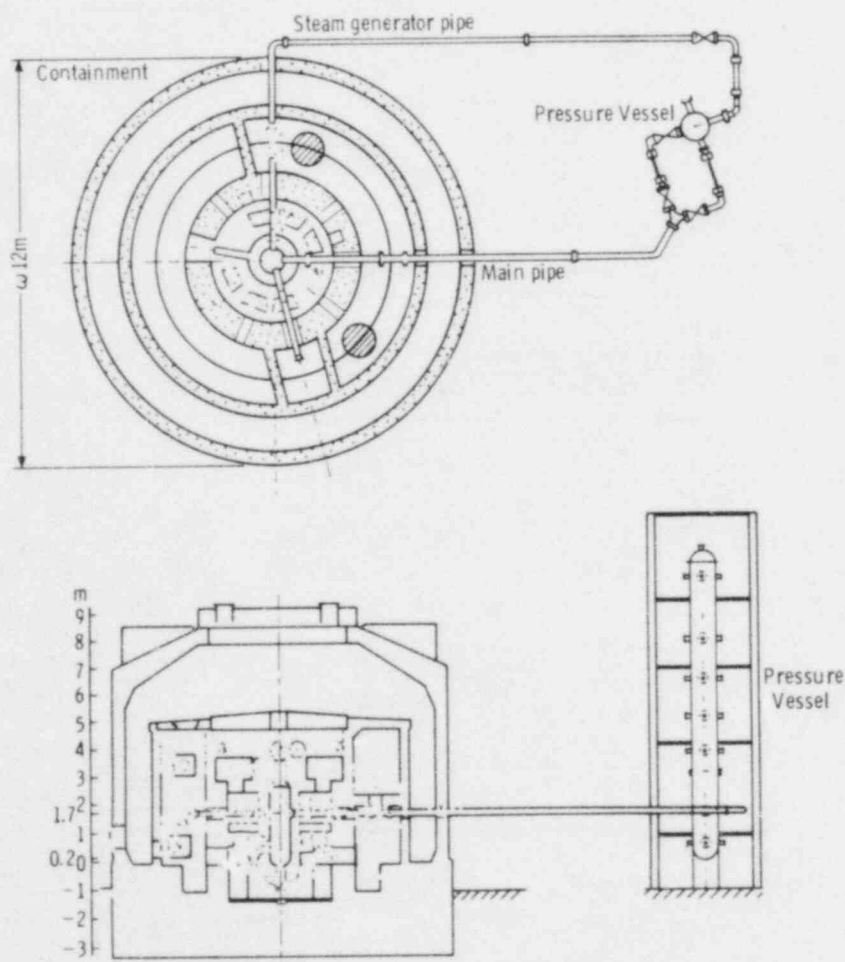


Figure 5-8. Model Containment (PWR configuration) R1-10, compartments; B1-9, sites of rupture; U13....., vent ducts (Battelle Institut)

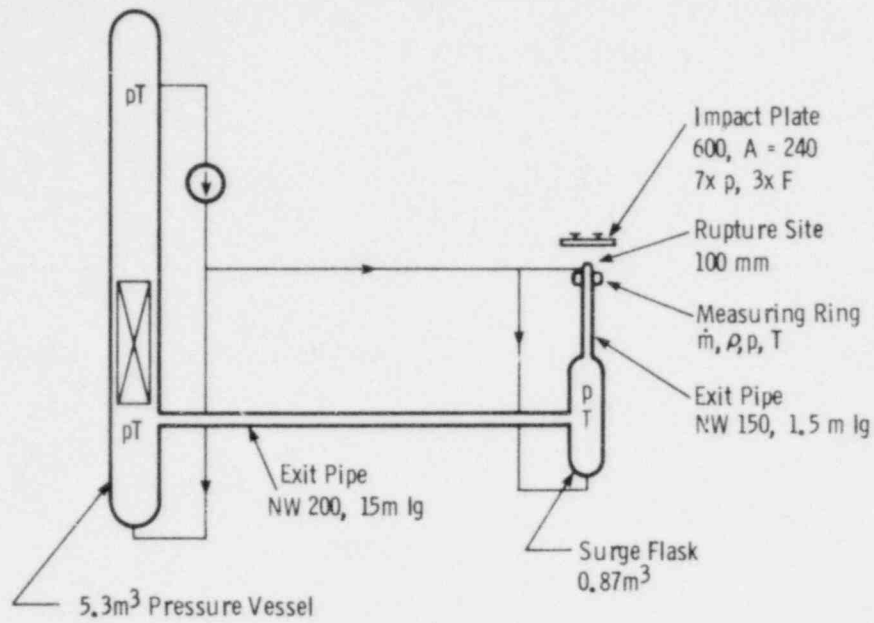


Figure 5-9. System RS-50, Test C11, C12 (Battelle)

Typical results for the nozzle configurations shown in Figures 5-10 and 5-11 are shown in Figures 5-12 through 5-15. The similarity in pressure profiles in the radial direction on the target between RS-50 and KWU data should be noted. No axial pressure distributions are available from RS-50 because all tests were performed using a separation of 240 mm.

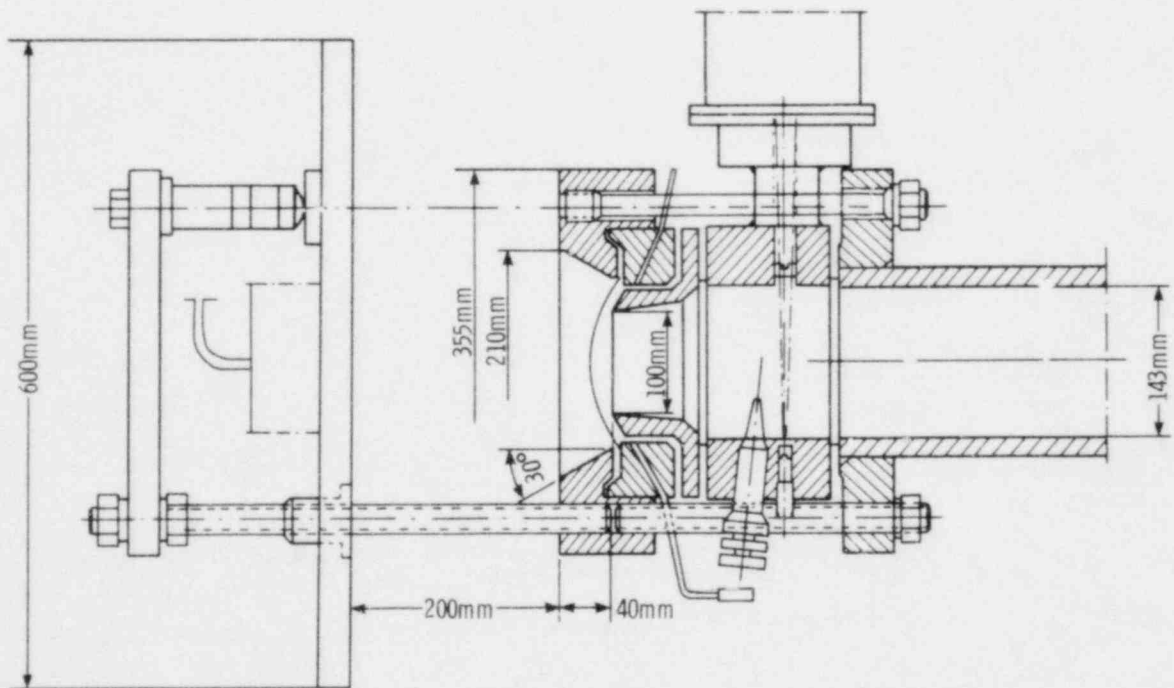


Figure 5-10. RS-50 Nozzle Configuration (Battelle)

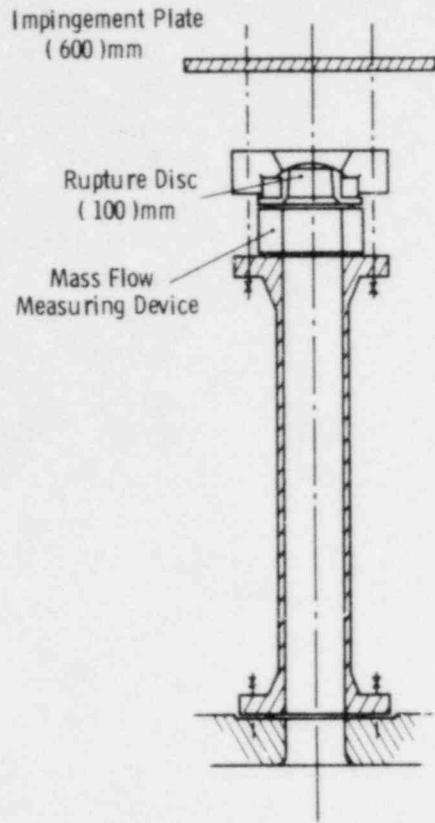


Figure 5-11. RS 50 Rupture Disc Assembly (Battelle)

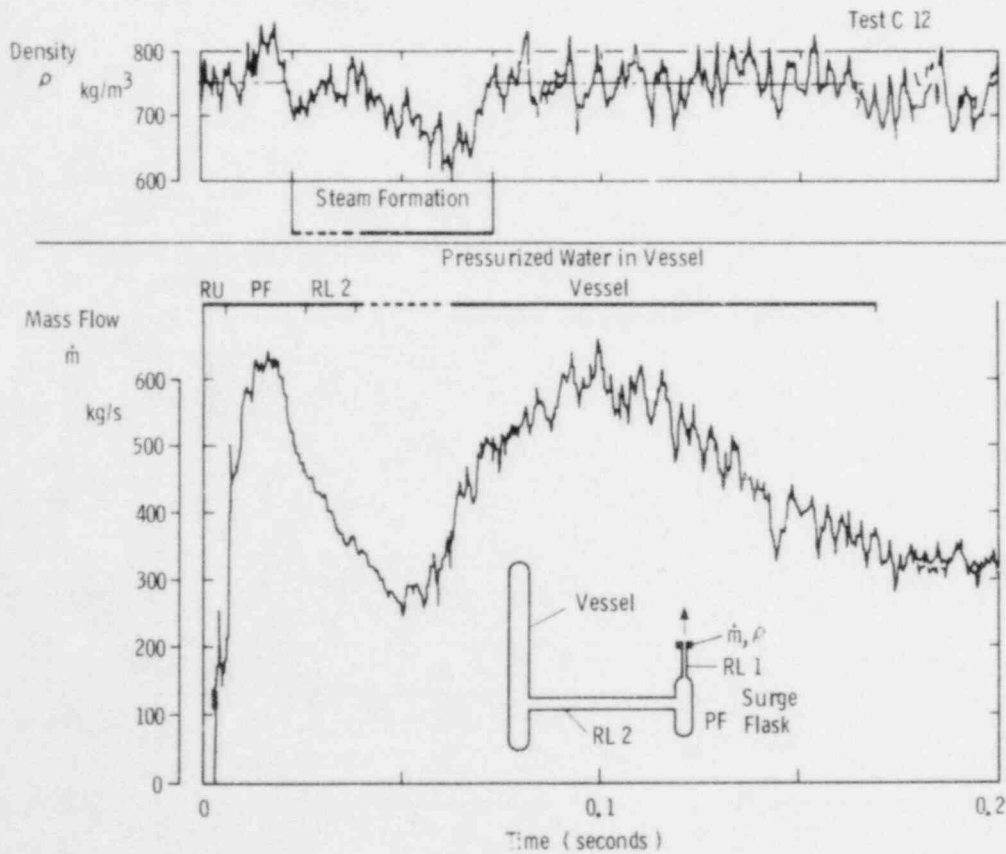


Figure 5-12. Mass Flow and Density (Battelle)

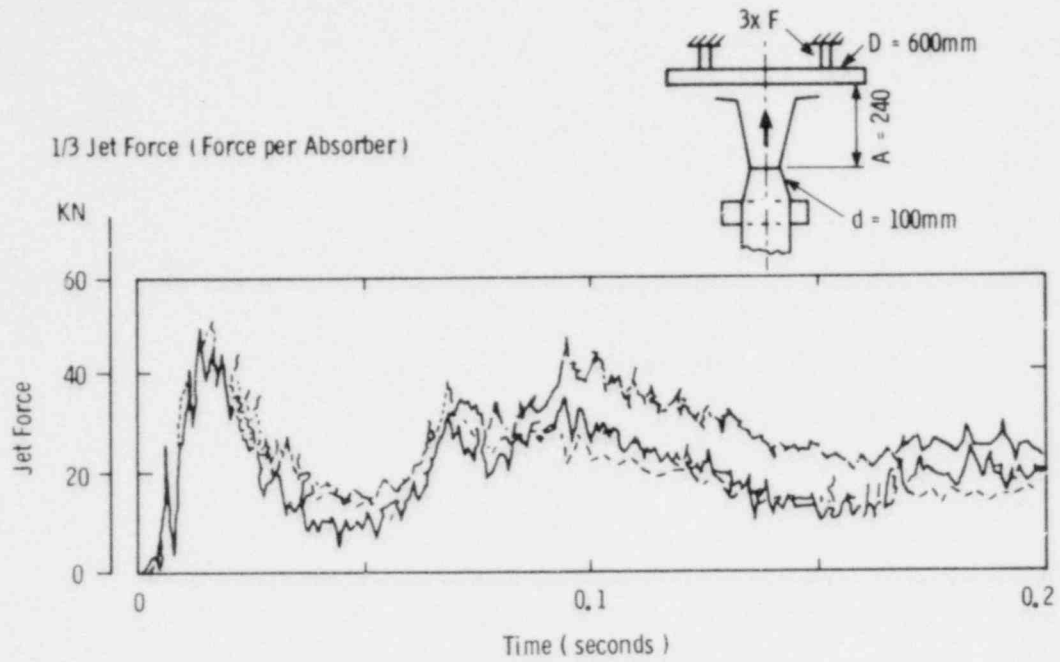


Figure 5-13. Integral Jet Force, RS-50 Test C12 (Battelle)

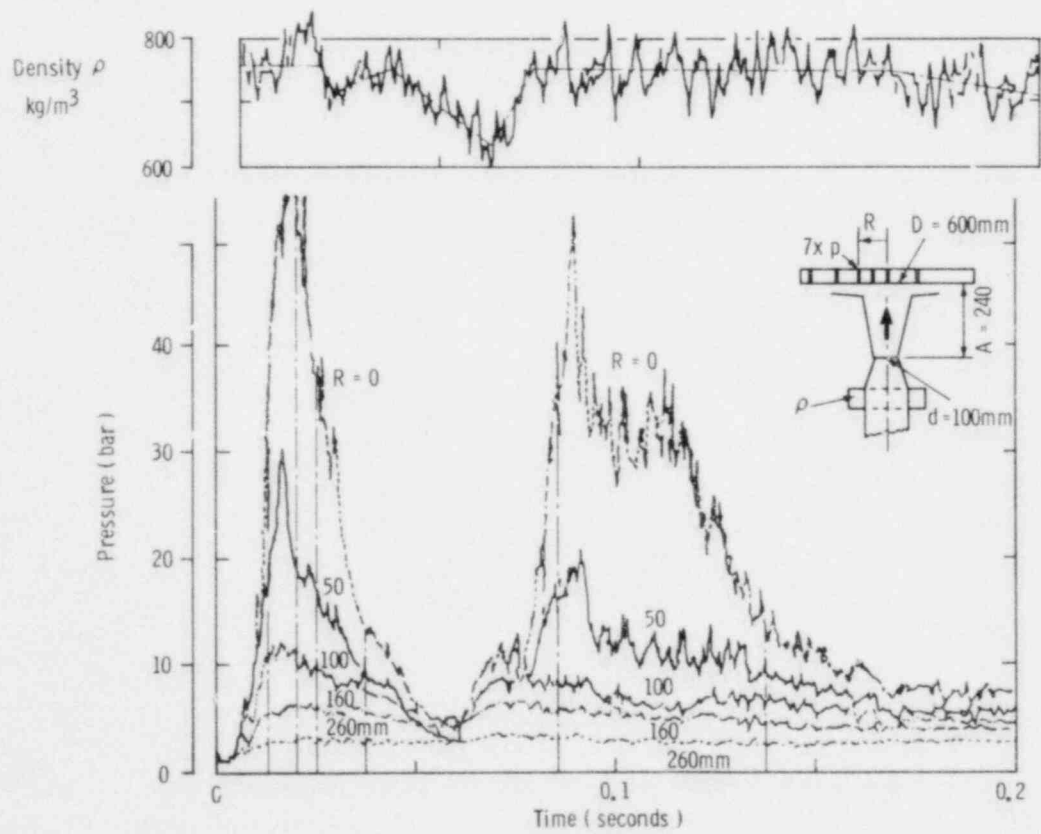


Figure 5-14. Correlation Between Jet Force and Density Upstream of the Outflow Section (Battelle)

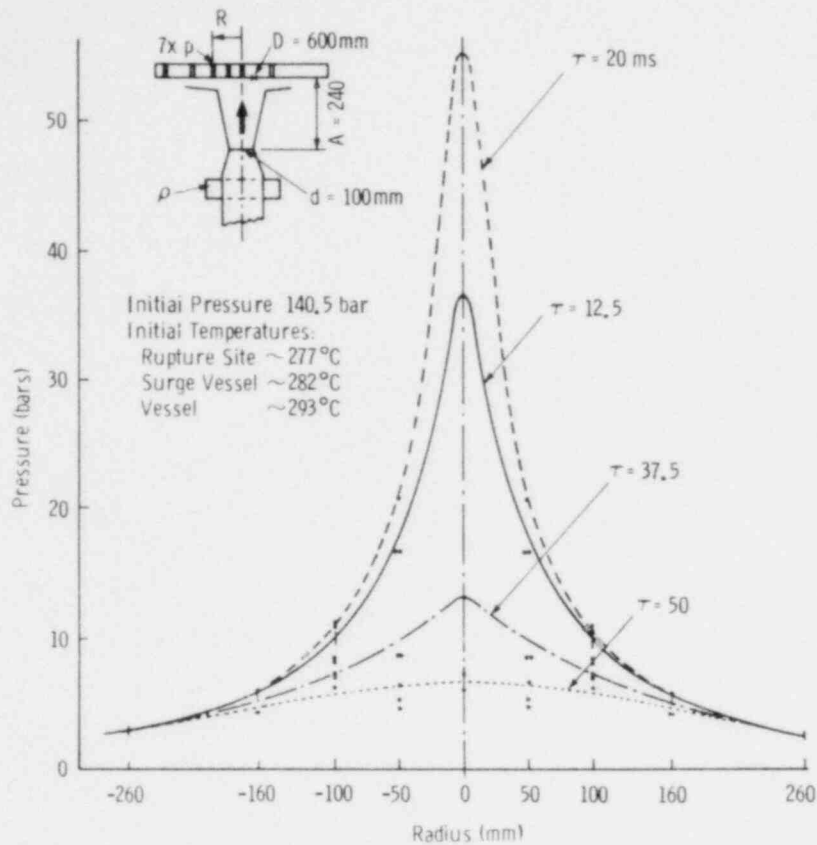


Figure 5-15. Jet Force Distribution, Test C12 (Battelle)

5.2.3 HDR

Blowdown tests are currently being planned at HDR, the superheated steam test facility.⁸ This facility is shown in Figure 5-16. The operating range for the HDR blowdown tests as well as approximate dates of availability are given in Table 5-II. Measurement locations for a typical blowdown test (V 22.1) are shown in Figure 5-17.

Data obtained from the series I and III blowdown tests should be very useful in the analysis of two-phase jet loading.

TABLE 5-II

Operating Range for HDR Blowdown Tests^{*}

Test	Availability Date	Nozzle Diameter (mm)	P_{max} (bar)	T_{max} ($^\circ\text{C}$)	T_{sat} ($^\circ\text{C}$)
I. Water Pipe	4/79	350	88	220	301.8
II. Steam Pipe	2/79	450	90	310	303.42
III. Water Pipe	4/81	350 or 450	110	310	318.7

^{*} Separation ratio (distance from nozzle to target/nozzle diameter) = 0.5 to 2

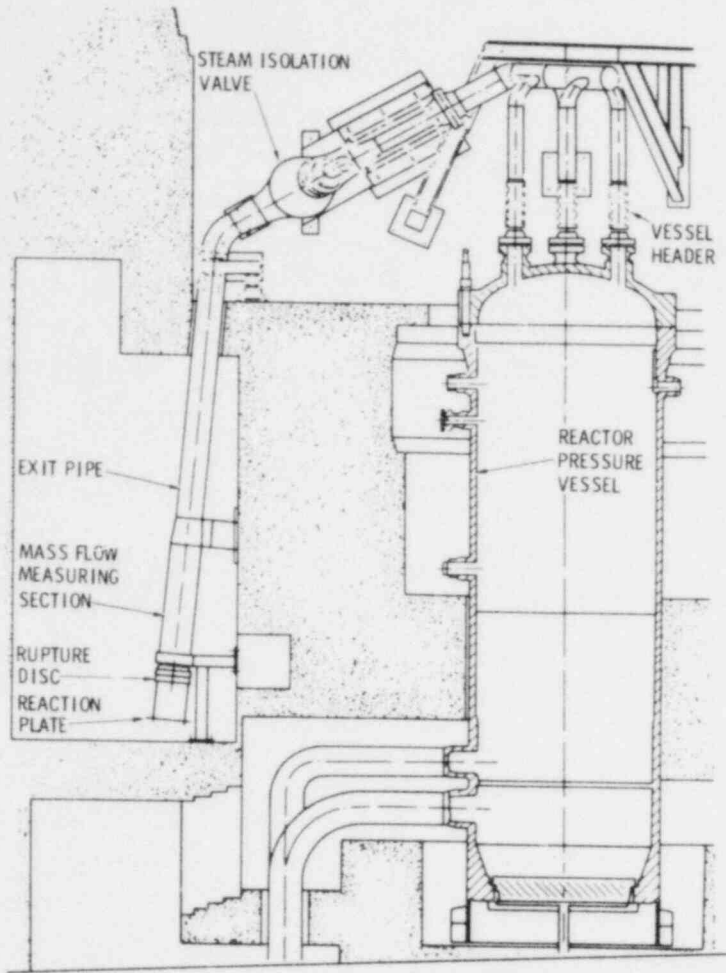
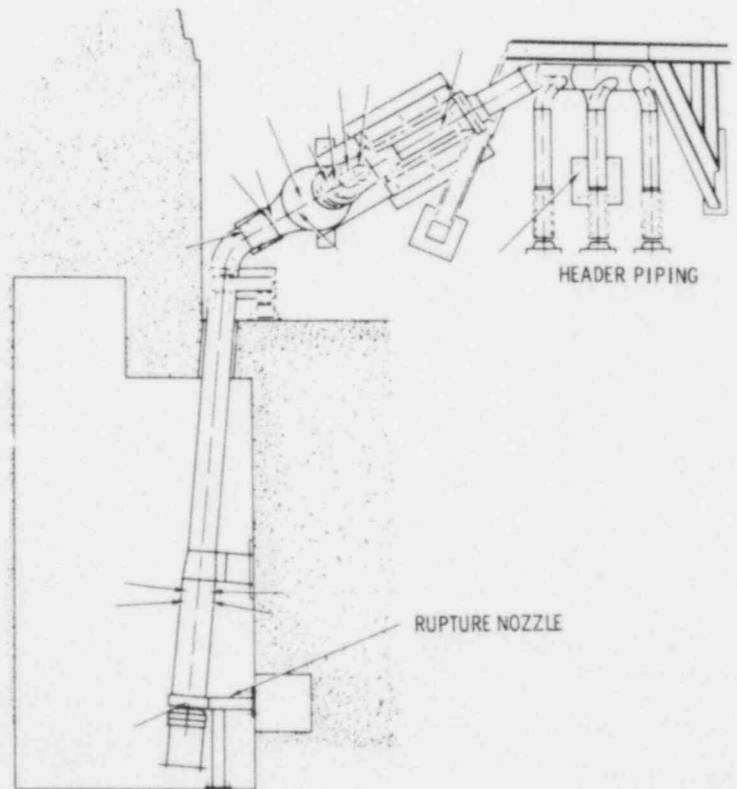


Figure 5-16. HDR Assembly

Figure 5-17. Measurement Locations for HDR Test V22.1



5.2.4 Summary of Experimental Data

The experimental data from the FRG presently available at Sandia are adequate for determining some of the properties of two-phase jets, such as radial and axial pressure profiles and impingement loads. However, in general the data are not sufficiently detailed to permit an in-depth analysis of the problem. Efforts are being made to acquire further information which will facilitate computer analysis. This includes physical dimensions of the systems, locations of the measurement instrumentation, fine-time resolution data (for at least the first 100 ms of the blowdown, during which time analysis indicates that the maximum impingement load has occurred), and information on the thermohydraulic conditions at the pipe exit.

5.3 Computer Program Results

Two computer programs are currently being tested to determine their applicability to two-phase jet analysis. These are CSQ and BEACON/MOD2. Testing with TRAC-P1 will begin shortly and continue through the remainder of FY79.

5.3.1 CSQ

CSQ is a two-dimensional, multimaterial thermodynamic equilibrium (TE) code developed at Sandia Laboratories.² It is being tested with data from KWU test 6 (NW50). A diagram of the CSQ model used for KWU test 6 is shown in Figure 5-18, and a list of initial conditions and blowdown data are given in Table 5-III for both the experiment and the CSQ calculation.

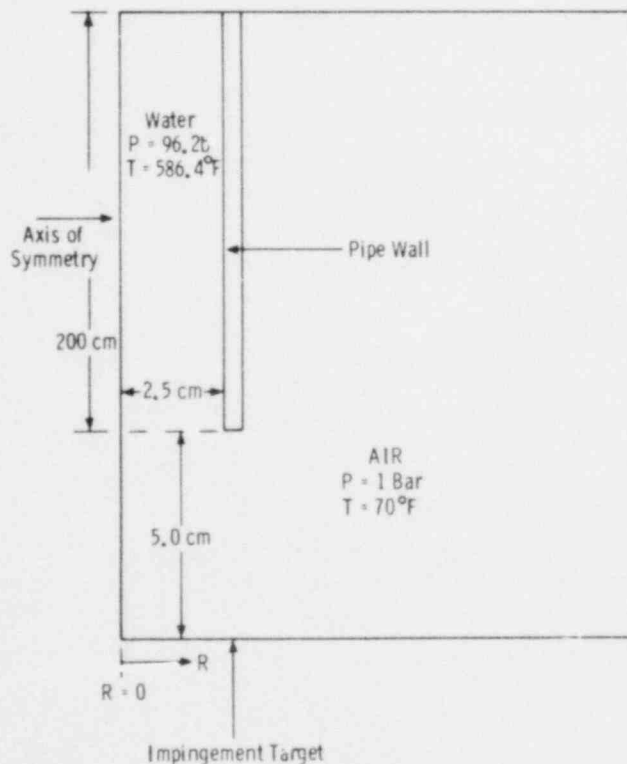


Figure 5-18. CSQ KWU Test 6 Model

TABLE 5-III

KWU Test 6 and CSQ Initial Conditions and Blowdown Results

Parameter	Experimental	CSQ Calculation
Initial pressure (bar)	96.2	96.2
Initial temperature ($^{\circ}\text{C}$)	308	308
Nozzle diameter (cm)	5	5
Distance to target (cm)	5	5
Break flow (kg/s)	36.4	48
Break pressure, 2 cm upstream of break (bar)	57.4	58
Maximum plate pressure, $R = 0$ (bar)	46	32
Coefficient of friction	0.81	0.0

An examination of Table 5-III indicates that CSQ correctly predicts the break pressure but that the mass flow is about 15% low. Also, the exit quality obtained by CSQ for this calculation is about 25% high. These differences may be the result of using a TE calculation under nonequilibrium conditions. (Rivard has shown that, for low upstream voiding, the calculated mass flows can be up to 25% lower than experimental data.⁹ Figure 5-19 shows that upstream of $L/D > 10$, our model has essentially no voiding and can be subject to a boiling delay. At the throat, a non-TE model would produce a larger break flow because of the lower exit quality.)

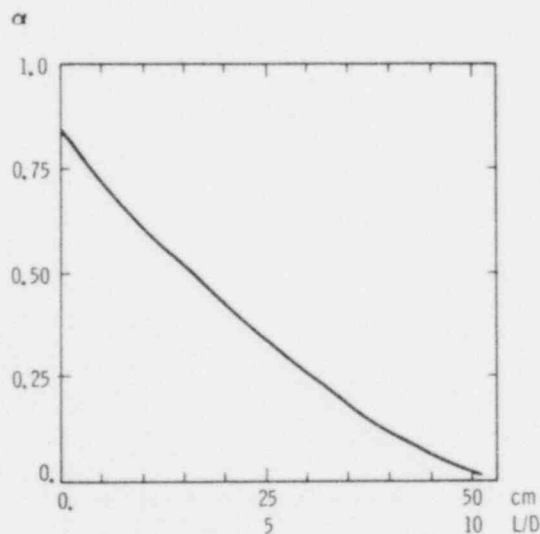


Figure 5-19. Void Fraction (α) vs Distance From Throat (upstream), CSQ KWU Test 6, $t = 5 \times 10^{-3}$ s

A comparison, CSQ vs experimental data, of the normalized pressure profile ($P_R/P_{R=0}$ vs R) on the impingement target at a separation distance equal to one diameter is shown in Figure 5-20. The experimental curve is more "peaked" towards the center of the target ($R = 0$) than the CSQ calculation which has a flatter profile. This may be because of more rapid boiling and more rapid expansion in the TE model.

A study was also performed to determine the effect of Eulerian mesh size on the maximum pressure on the target ($R = 0$). The results of this study are shown in Figure 5-21. Finer mesh sizes than 0.1 cm are possible, but run times and computer costs become very large for a finer mesh.

Figure 5-20. Radial Pressure Profile

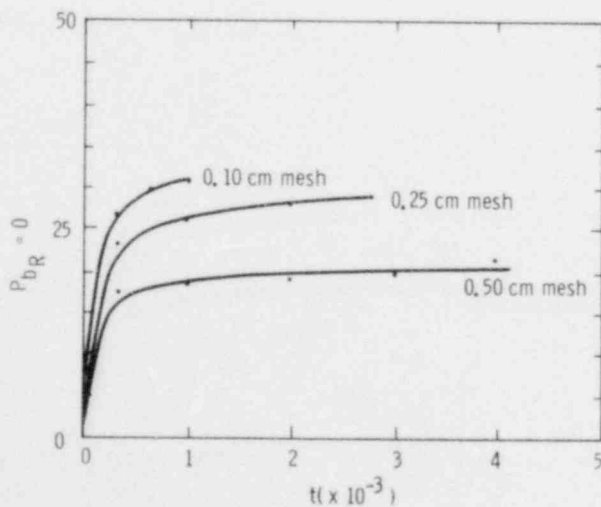
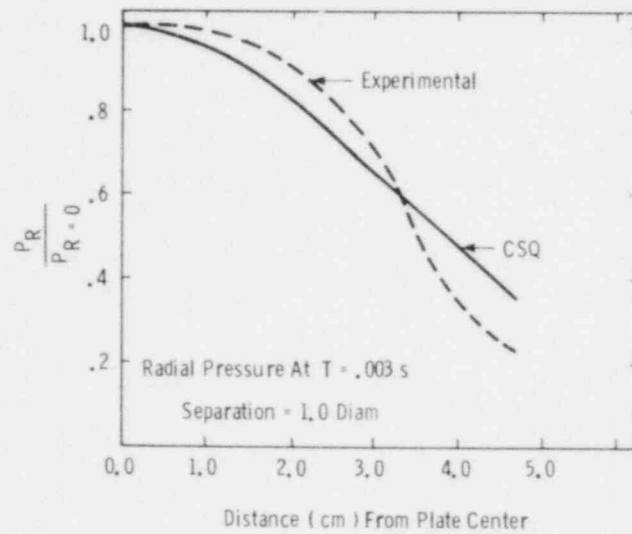


Figure 5-21. Plate Pressure vs Mesh Size

In Figure 5-22, a comparison is made of the maximum plate pressure as a function of axial separation from the throat (normalized to stagnation pressure = 96.2 bars) for CSQ calculations vs experimental data. The CSQ pressures fall off faster than the experimental data. This may again be the result of nonequilibrium effects in the nozzle.

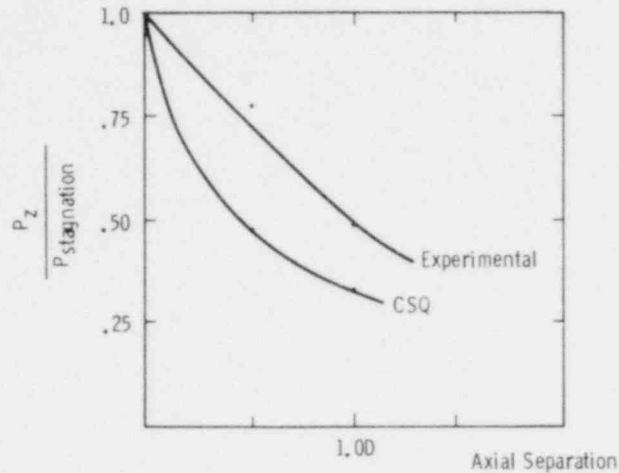


Figure 5-22. Impact Plate Pressure vs Axial Separation

Future work with CSQ will concern modifying the model to determine if the nonequilibrium effects can be reduced and a better fit with the experimental data obtained. The modeling effort will also be expanded to include data from research project RS-50 and the HDR test facility.

5.3.2 BEACON/MOD2

BEACON/MOD2 is a two-phase, two-component, nonequilibrium code developed at EG&G, Idaho.

Figure 5-23 shows the model used in simulating KWU test 6.

The one-dimensional pipe axial pressure profile obtained with the use of BEACON/MOD2 is shown in Figure 5-24. The break pressure is somewhat low (45 bar) while the critical mass flow is significantly high (25%). This is probably the result of a combination of three factors: the incompressible liquid model used, the coarseness of the mesh (1 cm), and the sensitivity of the calculation to the phase change model multipliers.

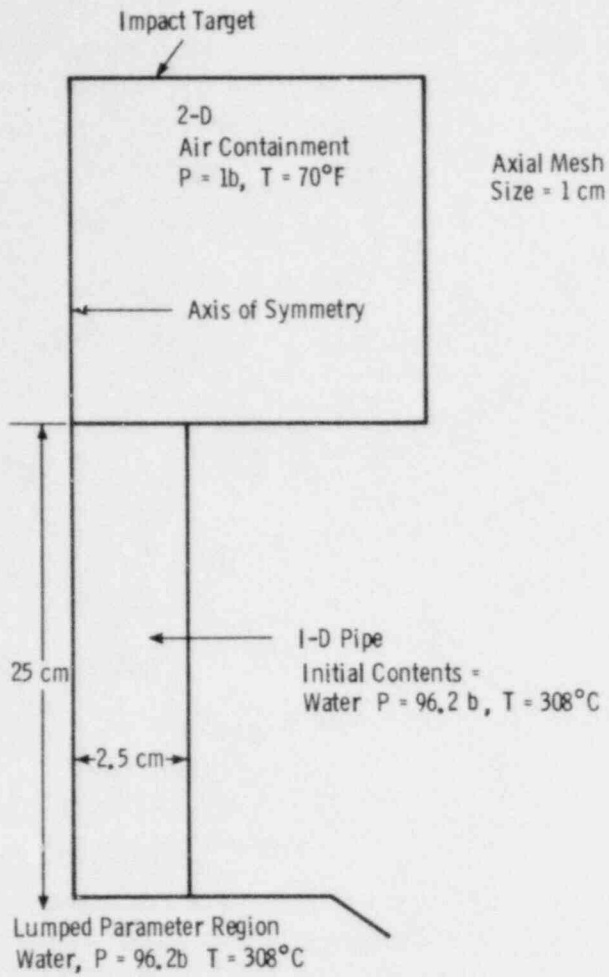


Figure 5-23. BEACON/MOD2 KWU Test 6 Model

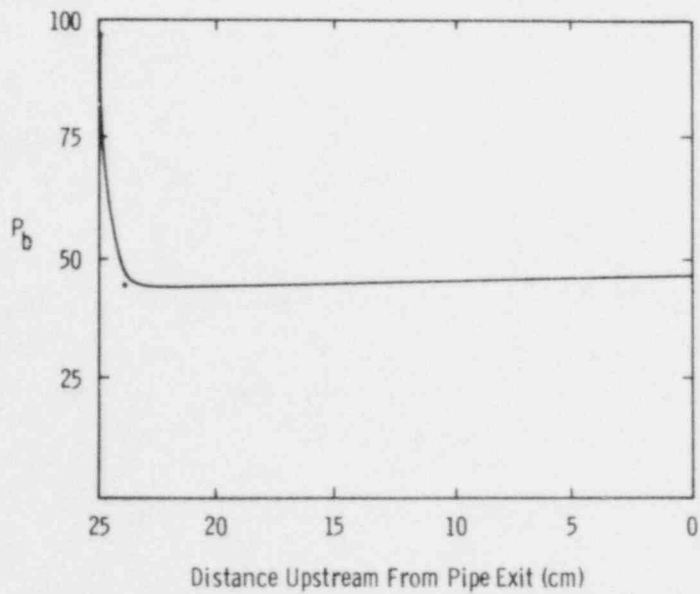


Figure 5-24. Axial Pressure in BEACON/MOD2 One-Dimensional Pipe, $t = 0.01$ s

While attempting to use BEACON/MOD2, the following problems were encountered:

- The BNL equation-of-state package--compressible liquid and real steam-- failed (frequent overflows caused by division by zero).
- The LASL equation-of-state option employs a constant liquid density (212°F) and an ideal gas approximation for steam. This results in errors of the order of 5% in break flows.
- The calculations are very sensitive to the evaporation rate multiplier used in the Rivard phase change model.¹⁰ (This model has recently been replaced in LASL codes with a phase change model that better predicts the experimental data.)
- The nonequilibrium features of the code have not been verified. The code is typically run with a large heat transfer coefficient to force phase equilibrium.
- All mass transfer models, other than Rivard's (homogeneous flow), are untested.
- The code must be run with a fixed mesh size in ΔZ (to use a fine zone mesh at the pipe exit requires using the same fine zoning throughout the model because of the donor-cell technique employed). This leads to excessively long run times and high computer costs.
- The automatic time step control feature of the code is inoperative for this type of problem. (The internally set time step is too large causing the code to fail.)
- The graphics package (IGS) is incompatible with the Sandia computer system.
- No graphics output tape is generated during program execution.

Due to the above difficulties with BEACON/MOD2, it is evident that more work needs to be done before it can be used confidently in a blowdown mode. Future work with BEACON will address its use in a containment mode. Detailed information will be required about break flows and pressures.

5.4 Future Work

Future work on the two-phase jet load program will include calculations with the LASL TRAC code, improving the model for CSQ analysis, modeling other facility blowdowns (RS-50, HDR), assessing BEACON in a containment mode, and beginning the nodalization and parametric studies.

References for Section 5

1. F. J. Moody, "Fluid Reaction and Impingement Loads," Specialty Conference on Structural Design of Nuclear Plant Facilities, December 1973.
2. S. L. Thompson, CSQ-A Two-Dimensional Hydrodynamic Program With Energy Flow and Material Strength, SAND74-0122, Sandia Laboratories, Albuquerque, NM, August 1975.
3. C. R. Broadus, S. W. James, W. H. Lee, J. F. Lime, and R. A. Pate, BEACON/MOD2 a CDC 7600 Computer Program for Analyzing the Flow of Mixed Air, Steam, and Water in a Containment System, CDAP-TR-002, EG&G, Idaho, December 1977.
4. TRAC-P1: An Advanced Best Estimate Computer Program for PWR LOCA Analysis, NUREG/CR-0063, LA-7279MS, Vol. 1.
5. R. Eichler, W. Kastner, H. Lochner, and K. Riedle, Studies on Critical Two-Phase Flow, NRC-477.
6. W. Kastner, R. Eichler, and K. Riedle, Experimental Studies on Forces of Critical Two-Phase Jets for Transverse and Longitudinal Cracks in Pipelines, NRC-478.
7. LOCA Experiments with a PWR Multi-Compartment Model Containment, BF-RS50-62-5, Battelle Institut E. V. Frankfurt Am Main.
8. KfK Nachrichten, Vol. 9, No. 2, 1977, NUREG/TR-0038.
9. W. C. Rivard, Nonequilibrium Phenomena and Structural Interactions in LWR Blowdown Studies, LA-UR-78-2565.
10. W. C. Rivard and M. D. Torrey, Numerical Calculation of Flashing From Long Pipes Using a Two-Field Model, LA-6104 MS.

DISTRIBUTION:

US Nuclear Regulatory Commission
(340 copies for R3)
Division of Document Control
Distribution Services Branch
7920 Norfolk Ave
Bethesda, MD 20014

US Nuclear Regulatory Commission (6)
Office of Nuclear Regulatory Research
Washington, DC 20555
Attn: W. C. Lyon
N. Zuber
S. Fabic
C. E. Johnson
R. R. Sherry
M. Vagins

US Nuclear Regulatory Commission (3)
Division of Systems Safety
Office of Nuclear Reactor Regulation
Washington, DC 20555
Attn: B. Sheron
N. Lauben
E. Throm

US Department of Energy
Operational Safety Division
Albuquerque Operations Office
P. O. Box 5400
Albuquerque, NM 87185
Attn: J. R. Roeder, Director

Westinghouse Electric Corporation
Research and Development Center
Churchill Boro
Pittsburgh, PA 15235
Attn: M. Mazumdar
Mathematics Department

Florida International University
Department of Statistics
Tamiami Trail
Miami, FL 33144
Attn: S. S. Shapiro

EG&G - Idaho, Inc. (2)
P. O. Box 1625
Idaho Falls, ID 83401
Attn: N. D. Cox
D. M. Snider

Electric Power Research Institute
3112 Hillview Avenue
Palo Alto, CA 94304
Attn: J. Carey

Offshore Power System
8000 Arlington Expressway
Box 8000
Jacksonville, FL 32211
Attn: D. H. Walker

Prof. S. Abdul-Kalik
Nuclear Engineering Dept
University of Wisconsin
Madison, WI 53706

Dr. S. G. Bankoff
Chemical Engineering Dept
Northwestern University
Evanston, IL 60201

Westinghouse Advanced Reactor Division
P. O. Box 158
Madison, PA 15663
Attn: L. E. Strawbridge

Westinghouse Electric Corp. (2)
Bettis Atomic Power Laboratory
P. O. Box 79
West Mifflin, PA 15122
Attn: W. D. Peterson
F. W. Lincoln

Westinghouse Electric Corp. (2)
Nuclear Energy Systems
P. O. Box 355
Pittsburgh, PA 15230
Attn: R. P. Vijuk
M. Y. Young

Los Alamos Scientific Laboratory (2)
P. O. Box 1663
Los Alamos, NM 87545
Attn: M. McKay
J. Jackson

400 C. Winter
1200 L. D. Smith
1223 R. B. Easterling
1223 I. J. Hall
1537 N. R. Keltner
2514 D. E. Mitchell
4400 A. W. Snyder
4410 D. J. McCloskey
4412 J. W. Hickman
4420 J. V. Walker
4422 R. L. Coats
4422 D. W. Varela
4423 J. E. Powell
4425 W. J. Camp
4440 G. R. Otey
4441 M. Berman (10)
4441 L. D. Buxton
4441 R. K. Byers
4441 R. K. Cole, Jr.
4441 B. W. Burnham
4441 D. Tomasko
4441 J. F. Muir
4442 W. A. Von Riesemann

DISTRIBUTION (Cont):

4443 D. A. Dahlgren
4450 J. A. Reuscher
4533 B. D. Zak
4550 R. M. Jefferson
32 H. J. Sutherland
3131 W. B. Benedick
5511 D. F. McVey
5511 B. M. Bulmer
5511 M. L. Corradini
5512 D. W. Larson
5520 T. B. Lane
5530 W. Herrmann
5532 B. M. Butcher
5534 J. E. Smaardyk
5641 G. P. Steck
5830 M. J. Davis
5830 L. S. Nelson
5831 N. J. Magnani
5831 D. A. Powers
5833 F. J. Zanner
5846 E. K. Beauchamp
5846 R. A. Sallach
8266 E. A. Aas
3141 T. L. Werner (5)
3151 W. L. Garner (3)
For: DOE/TIC (Unlimited Release)
3154-3 R. P. Campbell (25)
For Distribution to NTIS